Syracuse University

SURFACE at Syracuse University

Dissertations - ALL

SURFACE at Syracuse University

10-31-2022

Design and modeling of superconducting hardware for implementing quantum stabilizers

Yebin Liu

Follow this and additional works at: https://surface.syr.edu/etd

Part of the Physics Commons

Recommended Citation

Liu, Yebin, "Design and modeling of superconducting hardware for implementing quantum stabilizers" (2022). *Dissertations - ALL*. 1607.
https://surface.syr.edu/etd/1607

This Dissertation is brought to you for free and open access by the SURFACE at Syracuse University at SURFACE at Syracuse University. It has been accepted for inclusion in Dissertations - ALL by an authorized administrator of SURFACE at Syracuse University. For more information, please contact surface@syr.edu.

ABSTRACT

Superconducting qubits are one of the leading systems for implementing quantum processors. Realizing fault-tolerant quantum computation requires some form of quantum error correction, which typically involves performing repeated stabilizer operations on groups of physical qubits in an array to form a logical qubit with enhanced protection against errors. Realizing a logical qubit that is suitable for running quantum algorithms requires an array with a significant number of physical qubits, which is extremely challenging. However, the physical qubit overhead can be reduced by lowering the error rate on the physical qubits. Current state-of-the-art superconducting qubit designs do not have robust protection against all types of errors. Reducing error rates on these conventional qubits requires further advances in fabrication, materials, and device packaging to reduce the noise and perturbations coupled to the qubit.

Another approach to reduce the error rates is to develop new qubit designs that have intrinsic protection against all types of errors. The charge-parity qubit is one such design. Conventional superconducting qubits are based on Josephson junctions, which have a 2π-periodic dependence on the superconducting phase difference across the junction. The charge-parity qubit is formed from a chain of plaquettes, each of which behaves as a π-periodic Josephson element. For appropriate parameters, the effective coupling Hamiltonian between plaquettes in a charge-parity qubit is equivalent to the implementation of a quantum stabilizer in superconducting hardware. In this thesis, I present the experimental realization of plaquette-chain devices that exhibit such stabilizer behavior. The plaquette devices are fabricated with arrays of Josephson junctions, with multiple on-chip flux- and charge-bias lines for local biasing of the various device elements. Microwave spectroscopy measurements allow for a characterization of the transitions between the different energy levels of the plaquette chain and their dispersion with flux and charge bias of the various device elements. Extensive numerical modeling of the energy-level structure and comparison with the measured transition spectra indicates that the device exhibits protection against local noise. This work paves the way for future qubits based on this design with optimized parameters and implementations that are capable of achieving dramatic reductions in error rates beyond the current state of the art.

DESIGN AND MODELING OF SUPERCONDUCTING HARDWARE FOR IMPLEMENTING QUANTUM STABILIZERS

By

Yebin Liu

BS, China University of Mining and Technology, 2014

Dissertation
Submitted in Partial Fulfillment of the Requirements
for the degree of
Doctor of Philosophy in Physics

Syracuse University
December 2022

Copyright © 2022 Yebin Liu
All rights reserved.

ACKNOWLEDGMENTS

First, I want to thank my advisor, Prof. Britton Plourde, who guided me to be a scientist. Britton set a good example of doing research tirelessly with tremendous enthusiasm. He always understands complex problems quickly and explains them in a clear comprehensive way. Whenever I reached a bottleneck, Britton was there to brainstorm with me, support me, and help me pass through it. For example, when we were confused by the spectroscopy data, Britton encourged me to learn the SuperQuantPackage to model the circuit and gave a lot of great suggestions. Without his numerous examinations and revisions, this thesis cannot be finished.

I also want to thank Prof. Robert McDermott who often points out some key problems and offers effective solutions during the weekly discussions. I thank Prof. Lev Ioffe for coming up with the great charge-parity qubit idea and offering theoretical insight to explain our experimental data. I also thank Prof. Ivan Pechenezhskiy for the discussion of the fluxonium qubit and sharing his experience of working in industry and academia. I thank Prof. Jae Oh, Prof. Simon Catterall, Prof. Denver Whittington and Prof. Liviu Movileanu to be my thesis defense committee members.

I want to thank Dr. Matthew Hutchings for training me in fabrication and qubit measurement. I thank Dr. JJ Nelson for sharing his in-depth fabrication knowledge. I thank Dr. Jaseung Ku for solving all kinds of problems in a responsible and comprehensive way, which I benefit a lot.

I want to especially thank Dr. Andrey Klots. Andrey instructs me to model our circuit correctly using SuperQuantPackage, which is a great tool he developes. Thanks for the continuous discussion of understanding the circuit, improving the modeling, and exchanging ideas of the evolving world.

I want to thank Dr. Kenneth Dodge for working with me on the same project. We supported each other and Kenneth's jokes are good stress reliever. I also want to thank Bradley Cole for fabricating our devices so quickly with high yields. I want to thank Michael Senatore, Andrew Ballard, Vito Iaia, Tianna McBroom, Eric Yelton, Clayton Larson, Jadrien Paustian for the cheerful lab atmosphere. I enjoy chatting and playing sports with you.

I want to thank Dr. Yu(Hugo) Hao for emphasizing the attenuation to details when doing research. He spent hours with me again and again during my hardest time for finding a job and gave meaningful suggestions. I want to thank Dr. Daniela Bogorin, Dr. Matthew Ware, Dr. Caleb Jordan, Dr. Indrajeet, Dr. Haozhi Wang, who are former members in the Plourde lab, for offering a lot of helps during my job searching period.

I want to thank Charlie Brown, Lou Buda and Phil Arnold for making the smaple boxes and other components. Especially Phil who drew a beautiful torus on my Plaque Award. I also want to thank Chris Alpha, Alan Bleier, Amrita Banerjee, Garry Bordonaro, Jeremy Clark, Vince Genova, Phil Infante, Tom Pennell, John Treichler, Aaron Windsor, Sam Wright for offering great helps for fabrication in CNF.

I want to thank my girlfriend Keyuan Li for not giving up our long-distance relationship starting right before COVID-19 outbreak three years ago. You fill my days with pleasure and laughter. I thank my friends for discussing all sort of matters in life and having fun together. This period of my life will be less joyful without you.

I thank my mother Xiaoying Zeng for giving me unconditional love. Being the kindest person I ever met, you educated me to be considerate. I thank my father Jinyang Liu for being supportive as always. Being a strong-mined person, you taught me to spare no effort when I encounter difficulties on the way of pursuing my dream. I thank my brother Yehui Liu for taking care of the family issues when I was away from home.

Contents

List of Tables ix

List of Figures xx

xxi

1 Introduction 1

2 Superconducting quantum computation 5
- 2.1 Qubit basics 5
- 2.2 Decoherence 7
- 2.3 Superconducting qubits 8
  - 2.3.1 Circuit QED 8
  - 2.3.2 Josephson junctions 9
  - 2.3.3 Transmon 11
  - 2.3.4 Fluxonium 13
- 2.4 Protected superconducting qubit 14
  - 2.4.1 Charge-parity qubit 15
- 2.5 Decoherence in superconducting qubits 15
  - 2.5.1 Dielectric loss 16
  - 2.5.2 Charge and flux noise 16
  - 2.5.3 Quasiparticles 17

3 Theory of superconducting hardware for implementing quantum stabilizers 18
- 3.1 π-periodic Josephson elements from dc SQUIDs 19

3.2 Single plaquette qubit 21
3.3 Double plaquette qubit 24
3.4 Concatenation and XX stabilizer 31
3.5 Triple plaquette qubit 32

4 Numerical modeling of Charge-Parity Qubits **33**
4.1 Introduction to SuperQuantPackage 33
4.2 Single frustration modeling 37
  4.2.1 Single frustration flux dispersion modeling 37
  4.2.2 Single frustration charge dispersion modeling 38
4.3 Double frustration modeling 40
  4.3.1 Double frustration flux dispersion modeling 41
  4.3.2 Double frustration flux dispersion vs. intermediate island capacitance 43
  4.3.3 Double frustration charge dispersion at double frustration . . 45
  4.3.4 Double frustration flux dispersion at different Q_{isl} 47
4.4 Triple frustration modeling 49
  4.4.1 Structureless plaquette model 49
  4.4.2 Triple frustration flux dispersion vs. intermediate island capacitance 49

5 Device design and fabrication **51**
5.1 Device parameters 51
5.2 Device design 53
5.3 Simulation 57
  5.3.1 Capacitance simulation 57
  5.3.2 Inductance simulation 59
5.4 Fabrication 59
5.5 Characterization of π-periodic Josephson element 62

6 Measurement of 3-plaquette chip **65**
6.1 Fridge setup 65
6.2 Electronics setup 67
6.3 Cavity flux tuning 68

6.4 Spectroscopy measurement . . . 72
6.4.1 Initialization . . . 72
6.4.2 Single frustration . . . 72
6.4.3 Double frustration . . . 75
6.5 Triple frustration . . . 81

7 Fitting of spectroscopy measurements **83**
7.1 General fitting strategy . . . 83
7.2 Single frustration fitting . . . 86
7.3 Double frustration fitting . . . 88
7.4 Triple frustration modeling . . . 92
7.5 Fitted parameter error estimation . . . 94

8 Summary and Future Directions **98**
8.1 Summary . . . 98
8.2 Improved parameters . . . 99
8.3 Parallel plate capacitor . . . 100
8.4 Reducing electronic capacitance . . . 100
8.5 Protected gates . . . 101

Bibliography **112**

List of Tables

5.1 Capacitances between the various charge bias lines (CB) and different islands. 58
5.2 Simulated island capacitance to ground 59
5.3 Simulated mutual inductances between flux-bias lines and plaquette loops. 59
6.1 Simulated and extracted inductance matrix. 71
6.2 Simulated and experimentally extracted capacitances between the charge bias lines (CB) and different islands. 79
7.1 Single frustration fitted parameters and estimated parameters from design and fabrication tests. 88
7.2 Double frustration fitted parameters and estimated parameters 92
7.3 Fitted parameter error estimation based on plasmon transition. . . . 95
7.4 Fitted parameter error estimation based on heavy fluxon transition. . 96
7.5 Fitted parameter error estimation based on light fluxon transition. . . 96
7.6 Fitted parameter error estimation based on plasmon-fluxon anticrossing. 96
7.7 Intersection of fitted errors estimated from four types of transition. . 97

List of Figures

2.1 Bloch sphere for representing an arbitrary qubit state in terms of the angles θ and ϕ. 6

2.2 (a) harmonic oscillator circuit. (d) parabolic potential. 9

2.3 (a) harmonic oscillator circuit schematic. (b) replacing the linear inductor with Josephson junction. (c) The potential of the circuit in (b). 11

2.4 (a) Fluxonium circuit diagram. (b) Fluxonium potential. 14

3.1 (a) Circuit schematic for dc SQUID plaquette. 2D potential as a function of common-mode (δ_p) and differential (δ_m) phase variables at external flux bias Φ_{ext} of (b) 0, (c) $\Phi_0/2$. (d) Linecut along δ_m for $\delta_p = 0$ for $\Phi_{ext} = 0$. (e) Linecut between adjacent minima vs. δ_m for $\Phi_{ext} = \Phi_0/2$. (f) Linecut along δ_p at $\delta_m = 0$ for $\Phi_{ext} = 0$. (g) Linecut between adjacent minima vs. δ_p for $\Phi_{ext} = \Phi_0/2$. 20

3.2 (a) Circuit schematic for dc SQUID plaquette with asymmetric Josephson junctions. Linecut between adjacent minima vs. δ_p for (b) $\Phi_{ext} = \Phi_0/2$, $\alpha = 0$, (c) $\Phi_{ext} = 0.45\Phi_0$, $\alpha = 0$, (d) $\Phi_{ext} = \Phi_0/2$, $\alpha = 0.05$. . . 21

3.3 Single cos2φ plaquette qubit. (a) Schematic of single π-periodic plaquette shunted by capacitance C_{sh}. (b) cos2φ potential at frustration ($\Delta\Phi = \Phi - \Phi_0/2 = 0$) with localized wavefunctions in 0 and π wells. (c) Potential for $\Delta\Phi < 0$, raises π wells above 0 wells, (d) Linear dispersion of 0 and π levels with respect to $\Delta\Phi$ for vanishing tunnel splitting. . 22

3.4 Wavefunctions for ground state doublets in (a) phase basis and (b) charge basis. 22

3.5 (a) Circuit schematic. (b) $4e$ dependence of charge modulation with perfectly symmetric circuit. The blue (red) level corresponds to a superposition of even (odd) numbers of Cooper pairs on the logical island. (c) For a circuit with asymmetries between the two junctions in the plaquette, the charge dependence has $4e$ periodicity for energy levels corresponds to superposition of even (blue) or odd (red) number of Cooper pairs, and the gap a $1e$ remains open. 23

3.6 Double cos2φ plaquettes with ineffective concatenation. (a) Schematic of two series π-periodic plaquettes shunted by capacitance C_{sh} with large capacitance C_{isl} from intermediate island to ground. (b) Contour plot of potential with respect to phase across each plaquette; periodic boundary conditions correspond to topology of a torus. (c) 1D cut of potential between 00 and $\pi\pi$ wells (top) and 0π and $\pi 0$ wells (bottom) at double frustration ($\Delta\Phi_1 = \Delta\Phi_2 = 0$). (d) Linear dispersion of 00 and $\pi\pi$ (0π and $\pi 0$) levels and flat dispersion of 0π and $\pi 0$ (00 and $\pi\pi$) levels for simultaneous scan of plaquette fluxes along $\Delta\Phi_1 = \Delta\Phi_2$ ($\Delta\Phi_1 = -\Delta\Phi_2$) on left (right) plot. (e)Visualizing the 2D potential on the surface of a torus, with the centers of the 00, 0π, $\pi 0$, and $\pi\pi$ wells labeled with black circles. 25

3.7 Double cos2φ plaquettes with effective concatenation. (a) Schematic of two series π-periodic plaquettes shunted by capacitance C_{sh} with small capacitance C_{isl} from intermediate island to ground, (b) Contour plot of potential with respect to phase across each plaquette; periodic boundary conditions correspond to topology of a torus. (c) 1D cuts of potential between 00 and $\pi\pi$ wells along $\phi_1 = \phi_2$ (left) and 0π and $\pi 0$ wells along $\phi_1 = \phi_2 + \pi$ (right) at double frustration ($\Delta\Phi_1 = \Delta\Phi_2 = 0$) with hybridized wavefunctions for symmetric (blue) and antisymmetric (red) superpositions. (d) 1D cut of effective potential along $\phi_1 = -\phi_2$ at double frustration. (e) Quadratic dispersion of even-parity (odd-parity) levels and flat dispersion of odd-parity (even-parity) levels near double frustration for simultaneous scan of plaquette fluxes along $\Delta\Phi_1 = \Delta\Phi_2$ ($\Delta\Phi_1 = -\Delta\Phi_2$) on left (right) plot. 26

3.8 Visualizing the 2D potential on the surface of a torus with the centers of the 00, 0π, $\pi 0$, and $\pi\pi$ wells labeled with solid circles. The red and blue rings joining wells of the same parity indicate the hybridization between states in wells of constant parity. 27

3.9 Sketch of double plaquette transition energy vs. the flux biases of Plaquettes 1 and 2. The transition energy changes the most and with a quadratic dependence with respect to flux in the direction of $\Delta\Phi_1+\Delta\Phi_2$ or $\Delta\Phi_1-\Delta\Phi_2$; the transition energy is flat with respect to each flux bias when the other plaquette is frustrated. This shape is analogous to a doubly folded piece of paper. 27

3.10 (a) Circuit schematic. (b) 2D potential when $\alpha = 0$ with unwrapping the compact phase variables so that they are no longer on a torus, but instead extend to $\pm\infty$. Red lines correspond to hybridization for even-parity wavefunctions, while blue lines correspond to hybridization for odd-parity wavefunctions. (c) 2D potential when α is non-negligible. (d) $\alpha = 0$: Left (right) plot is the 1D cut potential along the direction of hybridization for even- (odd-) parity wavefunctions, and they both have a $\cos 2\varphi$ potential. (e) $\alpha \neq 0$: Left/right plot is the 1D cut of the potential along the direction of hybridization for even- (odd-) parity wavefunctions. The even-parity wavefunctions experience a $\cos 2\varphi$ potential, while the odd-parity wavefunctions experiences a potential with a $\cos\varphi$ component mixed in with the $\cos 2\varphi$ potential. 30

3.11 $4e$ dependence of modulation of Δ_{SA} at double frustration with offset charge bias on intermediate island for (a) symmetric plaquettes with $\alpha = 0$; (b) plaquettes with $\alpha \neq 0$. 31

3.12 Schematic of triple frustration flux dispersion for the two lowest levels. 32

4.1 Circuit schematic. (a) 3-plaquette chip circuit schematic. (b) Schematic of single frustration modeling. (c) Schematic of double frustration modeling. (d) Schematic of triple frustration modeling. 34

4.2 Convergence of transition frequencies at double frustration with respect to the number of states used for each coordinate in the simulation. The red dashed lines correspond to the number of states chosen for each coordinate for subsequent device simulations. Coordinates 1 and 2 are cyclic coordinates and coordinates 3-7 are oscillator coordinates. . . 36

4.3 Single frustration energy levels and flux dispersion. (a) Schematic of potential energy vs. phase across $\cos 2\varphi$ element for single plaquette with symmetric junctions for exact flux frustration (top), and flux-bias 40 mΦ_0 away from frustration (bottom); lines indicate example plasmon (red) and heavy fluxon (blue) transitions. (b) Energy-level dispersion as a function of flux bias relative to single frustration for single plaquette with transitions indicated following earlier color scheme. . 37

4.4 Single frustration energy levels and charge dispersion for $\Delta\Phi = 0$. (a) circuit diagram. (b) Single plaquette energy levels vs charge on the shunt capacitor, when $\alpha = 0$. (c) Single plaquette energy levels vs charge on the shunt capacitor, when $\alpha \approx 0.03$. (d) Energy levels vs. flux when the offset charge on the shunt capacitor is biased at $0e$ (black) and $1e$ (blue). Below 3.5 GHz, the levels for 0e and 1e appear to be on top of each other. (e) Zoomed-in single plaquette energy levels vs charge on the shunt capacitor for the ground-state doublet, when $\alpha = 0$. (f) Zoomed-in single-plaquette energy levels vs. charge on the shunt capacitor for the ground-state doublet when $\alpha \approx 0.03$. 39

4.5 Modeling double plaquette flux dispersion. (a) Sketch of contour plot of effective potential at double frustration accounting for different effective masses plotted as a function of the phase across each plaquette with periodic boundary conditions; lines indicate plasmon (red), plus heavy (blue) and light (magenta) fluxon transitions. (b) Level diagrams around frustration for two concatenated plaquettes with E_J, E_C, E_L, α $=$ 1.75 K, 3.54 K, 1.20 K, 0.031. 41

4.6 Double plaquette flux dispersion with different intermediate island capacitance (a) $C_{isl} = 1$ fF, which results in strong hybridization and $\Delta_{SA} \approx 2.9$ GHz. (b) $C_{isl} = 5$ fF. The hybridization is reduced and $\Delta_{SA} \approx 1.3$ GHz. (c) $C_{isl} = 10$ fF. The hybridization is significantly suppressed. $\Delta_{SA} \approx 0.5$ GHz, and the flux dispersion is close to linear. (d) $C_{isl} = 50$ fF. The hybridization is almost suppressed, the $\Delta_{SA} \approx 0$ GHz, and the flux dispersion is essentially linear. 44

4.7 (a) Circuit schematic. (b) When $\alpha = 0$, the charge modulation for the symmetric/antisymmetric energy levels for even- and odd-parity (The even- and odd parity levels are on top of each other) have $4e$ dependence. They cross at $1e$ and the gap closes because of destructive interference. (c) When α =0.03, the charge modulation for the symmetric/antisymmetric energy levels for even- and odd-parity have $4e$ dependence. They cross at $1e$ and the gap closes for even-parity states, because of destructive interference; at the same time, the splitting remains open for odd-parity states, because of incomplete destructive interference. 45

4.8 Same figure as Fig. 3.10, repeated here for emphasis. (a) Circuit schematic. (b) 2D potential when $\alpha = 0$ with unwrapping the compact phase variables so that they are no longer on a torus, but instead extend to ±∞. Red lines correspond to hybridization for even-parity wavefunctions, while blue lines correspond to hybridization for odd-parity wavefunctions. (c) 2D potential when α is non-negligible. (d) $\alpha = 0$: Left (right) plot is the 1D cut potential along the direction of hybridization for even- (odd-) parity wavefunctions, and they both have a $\cos 2\varphi$ potential. (e) $\alpha \neq 0$: Left/right plot is the 1D cut of the potential along the direction of hybridization for even- (odd-) parity wavefunctions. The even-parity wavefunctions experience a $\cos 2\varphi$ potential, while the odd-parity wavefunctions experiences a potential with a $\cos\varphi$ component mixed in with the $\cos 2\varphi$ potential. 46

4.9 Energy levels vs. flux at double frustration with different intermediate island offset charge. (a,b) $\alpha = 0$: The phase particle can tunnel from 00 well to $\pi\pi$ well along two identical paths leading to Aharonov-Casher interference depending on the enclosed charge, in this case, the offset charge on the intermediate island. (a) When $Q_{isl} = 0e \mod 2e$, constructive interference results in significant tunneling between the 00 and $\pi\pi$ wells. (b) When $Q_{isl} = 1e \mod 2e$, the two paths have destructive interference and tunneling is suppressed, thus $\Delta_{SA} = 0$. (c,d) $\alpha = 0.03$: now the even- and odd-parity wavefunctions experience different potentials. (c) When $Q_{isl} = 0e \mod 2e$, the energy of the ground state doublet is not degenerate at frustration, but instead this degeneracy is moved away from frustration. (d) When $Q_{isl} = 1e \mod 2e1e$, the Δ_{SA} for even-parity energy levels still closes because it experiences a $\cos 2\varphi$ potential, while the Δ_{SA} for odd-parity energy levels remains open because it experiences a potential with a nonzero $\cos\varphi$ component. 48

4.10 Structureless plaquette model. Energy level spectrum with $\alpha = 0$ at triple frustration for simultaneous scan of flux bias to each plaquette along a line from 000 to $\pi\pi\pi$ for C_{isl} = (a) 1 fF, (b) 8 fF, (c) 25 fF, (d) 50 fF. 50

5.1 Device schematic. Plaquettes are in the middle of the figure and connect to the large shunt capacitor. We apply fluxes to different plaquettes through PB01, PB12, PB23, PB30 flux bias lines. We apply fluxes to the two SQUIDs that comprise the SQUID switch through SBC and SBO. We control the offset charges on the shunt capacitor through CB_{sh} and the offset charge on the intermediate island through CB1 and CB2 charge bias lines. 54

5.2 Image from optical microscope with (a) colorized flux lines (blue) and plaquette loops (red), (b) colorized charge lines and intermediate islands. 55

5.3 SEM images of (a) plaquette, (b) junction chain, (c) small junctions. 56

5.4 (a) Q3D simulation image. (b) Zoomed in Q3D image and the highlighted magenta color elements are CB1, CB2, Island 1 and Island 2. Island 2 is simulated including part of the junction chain inductor. . 58

5.5 (a) Circuit schematic for a plaquette embedded in an rf SQUID loop with a shunt capacitor. (b) Resonance frequency at two different fluxes. (c) Resonance frequency vs. plaquette and rf SQUID flux-bias currents. (d) Resonance frequency vs. orthogonalized rf SQUID flux (Φ_{rf}) and plaquette flux (Φ_P). The yellow color in the two-dimensional plots corresponds to higher resonance frequency and the blue color corresponds to lower resonance frequency. The horizontal red dashed lines correspond to the locations of the cuts for the next figure. 61

5.6 (a) Resonance frequency with respect to rf SQUID flux when $\Phi_P = 0$. (b) Resonance frequency with respect to rf SQUID flux when $\Phi_P = 0.5\ \Phi_0$. 63

5.7 (a) Extracted resonance frequency vs. rf SQUID flux when $\Phi_P = 0$. (b) Zoomed-in plot near the upper frequency range. 64

6.1 Fridge setup and and room-temperature electronics setup. 66

6.2 (a) Device image and blue false-color highlighting of the different plaquette flux-bias lines. (b) Readout cavity frequency vs. PB12 flux bias line. (c,d) Scanning different combinations of the plaquette flux lines, while fixing the cavity at the frequency of the resonance when one plaquette is at frustration. The three sets of parallel lines correspond to three plaquettes near frustration. (c) Scanning PB01 and PB30 flux bias lines. (d) Scanning PB12 and PB23 flux bias lines. (e) Scanning cavity transmission vs. the two SQUID flux lines, while fixing the cavity at the frequency of the resonance when one of the SQUIDs is at frustration. The two sets of parallel lines correspond to the two SQUIDs tuning through frustration. 69

6.3 (a) Fine structure observed in a high-resolution scan of the cavity response while varying PB01 and PB12 near double frustration of Plaquettes 1 and 2. (b) Scanning pure Plaquette 1 and pure Plaquette 2 flux using the extracted inductance matrix, with centering at Plaquette 1/2 double frustration. 70

6.4 (a) Device image and blue false-color highlighting of plaquette flux-bias lines. Single frustration spectroscopy measurement vs. flux for (b) Plaquette 1, (c) Plaquette 2, (d) Plaquette 3. 73

6.5 Repeated measurements of the cavity modulation with the offset charge bias to the shunt capacitor island. 74

6.6 (a) Device image and false-color highlighting of charge-bias lines. (b) Plaquette 1/2 double frustration spectroscopy at 17 mΦ_0 vs. offset charge on island between Plaquette 1 and Plaquette 2 with two quasiparticle bands. (c) Plaquette 2/3 double frustration spectroscopy at 11 mΦ_0 vs. offset charge on island between Plaquette 1 and Plaquette 2 with two quasiparticle bands. 75

6.7 Cavity transmission vs. CB1 and CB2 for (a) Plaquette 1/2 double frustration, (b) Plaquette 2/3 double frustration, (c) Plaquette 1/3 double frustration, (d) Plaquette 1/2/3 triple frustration. 76

6.8 Island 1 and 2 charge modulation drift over 11-hour span. Nearly simultaneous measurement for the charge offset on Island 1 and Island 2. The scan is performed by first scanning island charge for Plaquette 1/2 double frustration while keeping Plaquette 3 at 50 mΦ_0. The flux is then pulsed quickly to Plaquette 2/3 double frustration, while keeping Plaquette 1 at 50 mΦ_0. 77

6.9 (a) Device image and false-color highlighting of flux-bias lines. Double frustration spectroscopy vs. flux for (a) Plaquette 1/2 double frustration, (b) Plaquette 2/3 double frustration, (c) Plaquette 1/3 double frustration. The flux for both plaquettes is scanned along the line from 00 to $\pi\pi$ and passing through double frustration. 78

6.10 (a) Device image and false-color highlighting of the flux-bias lines. (b) Spectroscopy vs. flux at triple frustration by simultaenously scanning the three plaquette fluxes along the direction from 000 to $\pi\pi\pi$ and passing through triple frustration. 81

7.1 (a) Device image. (b) Plaquette 2 single frustration fitting. The red lines are plasmon transitions, blue lines are fluxon transitions. The dotted lines are transitions out of the $|0_\pi\rangle$ state. The dash-dotted lines are transitions out of $|1_\pi\rangle$ state. The dashed lines are transitions out of $|2_\pi\rangle$ state. (c) Zoomed-in plaquette 2 single frustration fitting. (d) Fitted energy levels with arrows indicating corresponding transitions from spectroscopy measurements. 84

7.2 Circuit schematic. Same figure as Fig. 4.1. (a) 3-plaquette chip circuit schematic. (b) Schematic of single frustration modeling. (c) Schematic of double frustration modeling. (d) Schematic of triple frustration modeling. 85

7.3 (a) Device image. Single frustration data and fitting of (b) Plaquette 1 , (c) Plaquette 2 and (d) Plaquette 3. The red lines are plasmon transitions, blue lines are fluxon transitions. The dotted lines are transitions out of the $|0_\pi\rangle$ state. The dash-dotted lines are transitions out of $|1_\pi\rangle$ state. The dashed lines are transitions out of $|2_\pi\rangle$ state. . . . 87

7.4 (a) Circuit image. (b) Flux spectroscopy data and fitting of Plaquette 1/2 double frustration. The red lines are the fitted plasmon transitions, the blue lines are the fitted heavy fluxon transitions, the purple lines are the fitted light fluxon transitions. The dotted lines are transitions out of the $|0\rangle$ state of the symmetric energy levels in the even-parity wells. The dash-dotted lines are transitions out of $|1\rangle$ state of the symmetric energy levels in the even-parity wells. The dashed lines are transitions out of $|2\rangle$ state of the symmetric energy levels in the even-parity wells. The solid red line is the plasmon transition between the antisymmetric energy levels in the even-parity well. (c) Calculated energy-level spectrum using the fitting parameters with arrows indicating the various corresponding transitions from the spectroscopy data. 89

7.5 (a) Circuit image. (b) Plaquette 1/2 double frustration charge modulation data of $|0_{ES}\rangle \rightarrow |3_{ES}\rangle$ transition at 17 mΦ_0. The red and blue dotted lines are the fitted transitions that correspond to different quasiparticle parity on intermediate Island 1. (c) Plaquette 2/3 double frustration charge modulation data of $|0_{ES}\rangle \rightarrow |3_{ES}\rangle$ transition at 11 mΦ_0. The red and blue dotted lines are the fitted transitions that correspond to different quasiparticle parity on intermediate Island 2. 90

7.6 (a) Device images and plaquette labeling. Flux spectroscopy data and fitting of (b) Plaquette 1/2, (c) Plaquette 2/3 and (d) Plaquette 1/3. The red lines are the fitted plasmon transitions, the blue lines are the fitted heavy fluxon transitions, the purple lines are the fitted light fluxon transitions. The dotted lines are transitions out of the 0 state of the symmetric energy levels in the even-parity wells. We denote it as $|0_{ES}\rangle$. The dash-dotted lines are transitions out of 1 state of the symmetric energy levels in the even-parity wells, $|1_{ES}\rangle$. The dashed lines are transitions out of $|2_{ES}\rangle$ state. The solid black lines between -20 to -10 mΦ_0 in the Plaquette 2/3 and 1/3 double frustration correspond to transitions involving the cavity: $|0_{ES}, n\rangle \rightarrow |1_{EA}, n-1\rangle$, where n and $n-1$ inside the ket are the photon numbers in the cavity. The solid black lines between -10 to -0 mΦ_0 in the Plaquette 2/3 double frustration correspond to $|0_{OS} \rightarrow 5_{ES}\rangle$ and $|1_{OS} \rightarrow 6_{ES}\rangle$. The solid black lines between -10 to -0 mΦ_0 in the Plaquette 1/3 double frustration correspond to $|0_{OS} \rightarrow 4_{ES}\rangle$ and $|0_{EA} \rightarrow 4_{OA}\rangle$. 91

7.7 (a) Device image. (b) Flux spectroscopy data and fitting of Plaquette 1/2/3. The red lines are the modeled plasmon transitions, the blue line is the modeled heavy fluxon transition, the purple line is the modeled light fluxon transition. The dotted lines are transitions out of the 0 state of the symmetric energy levels in the even-parity wells. 93

7.8 Flux spectroscopy data and fitting of Plaquette 1/2 double frustration. The four orange arrows point to the four transitions we use to estimate the fitted errors. 95

8.1 (a) Modeled energy levels near triple frustration with improved parameters, as described in text. (b) Modeled transitions near triple frustration. (c) Zoomed-in transition plot between 0 to 0.3 GHz. . . 99

8.2 Schematic for implementing protected gates on charge-parity qubit. The $\cos 2\varphi$ element connects to the shunt capacitor or the superinductor through SQUID switches. The SQUID switch between the $\cos 2\varphi$ element and the shunt capacitor is normally closed, and opened briefly for X gates in the phase basis; the SQUID switch between the $\cos 2\varphi$ element and the superinductor is normally open, and closed briefly for Z gates in the phase basis. 101

Chapter 1

Introduction

The field of quantum computing takes advantage of several unique and counterintuitive phenomena of quantum mechanics, including superpositions, interference, and entanglement, to create processors that can dramatically outperform classical computers for solving certain problems. A universal fault-tolerant quantum computer will be able to execute key quantum algorithms, such prime factoring with an exponential speedup over classical processors [1, 2], and unstructured database searching with a quadratic speedup [3]. However, a quantum processor capable of this performance requires error rates that are orders of magnitude lower than current state-of-the-art processors. Nonetheless, recent advances in the field have led to the development of what are referred to as noisy intermediate-scale quantum (NISQ) systems [4]. While not fault-tolerant, these systems are capable of solving important problems in physics [5], chemistry [6, 7, 8, 9], and artificial intelligence [10, 11, 12]. Current state-of-the-art quantum processors have error. rates $\sim 10^{-3}$ [13, 14, 15, 16, 17, 18]; the error rates need to improve by orders of magnitude to run useful quantum algorithms.

The fundamental element in a quantum computer is a quantum bit, or qubit. Building a functional quantum computer requires physical qubits with long coherence, where each qubit can controllably interact with at least neighboring qubits in an array. Implementing quantum error correction to achieve fault-tolerance involves forming logical qubits from a larger number of physical qubits, with stringent requirements on the gate errors, initialization, and readout fidelity for the physical qubits [19]. There are multiple competing approaches for implementing qubits. Besides superconducting qubits [20], other systems include trapped ions [21], semiconductor quantum dots

[22] and photonic qubits [23]. Superconducting qubits are widely used because of their fast gate operations and initialization, high-fidelity readout, and scalability from leveraging microfabrication techniques from the semiconductor processing industry. A comprehensive recent summary of the current state-of-the-art in superconducting qubits can be found in Ref. [24].

Although the coherence of superconducting qubits has improved by over five orders of magnitude in the last two decades [24], the gate error rates are still orders of magnitude larger than what is necessary to build a fault-tolerant quantum processor. Besides errors due to calibration imprecision, gate errors are caused by various sources, such as environmental noise and dissipation, as well as coherent interactions with other quantum systems or levels. Gate errors can be broadly separated into three categories: bit-flip errors, phase-flip errors, and leakage errors. All of these must be suppressed to implement a successful quantum processor. Within the field of superconducting qubits, the transmon qubit has been one of the most successful designs over the past 15 years. Phase-flip errors in transmons due to environmental charge noise are exponentially suppressed because the width of the circuit wavefunction in the charge basis is large [25]. On the other hand, when the frequency of a transmon is made tunable, the device becomes suseptible to phase-flip errors from magnetic flux noise [26]. In addition, the nature of the transmon wavefunctions makes the qubit sensitive to environmental noise at the qubit frequency, thus leading to bit-flip errors. Also, due to the small anharmonicity of transmons, it can be challenging to reduce leakage errors out of the qubit subspace. Fluxonium is another promising superconducting qubit design, with disjoint wavefunctions for the qubit basis states that help to reduce bit-flip errors [27, 28]. However, achieving low phase-flip error rates in fluxonium is challenging because of the susceptibility to flux noise. Because of the relatively large anharmonicity, leakage errors are less problematic for fluxonium qubits, although initialization is more difficult due to the generally small energy scales at the typical operating point. For both transmons and fluxonia, there is no clear path for the simultaneous significant suppression of bit-flip, phase-flip, and leakage errors. To further reduce error rates with the transmon and fluxonium designs, the primary focus involves reducing environmental noise, with significant effort in materials science and device fabrication [29, 30].

With sufficiently low physical qubit error rates, quantum error correction (QEC) can be implemented for working towards a fault-tolerant processor. In general, QEC schemes are based on spreading quantum information across an array of physical qubits to form a logical qubit [31, 32, 33]. Through repeated measurements of stabilizers, which consist of products of operators on multiple qubits in the array, errors due to local noise on individual physical qubits can be detected and corrected. Of course, adding more imperfect physical qubits to run QEC can end up decreasing the overall coherence. Thus, to make QEC effective, the physical qubit error rate must be below a threshold, which depends on the particular QEC scheme. At this point, the error rate in the logical qubits becomes lower than in the physical qubits. The Google Quantum AI team recently demonstrated exponential suppression of bit-flip and phase-flip errors in an array of transmon qubits using the repetition code [18]; the Google group also demonstrated logical qubits based on the surface code with transmons where the logical errors improved as the number of physical qubits was increased [34]. Another superconductor-based scheme involving bosonic codes in superconducting resonators has also demonstrated logical error rates lower than physical error rates [35]. Nonetheless, reducing logical error rates to the level required for fault-tolerance requires thousands of current state-of-the-art physical qubits to form a single logical qubit. This becomes an extremely challenging engineering task. Several years ago, transmons were shown to be capable of reaching the error correction threshold for the surface code approach to QEC [32, 36]

The overhead requirement on the number of physical qubits required to form a logical qubit with a particular error rate decreases with the ratio of the error per physical gate to the QEC threshold [18]. Thus, significant improvements in qubit coherence to reduce physical qubit error rates can have a large impact. Protected qubit designs, with intrinsic protection against local noise, hold promise for moving beyond the error rates that are achievable with transmon or fluxonium qubits. In general, protected qubit designs involve wavefunctions for the qubit basis states that are disjoint in phase space; at the same time, the qubits have suppressed sensitivity to local noise, thus providing suppression of both bit-flip and phase-flip errors [37, 38, 39, 40, 41]. The charge-parity qubit that we are pursuing is one such protected qubit design. In particular, the charge-parity qubit involves built-in stabilizers involving different components of the device. These stabilizers allow for the nonlocal storage of quantum information and enhance the immunity to local noise. In this thesis, I will describe the concept of simultaneously suppressing both bit-flip errors and phase-flip errors with charge-parity qubits.

This thesis is structured as follows. Chapter 2 gives a brief overview of superconducting qubits − introducing transmon and fluxonium, then the protected qubit design. The last section will discuss the common decoherence sources in superconducting qubits. Chapter 3 describes the basic concept of charge-parity qubits. Chapter 5 shows our choice of parameters, device design, circuit-element simulation and device fabrication. Chapter 4 describes the modeling of charge-parity qubits with actual circuit parameters, including details of the complex energy-level dispersion with respect to flux and charge bias. Chapter 6 presents the measurement setup as well as the spectroscopy experimental methods and data. Chapter 7 describes the process for fitting the modeled energy-level spectra to the experimental spectroscopy data. Chapter 8 discusses several potential improvements in future devices that could enable the charge-parity qubit to operate with protection for significant improvements in coherence beyond conventional superconducting qubits.

Chapter 2

Superconducting quantum computation

In this chapter, I describe basic concepts of qubits and their realization with superconducting circuits and Josephson junctions. I introduce the topic of circuit quantum electrodynamics (cQED), which provides a key framework for describing networks of superconducting qubits and photonic modes. I next describe the transmon qubit [25] and fluxonium qubit [27, 28], which represent the current state of the art for superconducting qubit technology. Next, I introduce the charge-parity protected qubit design based on $\cos 2\varphi$ elements, which has the potential to achieve error rates that are significantly lower than have been demonstrated with conventional qubit designs.

2.1 Qubit basics

The fundamental element in a quantum computer is the qubit. A qubit is a two-state quantum system, with basis states $|0\rangle$ and $|1\rangle$, that can be prepared in an arbitrary superposition:

$$|\psi\rangle = \alpha\,|0\rangle + \beta\,|1\rangle\,, \tag{2.1}$$

where α and β are complex numbers with $|\alpha|^2 + |\beta|^2 = 1$; $|\alpha|^2$ and $|\beta|^2$ represent the probability for a measurement to observe the qubit in $|0\rangle$ and $|1\rangle$, respectively. An arbitrary qubit state can be visualized on the Bloch sphere (Fig. 2.1) by expressing

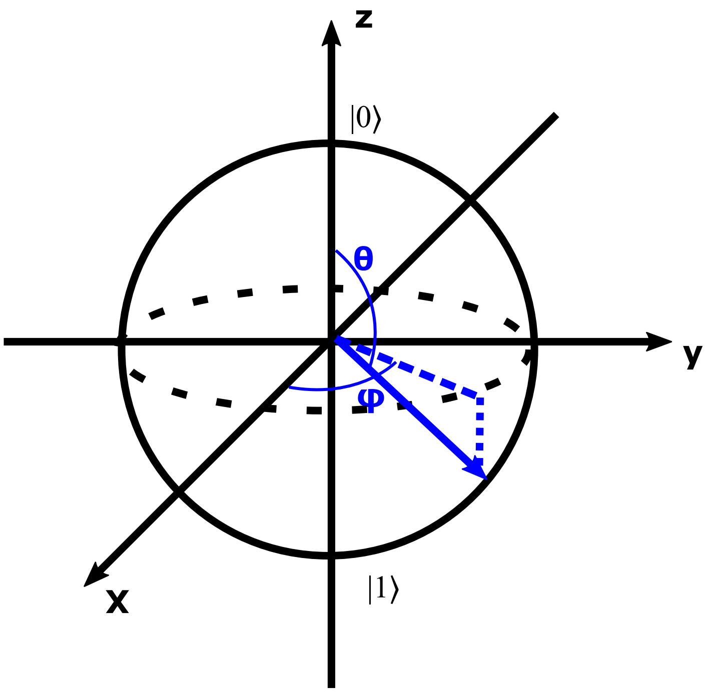

Figure 2.1: Bloch sphere for representing an arbitrary qubit state in terms of the angles θ and ϕ.

the state vector in terms of polar and azimuthal angles θ and ϕ:

$$|\psi\rangle = \cos\frac{\theta}{2}\,|0\rangle + e^{i\phi}\sin\frac{\theta}{2}\,|1\rangle\,. \tag{2.2}$$

Another representation of the qubit state that is particularly useful when considering decoherence is based on the density matrix $\rho = |\psi\rangle\langle\psi|$.

$$\rho = \frac{1}{2}(I + \vec{a}\cdot\vec{\sigma}) = \frac{1}{2}\begin{pmatrix} 1+\cos\theta & e^{i\phi}\sin\theta \\ e^{i\phi}\sin\theta & 1+\sin\theta \end{pmatrix}. \tag{2.3}$$

Here, the I is identity matrix, $\vec{a}$ is the Bloch vector, $\vec{\sigma} = (\sigma_x, \sigma_y, \sigma_z)$, where the σ_i are the Pauli matrices. When $|\vec{a}| = 1$, the qubit is in a pure state and the Bloch vector points on the surface of the Bloch sphere. In this case, the density matrix can be expressed as:

$$\begin{pmatrix} |\alpha|^2 & \alpha\beta^* \\ \alpha^*\beta & |\beta|^2 \end{pmatrix}. \tag{2.4}$$

When $|\vec{a}| < 1$, the Bloch vector does not reach the surface of the Bloch sphere, corresponding in general to a mixed state with a loss of qubit coherence.

2.2 Decoherence

Decoherence of physical qubits plays a critical role in determining gate errors in a quantum processor. In general, decoherence can be described by two timescales that describe the decay of the entries in the density matrix. This can be written in the Bloch-Redfield formalism as [42]:

$$\rho_{BR} = \begin{pmatrix} 1 + (|\alpha|^2 - 1)e^{-\Gamma_1 t} & \alpha\beta^* e^{-\Gamma_2 t} \\ \alpha^*\beta e^{-\Gamma_2 t} & |\beta|^2 e^{-\Gamma_1 t} \end{pmatrix}. \tag{2.5}$$

where

$$\Gamma_1 \equiv \frac{1}{T_1} \tag{2.6}$$

$$\Gamma_2 \equiv \frac{1}{T_2} = \frac{\Gamma_1}{2} + \Gamma_\phi, \tag{2.7}$$

Γ_1 is the relaxation rate corresponding to the decay of the diagonal elements of the density matrix. Γ_1 characterizes the rate at which the qubit loses energy to the environment, thus leading to bit-flip errors. Γ_2 corresponds to the decay rate for the off-diagonal elements of the density matrix, characterizing the rate at which the qubit loses phase information, leading to phase-flip errors. Γ_2 is composed of a contribution from relaxation as well as a pure dephasing rate Γ_ϕ, which results from the random accumulation of dynamical phase due to low-frequency noise in the energy difference between the qubit basis states. Pure dephasing causes a loss of phase coherence, but without energy loss to the environment.

The relaxation rate and pure dephasing rate due to a fluctuating parameter λ can be computed from the following expressions:

$$\Gamma_1^\lambda \propto \left| \langle 0| \frac{\partial \hat{H}_q}{\partial \lambda} |1\rangle \right|^2 S_\lambda(\omega_{10}) \tag{2.8}$$

$$\Gamma_\phi^\lambda \propto \left| \frac{\partial \omega_{10}}{\partial \lambda} \right|. \tag{2.9}$$

Here, the matrix element $\langle 0|\partial \hat{H}_q/\partial\lambda|1\rangle$ is qubit transverse susceptibility to the fluctuating parameter λ, $\partial\omega_{10}/\partial\lambda$ is the qubit frequency first derivative with respect to the parameter λ, and $S_\lambda(\omega_{10})$ is the noise power spectral density at the qubit frequency [43, 42]. Γ_ϕ^λ also depends on the spectrum of fluctuations in λ at low frequencies, and requires a more involved calculation to determine the dephasing rate depending on the particular power spectral density for fluctuations of λ. The power spectral density for different types of noise for for a typical superconducting qubit environment can be found in Ref. [42]. In Sec. 2.5, we discuss some of the dominant noise sources.

Equations (2.7) and (2.8) suggest at least two possible approaches for combatting decoherence. The first way is to engineer the environment so that the noise power spectral density is minimized at the frequencies that affect the qubit. The second way involves engineering the qubit energy-level structure so that the susceptibility to the dominant noise sources is minimized. For superconducting qubits, the first way requires improvements in fabrication, materials, and packaging. In order to apply the second approach to conventional superconducting qubits, as we will see in Sections 2.3.3 and 2.3.4, there is a conflict for simultaneously reducing the susceptibility to relaxation noise and dephasing noise. In Sec. 2.4, we introduce the concept of protected qubit designs, which provide a way to achieve this.

2.3 Superconducting qubits

In this section, I describe superconducting circuits in the framework of cQED. Next, I discuss different types of superconducting qubits and the common decoherence sources that affect superconducting qubits.

2.3.1 Circuit QED

The LC circuit is one of the simplest resonant circuit. The Hamiltonian of a LC circuit is

$$\hat{H} = \frac{\hat{Q}^2}{2C} - \frac{\hat{\Phi}^2}{2L}. \tag{2.10}$$

Here $\hat{Q}$ is the charge operator and $\hat{\Phi}$ is the flux operator, which follow the commutation relation

$$[\hat{\Phi}, \hat{Q}] = i\hbar. \tag{2.11}$$

We can rewrite the Hamiltonian in the energy basis

$$\hat{H} = \hbar\omega_0 \left(\hat{a}^\dagger \hat{a} + \frac{1}{2} \right), \tag{2.12}$$

where $\omega_0 = 1/\sqrt{LC}$, $\hat{a}^\dagger$ and $\hat{a}$ are the raising and lowering operators, respectively. The $\hat{\Phi}$ and $\hat{Q}$ operators are then

$$\hat{\Phi} = \Phi_{\mathrm{zpf}}(\hat{a}^\dagger + \hat{a}), \tag{2.13}$$

$$\hat{Q} = iQ_{\mathrm{zpf}}(\hat{a}^\dagger - \hat{a}). \tag{2.14}$$

The zero-point fluctuations of the $\hat{\Phi}$ and $\hat{Q}$ operators are

$$\Phi_{\mathrm{zpf}} = \sqrt{\frac{\hbar Z_0}{2}}, \tag{2.15}$$

$$Q_{\mathrm{zpf}} = \sqrt{\frac{\hbar}{2Z_0}}. \tag{2.16}$$

Here $Z_0 \equiv \sqrt{L/C}$ is the characteristic impedance of the LC circuit [44].

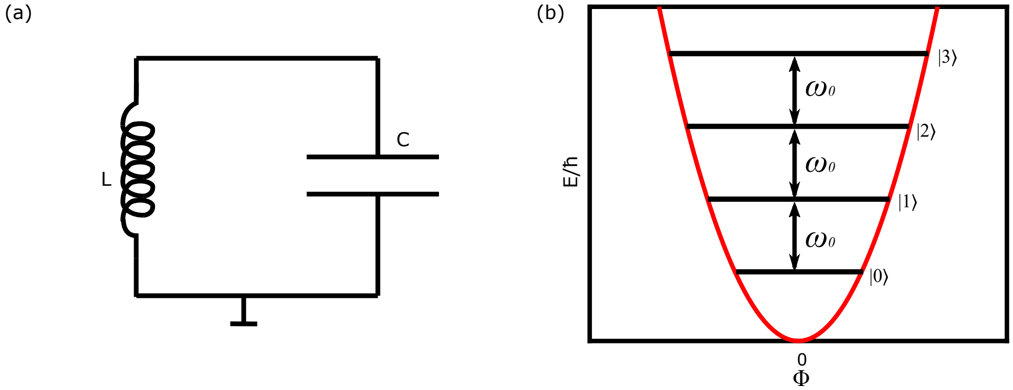

Figure 2.2: (a) harmonic oscillator circuit. (d) parabolic potential.

The harmonic oscillator has evenly spaced energy levels, so we cannot selectively drive the qubit between the $|0\rangle$ state and $|1\rangle$ state [Fig. 2.2(b)]. We will need to introduce nonlinearity to the system to make a qubit with a unique transition between $|0\rangle$ and $|1\rangle$.

2.3.2 Josephson junctions

Josephson junctions are widely used for introducing nonlinearity in superconducting circuit. In superconductors, the nature of scattering between phonons and electrons at low temperatures leads to an attractive interaction between electrons. This causes the electrons to form Cooper pairs, which are able to condense into a macroscopic ground state described by a complex wavefunction with a magnitude and well-defined phase φ [45, 46]. A Josephson tunnel junction consists of an SIS structure, with two superconducting electrodes separated by an insulating barrier with a thickness of the order of 1 nm. The behavior of a Josephson junction is related to the difference in the phase of the superconducting wavefunction on the two sides of the barrier, $\Delta\varphi$, which is often simplified to just φ.

The current-phase relation for a Josephson junction is

$$I = I_0 \sin\varphi. \tag{2.17}$$

Here I is the current through the junction, φ is the phase difference between the wavefunctions in the two superconducting electrodes, and I_0 is the critical current. The critical current is given by the Ambegaokar-Baratoff relation [47]:

$$I_0 = \frac{\pi\Delta}{2eR_n}, \tag{2.18}$$

where R_n is the junction resistance with the electrodes in the normal state. The critical current is the maximum supercurrent that a junction can carry and this depends exponentially on the thickness of the insulating barrier. When applying a voltage across the junction, the phase changes with time

$$V = \frac{\Phi_0}{2\pi}\frac{d\varphi}{dt}. \tag{2.19}$$

Here, V is the voltage across the junction and $\Phi_0 \equiv h/2e$ is magnetic flux quantum.

The inductance of the Josephson junction is given by

$$L_J = \frac{V}{\frac{dI}{dt}} = \frac{\Phi_0}{2\pi I_0 \cos\varphi} = \frac{\Phi_0}{2\pi\sqrt{I_0^2 - I^2}}, \tag{2.20}$$

and we can see it is a nonlinear inductor, since L_J depends on I. The Josephson energy is

$$E = -E_J \cos\varphi \tag{2.21}$$

$$E_J \equiv \frac{\Phi_0 I_0}{2\pi}. \tag{2.22}$$

Now we can replace the linear inductor in the LC circuit [Fig. 2.3(a)], and the Hamiltonian can be rewritten as:

$$\hat{H} = \frac{(2e)^2(\hat{n} - n_g)^2}{2C} - E_J \cos\hat{\varphi}. \tag{2.23}$$

Here, $\hat{n}$ is the Cooper pair number operator, n_g is the offset charge coupled with a bias on a gate electrode, and the phase difference φ is now an operator $\hat{\varphi}$.

In the phase basis, the potential has a $\cos\varphi$ dependence rather than a harmonic form, so the transition frequencies $\omega_{01}, \omega_{12}, \ldots$ are different and we can selectively operate the qubit between the $|0\rangle$ and $|1\rangle$ states [Fig. 2.3(b)]. We thus can use the $|0\rangle$ and $|1\rangle$ states as our computational states.

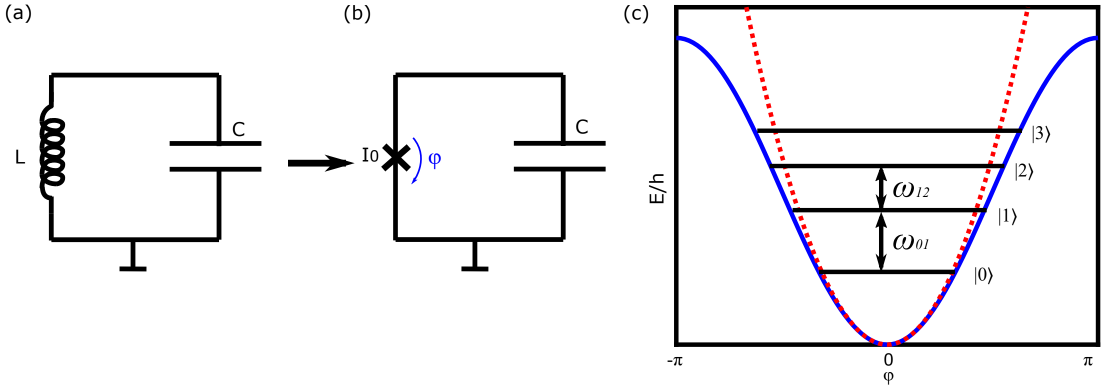

Figure 2.3: (a) harmonic oscillator circuit schematic. (b) replacing the linear inductor with Josephson junction. (c) The potential of the circuit in (b).

2.3.3 Transmon

One of the most promising superconducting qubits currently is the transmon, which was first developed in 2007, as described in Ref. [25]. This qubit type forms the building block for many modern quantum processors, including industrial systems at Google, IBM, Rigetti, IQM, etc. The circuit schematic is shown in Fig. 2.3(b). We can rewrite the Hamiltonian from Eq. (2.23)

$$\hat{H} = 4E_C(\hat{n} - n_g)^2 - E_J \cos\hat{\varphi}, \tag{2.24}$$

where $E_C \equiv e^2/2C$ [25]. In the following chapters, we will define E_C differently as $E_C \equiv (2e)^2/2C$, which follows the convention in the previous protected qubit research [37]. When $E_J >> E_C$, the width of the wavefunction in the charge basis is large [Eq. 2.16], and the charge dispersion of the m^{th} level ϵ_m is exponentially suppressed with E_J/E_C [25]:

$$\epsilon_m \simeq (-1)^m E_C \frac{2^{4m+5}}{m!} \sqrt{\frac{2}{\pi}} \left(\frac{E_J}{2E_C}\right)^{\frac{m}{2}+\frac{3}{4}} e^{-\sqrt{\frac{8E_J}{E_C}}}. \tag{2.25}$$

In the large E_J/E_C limit, the m^{th} energy level is [25]

$$E_m \simeq -E_J + \sqrt{8E_C E_J}\left(m + \frac{1}{2}\right) - \frac{E_C}{12}(6m^2 + 6m + 3), \tag{2.26}$$

and the corresponding 0-1 transition is [25]

$$E_{01} \simeq \sqrt{8E_C E_J} - E_C. \tag{2.27}$$

The transmon is different from a simple LC circuit because E_{01} and E_{12} are different. The anharmonicity measures this difference and is defined as [25]:

$$\alpha \equiv E_{12} - E_{01}, \tag{2.28}$$

and the anharmonicity for the transmon is

$$\alpha \simeq -E_C. \tag{2.29}$$

We can see that reducing the charge dispersion also reduces the anharmonicity, which could make the qubit difficult to control if it approaches a harmonic oscillator too closely. However, while the charge dispersion exponentially depends on $\sqrt{1/E_C}$, the anharmonicity depends on E_C only linearly. We can thus suppress the charge dispersion while keeping the anharmonicity on the order of 100-300 MHz. Typical 0-1 transition frequencies for a transmon are in the 4-5 GHz range.

The transmon with a single junction has a fixed E_{01} and the dephasing of the qubit can be small due to the exponentially suppressed charge dispersion. However, the lack of frequency tunability can cause frequency crowding issues if there are a large number of qubits on the same chip. One way to avoid frequency crowding involves using a superconducting quantum interference device (SQUID) design made by replacing the single junction with two junctions in parallel. The E_J, and thus E_{01}, can be tuned by an external flux Φ [25]:

$$E_J = E_{J\Sigma} \cos\left(\frac{\pi\Phi}{\Phi_0}\right) \sqrt{1 + d^2 \tan^2\left(\frac{\pi\Phi}{\Phi_0}\right)}, \tag{2.30}$$

where $E_{J\Sigma} \equiv E_{J1}+E_{J2}$, $d \equiv (E_{J1}-E_{J2})/(E_{J1}+E_{J2})$, E_{J1} and E_{J2} are the Josephson energy of the two junctions. When $d = 0$, the flux dispersion is large, and the qubit is sensitive to flux noise away from $0\ \Phi_0$. We can increase d to reduce the flux dispersion while keeping a weak tunability [26]. Also, the tunable transmon can achieve high-fidelity two-qubit gates that meet the surface code threshold for quantum error correction [36]. One alternative way to solve the frequency crowding issue is to do laser annealing for adjusting the critical currents of the junctions in single-junction transmons after the initial device fabrication. [48].

The wavefunctions for the two states of the transmon are not disjoint, so it is susceptible to noise processes at the qubit frequency that cause relaxation. Thus, there is no intrinsic protection against bit-flip errors. The way to reduce Γ_1 in transmons involves improving fabrication, materials, and packaging, as mentioned in Sec. 2.2. Also, the small anharmonicity of the transmon can lead to leakage errors during gate operation.

2.3.4 Fluxonium

Fluxonium, due to small coupling between the $|0\rangle$ and $|1\rangle$ state in the phase basis, has small transition matrix element $\left|\langle 0|\partial \hat{H}_q/\partial\lambda|1\rangle\right|^2$, which results in small Γ_1. In addition, the anharmonicity is large. The Hamiltonian of fluxonium is [28, 49]

$$\hat{H} = 4E_C\hat{n}^2 + \frac{E_L(\hat{\varphi} - 2\pi\varphi_{ext})^2}{2} - E_J\cos\hat{\varphi}, \tag{2.31}$$

where $E_L = \Phi_0^2/(2\pi)^2L$, $\varphi_{ext} = \Phi_{ext}/\Phi_0$ and Φ_{ext} is the magnetic flux passing through the loop. The fluxonium is made by connecting a Josephson junction, a linear inductor and a shunt capacitor in parallel [Fig. 2.4(a)]. Typically, the fluxonium is operated at frustration, where $\Phi_{ext} = \Phi_0/2$, as in Fig. 2.4(b). At frustration, the fluxonium has a double well potential and large barrier height, which results in small transition matrix elements between computational states and a high T_1. However, when the flux is moved away from frustration, one well goes up in energy and the other goes down. Because the slope of this flux-dependence $|\partial\omega_{10}/\partial\lambda|$ is large, it is difficult to maintain low dephasing and phase-flip error rates.

Because of the nature of the wavefunctions for transmon and fluxonium qubits, we can see that there is a conflict of simultaneously suppressing both bit-flip errors and phase-flip errors. The transmon has low Γ_ϕ due to charge noise because of the

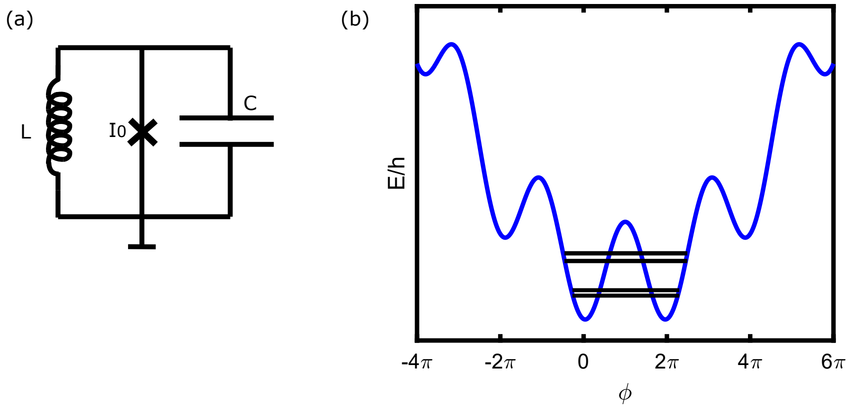

Figure 2.4: (a) Fluxonium circuit diagram. (b) Fluxonium potential.

delocalized wavefunctions in charge space. However, because the $|0\rangle$ and $|1\rangle$ wavefunctions have significant overlap, it is difficult to achieve low Γ_1 without significant efforts to reduce noise at the qubit frequency. The fluxonium with large shunt capacitor and large barrier height has small transition matrix elements between the computational states, but the resulting flux dispersion is large. Reducing the shunt capacitance and the barrier height, the computational states have wavefunctions that are more delocalized, and the flux dispersion is reduced. However, in this case, the transition matrix elements increase and result in a larger Γ_1. Thus, the fluxonium qubit needs some trade-off between suppressing the Γ_1 and Γ_ϕ.

2.4 Protected superconducting qubit

Fault-tolerant quantum computation requires suppression of both bit-flip errors and phase-flip errors. While these two requirements are in conflict for conventional qubits, like the transmon and fluxonium design, more complex superconducting qubits have been considered that in principle could make this possible. The 0-π qubit [50] is one example of such a qubit design.

The 0-π qubit involves a $\cos 2\phi$ potential that is achieved not with a flux bias, but rather with exceedingly large inductances and a cross capacitance. In the ideal parameter regime, which requires quite large inductance, the computational $|0\rangle/|1\rangle$ states for the 0-π correspond to superposition of even/odd numbers of Cooper pairs. The protection again bit-flip error comes from the noise operator not being able to drive transitions between states with different parity.

The protection against dephasing from flux noise comes wavefunction spreading out across multiple minima in the phase coordinate that couples to the external flux. Thus, phase-flip errors due to flux noise are exponentially suppressed with the spread of the wavefunction in this phase coordinate. The qubit is similarly protected against dephasing from charge noise because of the spread of the wavefunction in the charge basis.

However, the ideal parameters for these protected qubit designs are hard to realize. The 0-π qubit requires exceedingly large and precisely matched inductances, as well as a large and compact cross-capacitance. An alternate approach to the 0-π design with relaxed parameter requirements but also reduced protection, the soft 0-π qubit, was demonstrated recently with relaxation times beyond 1 ms and dephasing times of order tens of μs [49].

2.4.1 Charge-parity qubit

The charge-parity qubit, based on the concatenation of $\cos 2\varphi$ elements, can simultaneously suppress bit-flip and phase-flip errors, and its ideal parameters are more achievable with current fabrication techniques. The protection against bit-flip errors is due to the disjoint wavefunctions for the computational states. The exponential protection against flux noise comes from having a large coupling in certain directions in phase space, so that the flux dispersion is exponentially flat in the number of $\cos 2\varphi$ elements. The corresponding Hamiltonian for this process is equivalent to the implementation of quantum stabilizers in hardware. In the coming chapters, I will explain the charge-parity qubit and our experimental realization and modeling of this circuit in detail. Following the convention of Ref. [37], we will define the charging energy as $E_C \equiv (2e)^2/2C$ for the charge-parity qubit.

2.5 Decoherence in superconducting qubits

In this section, I will describe the dominant noise sources that impact relaxation and dephasing in superconducting qubits.

2.5.1 Dielectric loss

Dielectric loss plays a significant role in the energy relaxation of superconducting qubits [51]. Two-level system defects in amorphous dielectric materials can couple to qubit modes and absorb energy from the qubit, thus enhancing qubit relaxation. A lossy dielectric material can be described by a complex permittivity $\epsilon = \epsilon' - i\epsilon''$ (ϵ'' is positive number), where the loss tangent $\tan\delta = \epsilon''/\epsilon'$ measures the dielectric loss [52]. In the case of a typical superconducting qubit, lossy amorphous dielectric layers can be found in various thin oxide layers on the substrate and metal-film surfaces, as well as at the interface between the substrate and metal layers. To estimate the energy decay rate due to dielectric loss, one must account for the electric field participation ratio for each of the components and their respective losses:

$$\Gamma_1 = \omega \sum_i \frac{p_i}{Q_i} + \Gamma_0. \tag{2.32}$$

Here, $1/Q_i = \tan\delta_i$ is the quality factor of each material, p_i is the participation ratio that is given by the electric field energy stored in the ith material over the entire electric energy for the circuit, and Γ_0 is the relaxation rate from mechanisms other than dielectric loss [53].

2.5.2 Charge and flux noise

Charge noise in superconducting circuits can be caused by multiple processes, including fluctuations of microscopic defects having a charge dipole moment, and the impact of high energy particles from background radioactivity [54] that generate electron-hole pairs in the substrate. The first type of noise typically has a $1/f$ power spectrum, with an amplitude at 1 Hz of $\sim 10^{-3}e/\mathrm{Hz}^{1/2}$ [55] and was studied extensively for small mesoscopic devices, such as the Cooper-pair-box [56]. The second type of noise leads to large discrete charge jumps in circuits with larger charge-sensing areas, such as transmons with planar shunt capacitors, and typically has a power spectrum closer to $1/f^2$ [57].

Since 1987, it has been known that superconducting devices at mK temperatures exhibit magnetic flux noise [58]. The power spectrum of this noise is typically close to $1/f$, with an amplitude at 1 Hz that is $\sim 1-5\ \mu\Phi_0/\mathrm{Hz}^{1/2}$ [59, 60]. The mechanism for flux noise has been studied intensively for many years and appears to be related to complex dynamics of adsorbed molecular oxygen, and potentially other contaminants, on the device surfaces [61, 62].

2.5.3 Quasiparticles

From the BCS theory of superconductivity, excitations above the superconducting ground state consist of quasiparticles (QPs), which dissipate energy when they carry current [45]. Excess QPs in the junction electrodes of a qubit enhance the inductive losses and reduce T_1. Quasiparticles can be generated by thermal excitation of Cooper pairs, but for a superconductor such as Al, with $T_c \approx 1.2\,\mathrm{K}$, at mK temperatures, the ratio of QPs to Cooper pairs should be less than 10^{-50}. By contrast, various experiments with superconducting circuits measure this ratio to be more than 40 orders of magnitude larger [63]. QPs can be generated by the absorption of pair-breaking radiation in the superconducting film in the form of photons or phonons. Phonons generated by high-energy particle impacts can create excess QPs and, most importantly, lead to correlated errors between qubits in an array [54, 64]. However, these events occur too infrequently to account for the large QP background observed in superconducting qubits. Nonetheless, the addition of phonon-downconverting structures can significantly reduce the correlated errors from the particle impacts [65, 66]. Recent experiments and theory have identified photon-assisted pair-breaking [67] as a dominant source of excess QPs, in particular, through the absorption of blackbody photons from the qubit environment by spurious antenna modes of typical qubit structures [68, 69]. One mitigation strategy for this mechanism involves the use of more compact designs for the qubit.

Photon shot noise

Because superconducting qubits are typically coupled to a readout resonator that is connected to external circuitry, fluctuations in the photon number in the resonator can cause noise in the dispersive shift of the qubit [70, 71], thus leading to dephasing and phase-flip errors [72]. Photon shot noise can be suppressed by reducing the mean photon number in the readout resonator through improvements in thermalization and filtering.

Chapter 3

Theory of superconducting hardware for implementing quantum stabilizers

In this chapter, I describe how a superconducting circuit can be constructed with built-in stabilizers. First, I introduce the basic element, a π-periodic Josephson plaquette, which we implement using a dc SQUID. Next, I describe how to form a charge-parity qubit from a single plaquette with a large capacitive shunt. However, while such a single-plaquette qubit can have a suppression of bit-flip errors, the large flux dispersion makes it sensitive to phase-flip errors from flux noise. If two plaquettes are concatenated in series with a small capacitance to ground between the plaquettes, quantum fluctuations allow the wavefunctions for the two plaquettes to hybridize. This double plaquette qubit has an effective coupling Hamiltonian that is equivalent to a stabilizer given by: $-(\Delta_{SA_{1/2}}/2)X_1X_2$, where $X_1X_2 = \sigma_x^1 \otimes \sigma_x^2$. This built-in stabilizer leads to a suppression of first order coupling to flux noise and a reduction of the curvature of the flux dispersion near frustration. With the large capacitive shunt, bit-flip errors are also suppressed. We will also discuss the triple plaquette qubit, with three series concatenated plaquettes, where phase-flip errors are further suppressed, with a stabilizer coupling term between the plaquettes given by: $-(\Delta_{SA_{1/2}}/2)X_1X_2 - (\Delta_{SA_{2/3}}/2)X_2X_3$. I will also describe the dispersion of the energy levels with offset charge bias to the various islands, as well as quasiparticle poisoning for different degrees of frustration. As mentioned in Sec. 2.4.1, I will define the charging energy as $E_C \equiv (2e)^2/2C$ for the rest of the thesis.

3.1 π-periodic Josephson elements from dc SQUIDs

In our device, we implement each π-periodic Josephson element with a plaquette formed from a dc Superconducting QUantum Interference Device (SQUID), consisting of two conventional Josephson junctions and a non-negligible loop inductance [Fig. 3.1(a)]. Each junction has a critical current I_0 and $E_J = \Phi_0 I_0/2\pi$; the inductance in each arm of the SQUID L is related to the inductive energy $E_L = (\Phi_0/2\pi)^2/L$. In order to understand the origin of the cos2φ potential, we consider the two-dimensional potential energy landscape as a function of the two junction phases, δ_1 and δ_2, which is determined by E_J, E_L, and the external flux bias Φ_{ext} [73]. For now, we consider symmetric plaquettes where both junction critical currents are identical; later in this section we will consider the effects of junction asymmetry. Following convention for dc SQUIDs we plot the potential energy in terms of the common-mode and differential phase variables: $\delta_p = (\delta_1 + \delta_2)/2$ and $\delta_m = (\delta_2 - \delta_1)/2$. The phase dependence of the Josephson energy for each junction results in a 2D washboard pattern of potential minima. At the same time the inductive energy associated with circulating currents flowing through the inductors corresponds to a parabolic sheet with its minimum along a line running parallel to δ_p. Changing Φ_{ext} shifts where the minimum of this inductive parabolic sheet falls with respect to the minima of the Josephson washboard, and thus determines the pattern of the global minima in the potential.

For a flux bias at unfrustration $\Phi_{ext} = 0 \,\mathrm{mod} \Phi_0$, the minima are centered on $\delta_m = 0$ and are spaced by 2π in δ_p [Fig. 3.1(b)]. Along δ_m, there is only the one minimum at $\delta_m = 0$ [Fig. 3.1(d)], corresponding to no circulating current around the SQUID loop. Along δ_p for $\delta_m = 0$, the potential follows a $\cos\delta_p$ dependence. Thus, at unfrustration, the plaquette behaves like a single Josephson junction with critical current $2I_0$. When flux biased at $\Phi_0/2$, the plaquette exhibits a staggered pattern of energy minima about a line along δ_p for $\delta_m = \pi/2$ [Fig. 3.1(c)]. Figure 3.1(e) shows a linecut along a line between two adjacent minima as a function of δ_m; the two minima correspond to opposite directions of circulating current around the plaquette loop, similar to a flux qubit [74] or fluxonium [27]. However, unlike these other qubits, these plaquettes also have another independent phase degree of freedom from δ_p, which corresponds to the phase drop across the plaquette. Along δ_p, the potential is simply $E_2 \cos 2\varphi$, with sequential minima separated by π [Fig. 3.1(g)], where the energy scale

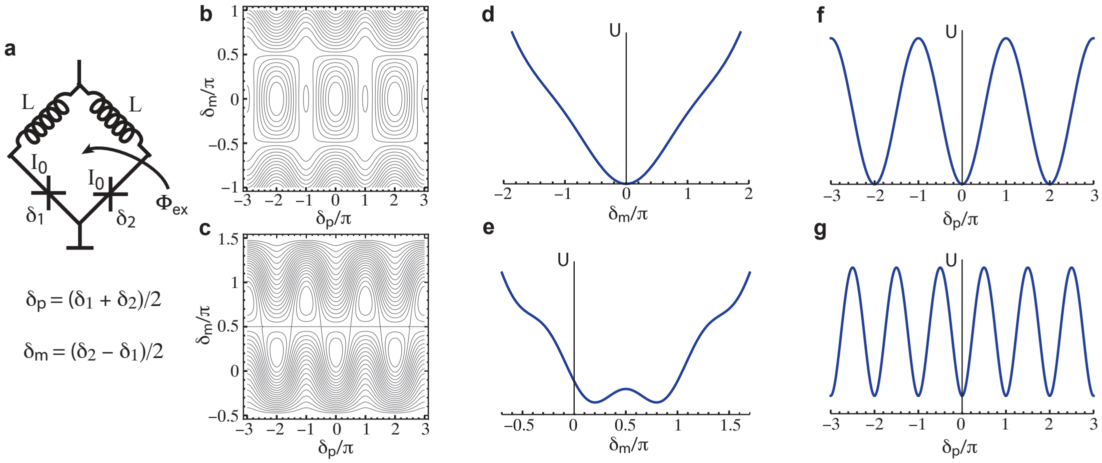

Figure 3.1: (a) Circuit schematic for dc SQUID plaquette. 2D potential as a function of common-mode (δ_p) and differential (δ_m) phase variables at external flux bias Φ_{ext} of (b) 0, (c) $\Phi_0/2$. (d) Linecut along δ_m for $\delta_p = 0$ for $\Phi_{ext} = 0$. (e) Linecut between adjacent minima vs. δ_m for $\Phi_{ext} = \Phi_0/2$. (f) Linecut along δ_p at $\delta_m = 0$ for $\Phi_{ext} = 0$. (g) Linecut between adjacent minima vs. δ_p for $\Phi_{ext} = \Phi_0/2$.

E_2 depends on the Josephson energies of the individual Josephson junctions E_J and the inductive energy of the SQUID loop inductance E_L.

While the behavior described here is generic for any dc SQUID, achieving a $\cos 2\varphi$ potential at frustration with a significant barrier height E_2 requires a sufficiently large ratio E_J/E_L. In the conventional language of dc SQUIDs, screening effects are characterized by the parameter $\beta_L = 2LI_0/\Phi_0 = E_J/\pi E_L$. For SQUIDs in the limit $\beta_L \to 0$ and perfect symmetry, the critical current of the SQUID will modulate to zero at frustration. For such a device, not only is the first-order Josephson energy suppressed, but E_2 will be vanishingly small as well, and thus not support bound states in a $\cos 2\varphi$ potential. In order to have a significant E_2, E_J/E_L must be of order unity. The dc SQUID in Fig. 3.1 has $E_J/E_L = \pi$ to highlight the development of the π-periodicity at frustration.

We next consider deviations from this ideal π-periodic plaquette behavior. With the flux bias moved below (above) frustration ($\Phi_0/2$), the π wells are raised above (below) the 0 wells [Fig. 3.2(c)]. To account for asymmetries between the two junctions in a plaquette we define $\alpha = (E_{J2} - E_{J1})\,/\,(E_{J2} + E_{J1})$, where E_{J1} (E_{J2}) is the Josephson energy of the left (right) junction. With a non-zero α, the common-mode

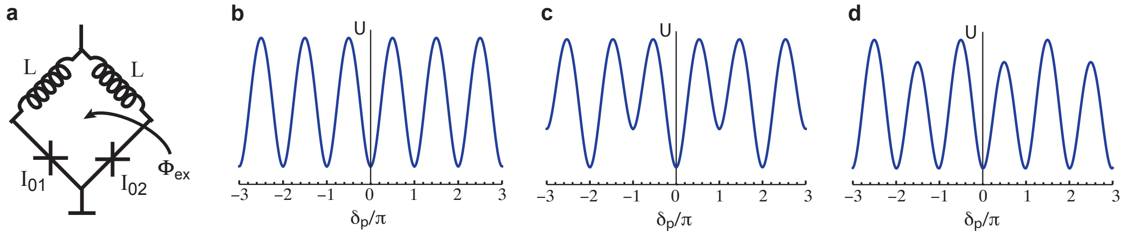

Figure 3.2: (a) Circuit schematic for dc SQUID plaquette with asymmetric Josephson junctions. Linecut between adjacent minima vs. δ_p for (b) $\Phi_{ext} = \Phi_0/2$, $\alpha = 0$, (c) $\Phi_{ext} = 0.45\Phi_0$, $\alpha = 0$, (d) $\Phi_{ext} = \Phi_0/2$, $\alpha = 0.05$.

potential along δ_p for $\Phi_{ext} = \Phi_0/2$ has equal minima for the 0 and π wells, but now the barrier heights between wells become asymmetric.

3.2 Single plaquette qubit

Here we consider the simplest qubit based on a single π-periodic plaquette [Fig. 3.3(a)]. The qubit consists of a superconducting island that is connected to ground by a single plaquette and a large shunt capacitor C_{sh}. Because the phase φ between the logical island and ground is the common-mode phase δ_p, it has cos2φ potential. The phase φ is a compact variable living on a circle, so the 0 well is identical to the 2π well, 4π well, etc. and the π well is identical to the 3π well, 5π well, etc. The Hamiltonian is

$$\hat{H} = E_C^{sh}(\hat{n} - n_g)^2 - E_2 \cos 2\varphi, \tag{3.1}$$

where $E_C^{sh} = (2e)^2/2C_{sh}$ corresponds to the charging energy of the shunt capacitor; C_{sh} is typically large and corresponds to a large effective mass. The second term in Eq. (3.1) corresponds to the $\cos 2\varphi$ potential, with a barrier height $2E_2$. The computational qubit states are formed from the ground state doublet, which in the phase basis is given by symmetric and antisymmetric superpositions of the lowest level in the 0 and π wells. In the charge basis, these states correspond to superpositions of even or odd numbers of Cooper pairs on the logical island (Fig. 3.4). As the wavefunction in the phase basis becomes more localized, the tunnel splitting between the logical states is exponentially suppressed and vanishing in the limit of large C_{sh} [37].

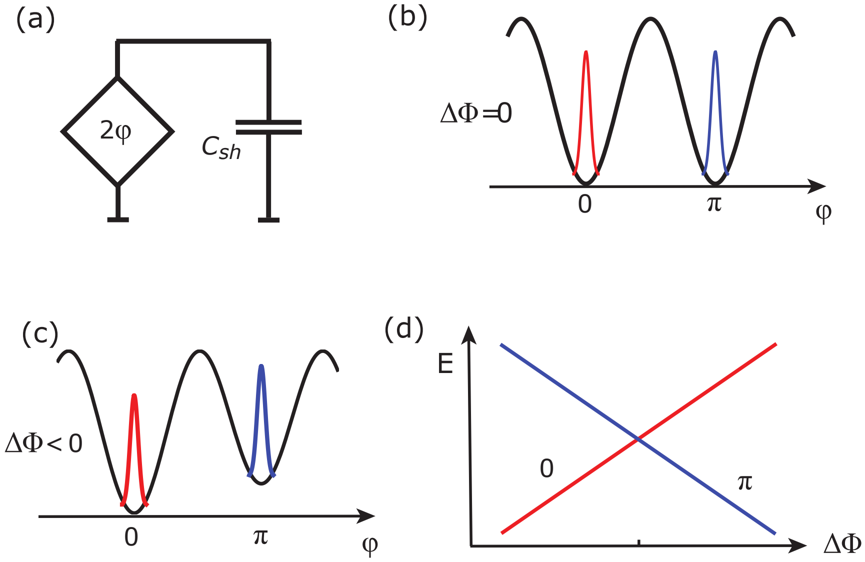

Figure 3.3: Single cos2φ plaquette qubit. (a) Schematic of single π-periodic plaquette shunted by capacitance C_{sh}. (b) cos2φ potential at frustration ($\Delta\Phi = \Phi - \Phi_0/2 = 0$) with localized wavefunctions in 0 and π wells. (c) Potential for $\Delta\Phi < 0$, raises π wells above 0 wells, (d) Linear dispersion of 0 and π levels with respect to $\Delta\Phi$ for vanishing tunnel splitting.

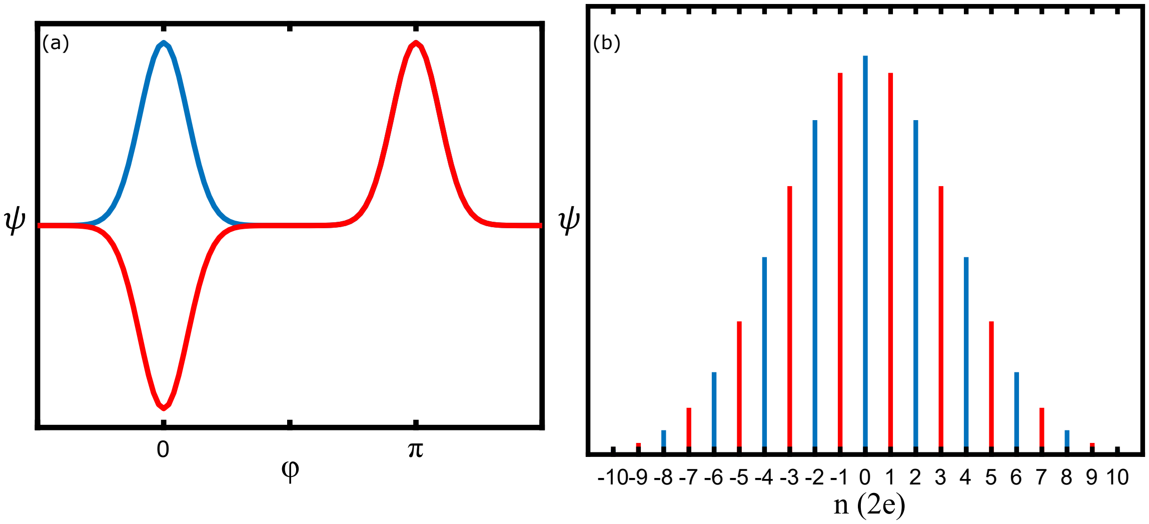

Figure 3.4: Wavefunctions for ground state doublets in (a) phase basis and (b) charge basis.

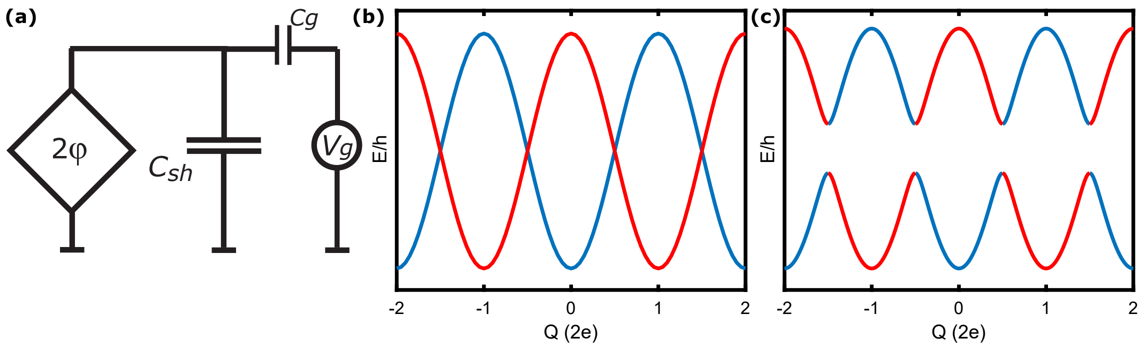

Figure 3.5: (a) Circuit schematic. (b) $4e$ dependence of charge modulation with perfectly symmetric circuit. The blue (red) level corresponds to a superposition of even (odd) numbers of Cooper pairs on the logical island. (c) For a circuit with asymmetries between the two junctions in the plaquette, the charge dependence has $4e$ periodicity for energy levels corresponds to superposition of even (blue) or odd (red) number of Cooper pairs, and the gap a $1e$ remains open.

When the offset charge on the logical island is varied, the splitting of the ground state doublet will modulate, with each level of the doublet exhibiting a $4e$ periodicity [Fig. 3.5(c)]. The charge modulation is an interference effect, as the tunneling can proceed forward or backward in the $\cos 2\varphi$ potential, or clockwise/counterclockwise around the circle, the phase particle acquires a different phase depending on the offset charge on the logical island and the tunneling direction; this is equivalent to Aharonov-Casher interference [75, 76]. The $\cos 2\varphi$ potential causes destructive interference for tunneling of single Cooper pairs across the plaquette, but does allow pairs of Cooper pairs to tunnel on and off the logical island, thus resulting in the $4e$ periodicity. When there is an asymmetry between the two junctions, the potential is no longer a pure $\cos 2\varphi$ [Fig. 3.1(d)]. In the charge basis, the ground state doublet is no longer a pure superposition of even or odd number of Cooper pairs, so at an offset charge of $1e \mod 2e$, the ground state splitting remains nonzero. The charge modulation of the even- or odd parity energy levels is still $4e$. Charge noise in the qubit environment, which caused problematic dephasing for early charge-based superconducting qubits such as the Cooper pair box, is not a problem here since the maximum charge modulation is quite small, less than 1 kHz for our typical target parameters.

As described in Sec. 2.5.2, superconducting qubit chips are subject to flux noise. When the flux fluctuates, the plaquette is not biased at frustration exactly and the π well is raised (lowered) with respect to the 0 well [Fig. 3.3(c)]. The qubit will accumulate a random dynamical phase and cause phase-flip errors. The flux dispersion of a single plaquette is linear in the limit of zero tunnel splitting [Fig. 3.3(d)]. The slope is typically in the order of several hundreds of MHz/mΦ_0. With such a large slope, the single plaquette qubit will have poor dephasing properties.

3.3 Double plaquette qubit

Since the single plaquette qubit does not have protection against phase-flip errors, we need to find a device configuration that has a flatter dispersion with respect to flux to suppress the phase-flip errors, while preserving the suppression of bit-flip errors as in the original single plaquette qubit. We need to delocalize the wavefunctions so that they are not sensitive to flux noise. This can be done by making a chain of two plaquettes as in Fig. 3.6(a). Here, C_{isl} is the capacitance of the intermediate island between the plaquettes to ground.

First, we can start looking at the case when C_{isl} is large, which should not result in effective hybridization [Fig. 3.6(a)]. At double frustration, when two adjacent plaquettes are simultaneously frustrated, there are four minima in the two-dimensional surface defined by the common-mode phase variables for each of the two plaquettes: $00, \pi\pi, 0\pi, \pi 0$ [Fig. 3.6(b)]. This surface has the topology of a torus [Fig. 3.6(e)], since φ for each plaquette is a compact variable with 2π periodicity. Biasing both plaquettes below 0.5 Φ_0 makes 00 the global minimum, while biasing above 0.5 Φ_0 makes $\pi\pi$ the global minimum. Biasing Plaquette 1 below 0.5 Φ_0 and Plaquette 2 above makes 0π the global minimum. Finally, biasing Plaquette 1 above 0.5 Φ_0 and Plaquette 2 below results in $\pi 0$ being the global minimum. Because C_{isl} is large, in this example the two plaquettes do not have effective concatenation and the plaquettes behave independently. The left plot in Fig. 3.6(d) is a sketch of the level structure with the flux bias scanned in the 00-to-$\pi\pi$ direction, which means tuning the flux in both plaquettes together and in the same direction. The red line corresponds to the ground state energy level in the 00 well, the blue line is the ground state energy level in the $\pi\pi$ well, and the green line is the ground state energy level in the 0π or $\pi 0$

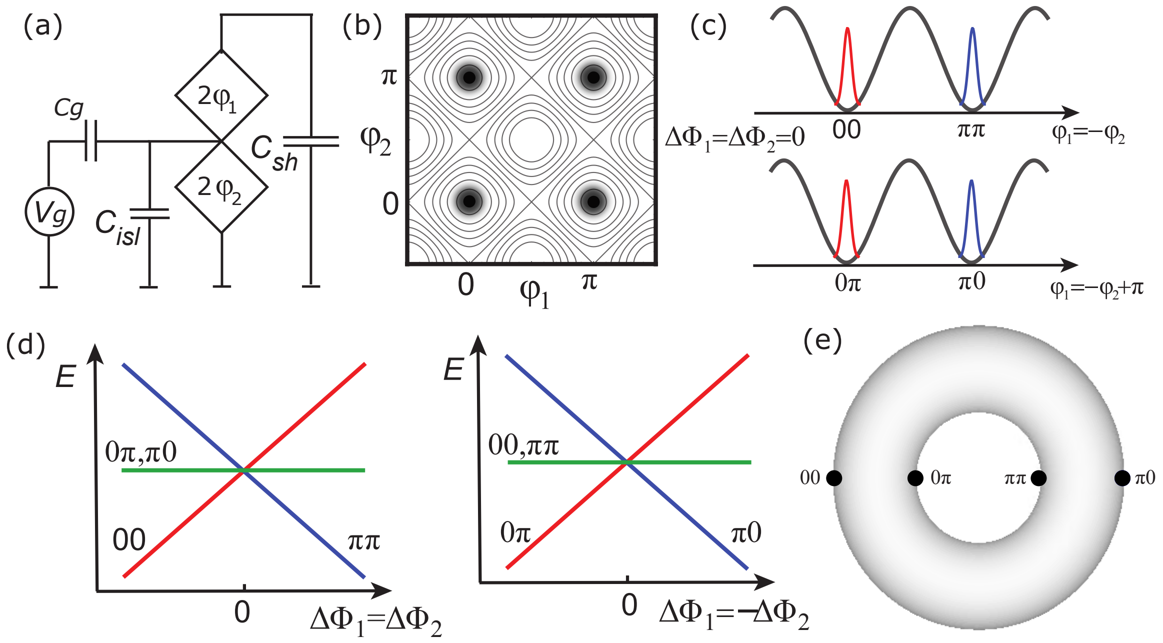
(a)
2φ1
Cg
Csh
2φ2
Vg
Cisl
(b)
π
φ2
0
0
φ1
π
(c)
ΔΦ1=ΔΦ2=0
00
ππ
φ1=−φ2
0π
π0
φ1=−φ2+π
(d)
E
0π,π0
00
ππ
0
ΔΦ1=ΔΦ2
E
00,ππ
0π
π0
0
ΔΦ1=−ΔΦ2
(e)
00
0π
ππ
π0

Figure 3.6: Double cos2φ plaquettes with ineffective concatenation. (a) Schematic of two series π-periodic plaquettes shunted by capacitance C_{sh} with large capacitance C_{isl} from intermediate island to ground. (b) Contour plot of potential with respect to phase across each plaquette; periodic boundary conditions correspond to topology of a torus. (c) 1D cut of potential between 00 and $\pi\pi$ wells (top) and 0π and $\pi 0$ wells (bottom) at double frustration ($\Delta\Phi_1 = \Delta\Phi_2 = 0$). (d) Linear dispersion of 00 and $\pi\pi$ (0π and $\pi 0$) levels and flat dispersion of 0π and $\pi 0$ (00 and $\pi\pi$) levels for simultaneous scan of plaquette fluxes along $\Delta\Phi_1 = \Delta\Phi_2$ ($\Delta\Phi_1 = -\Delta\Phi_2$) on left (right) plot. (e)Visualizing the 2D potential on the surface of a torus, with the centers of the 00, 0π, $\pi 0$, and $\pi\pi$ wells labeled with black circles.

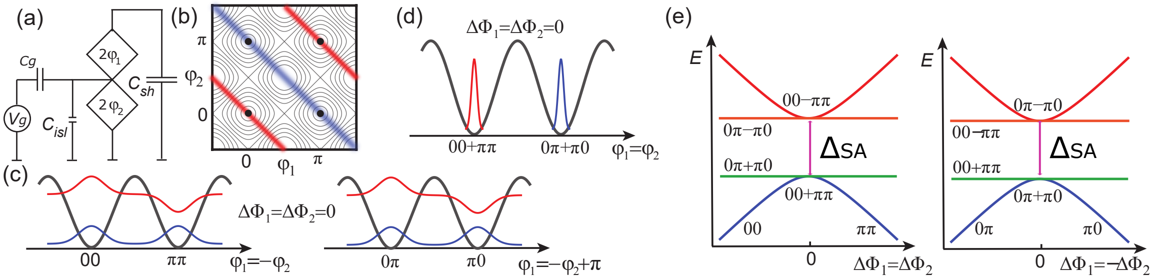
(a)
C_g
$2\varphi_1$
$2\varphi_2$
C_{sh}
V_g
C_{isl}
(b)
π
φ_2
0
0
φ_1
π
(d)
$\Delta\Phi_1=\Delta\Phi_2=0$
$00+\pi\pi$
$0\pi+\pi0$
$\varphi_1=\varphi_2$
(c)
$\Delta\Phi_1=\Delta\Phi_2=0$
00
$\pi\pi$
$\varphi_1=-\varphi_2$
0π
$\pi0$
$\varphi_1=-\varphi_2+\pi$
(e)
E
$00-\pi\pi$
$0\pi-\pi0$
$0\pi+\pi0$
Δ_{SA}
$00+\pi\pi$
00
$\pi\pi$
0
$\Delta\Phi_1=\Delta\Phi_2$
E
$0\pi-\pi0$
$00-\pi\pi$
$00+\pi\pi$
Δ_{SA}
$0\pi+\pi0$
0π
$\pi0$
0
$\Delta\Phi_1=-\Delta\Phi_2$

Figure 3.7: Double cos2φ plaquettes with effective concatenation. (a) Schematic of two series π-periodic plaquettes shunted by capacitance C_{sh} with small capacitance C_{isl} from intermediate island to ground, (b) Contour plot of potential with respect to phase across each plaquette; periodic boundary conditions correspond to topology of a torus. (c) 1D cuts of potential between 00 and $\pi\pi$ wells along $\phi_1 = \phi_2$ (left) and 0π and $\pi0$ wells along $\phi_1 = \phi_2 + \pi$ (right) at double frustration ($\Delta\Phi_1 = \Delta\Phi_2 = 0$) with hybridized wavefunctions for symmetric (blue) and antisymmetric (red) superpositions. (d) 1D cut of effective potential along $\phi_1 = -\phi_2$ at double frustration. (e) Quadratic dispersion of even-parity (odd-parity) levels and flat dispersion of odd-parity (even-parity) levels near double frustration for simultaneous scan of plaquette fluxes along $\Delta\Phi_1 = \Delta\Phi_2$ ($\Delta\Phi_1 = -\Delta\Phi_2$) on left (right) plot.

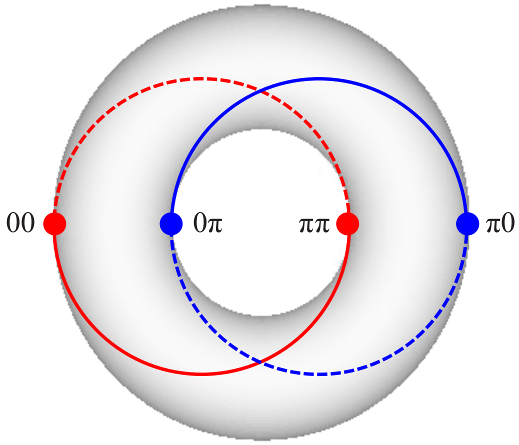

Figure 3.8: Visualizing the 2D potential on the surface of a torus with the centers of the 00, 0π, $\pi 0$, and $\pi\pi$ wells labeled with solid circles. The red and blue rings joining wells of the same parity indicate the hybridization between states in wells of constant parity.

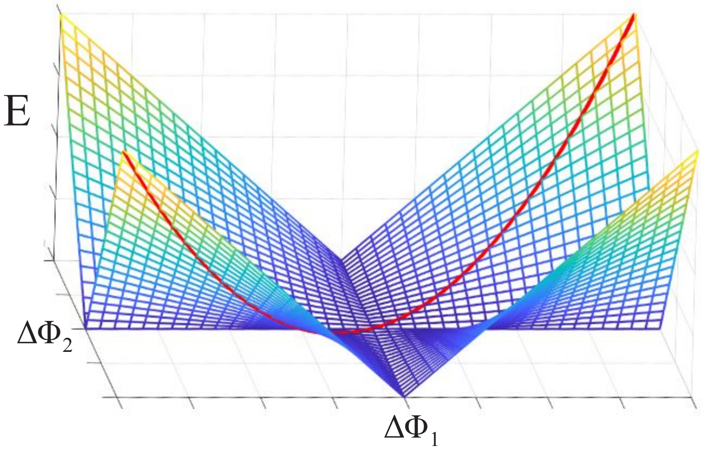

Figure 3.9: Sketch of double plaquette transition energy vs. the flux biases of Plaquettes 1 and 2. The transition energy changes the most and with a quadratic dependence with respect to flux in the direction of $\Delta\Phi_1 + \Delta\Phi_2$ or $\Delta\Phi_1 - \Delta\Phi_2$; the transition energy is flat with respect to each flux bias when the other plaquette is frustrated. This shape is analogous to a doubly folded piece of paper.

wells. When scanning the flux in the even-parity direction (00 to $\pi\pi$), the even-parity levels have a linear flux dispersion, while the odd-parity energy levels have a flat flux dispersion. When scanning the flux in the odd-parity direction (0π to $\pi 0$), the odd-parity levels have a linear flux dispersion, while the even-parity energy levels have a flat flux dispersion. This linear flux dispersion results in dephasing through the same mechanism as for a single plaquette qubit and the qubit will have a high dephasing rate due to flux noise.

However, when C_{isl} is small [Fig. 3.7(a)], the effective mass along the 0π to $\pi 0$ direction is small, and thus the quantum fluctations are large due to significant tunneling between wells with the same parity [Fig. 3.7(b)]. Wavefunctions of the same parity, so, 00 and $\pi\pi$, and 0π and $\pi 0$, hybridize quickly so that the two ground states become $00{+}\pi\pi$ and $0\pi{+}\pi 0$. Because the plaquette phases are compact variables, this potential follows the surface of a torus. The wavefunctions correspond to the even- and odd-parity energy levels can be represented as two separate but interlocking rings on the surface of this torus (Fig. 3.8). The even- and odd-parity energy levels are then the two logical states for this double-plaquette circuit. The hybridization between wells of the same parity means that the ground state for each parity is a symmetric superposition, while there is an excited antisymmetric state; the size of the splitting between these depends on how large E_C^{isl} is, where $E_C^{isl} = (2e)^2/C_{isl}$ [Fig. 3.7(e)]. The tunneling between states of opposite parity correspond to a single extra Cooper pair tunneling on or off the island; this change of parity of the logical island is suppressed by C_{sh}. The large C_{sh} corresponds to a large effective mass along the even-parity to odd-parity directions, so the coupling between the even- and odd-parity ground states is small [Fig.3.7(d)]. The tunnel splitting decrease exponentially with $\sqrt{E_2^{eff}/E_C^{sh}}$. The left plot of Fig. 3.7(e) shows a sketch of a flux scan along the even-parity direction from 00 to $\pi\pi$. The energy levels have the largest curvature along this flux direction, so this direction sets the upper limit of the flux sensitivity (Fig.3.9). Because of strong coupling between wells with the same parity, the even-parity energy level has a large symmetric/antisymmetric gap (Δ_{SA}) at frustration as shown in Fig. 3.7(e). Near frustration, the blue line corresponds to $00{+}\pi\pi$ and the red line corresponding to $00{-}\pi\pi$. The flux dispersion is no longer linear but quadratic. The odd-parity energy levels remain flat and also have two bands correspond to $0\pi{+}\pi 0$ (two degenerate green lines) and $0\pi{-}\pi 0$ (two degenerate orange lines). The right plot of Fig. 3.7(e) shows a sketch of a flux scan in the odd-parity direction from 0π to $\pi 0$. The blue line corresponds to 0π+$\pi 0$ and the red line corresponds to 0π-$\pi 0$. The flux dispersion is again quadratic. The even-parity energy levels remain flat and also have two bands corresponding to 00+$\pi\pi$ (two degenerate green lines) and 00-$\pi\pi$ (two degenerate orange lines). The flux dispersion is quadratic near frustration and the linear term in the flux dispersion vanishes, thus, in the limit of a small amplitude of flux noise, the relative energies of the two qubit states will not fluctuate, and thus the dephasing will be suppressed.

In Fig. 3.10(b), we show the 2D potential when $\alpha = 0$ with unwrapping the compact phase variables so that they are no longer on a torus, but instead extend to $\pm\infty$. Red lines correspond to the direction of hybridization for the even-parity wavefunctions, while blue lines correspond to the direction of hybridization for the odd-parity wavefunctions. We show the 1D cut of the potential of the even- and odd-parity wavefunctions in Fig. 3.10(d), and they both have a $\cos 2\varphi$ potential. Figure 3.10(c) shows the 2D potential when α is non-negligible. In this case, the even-parity wavefunction experiences a $\cos 2\varphi$ potential, while the odd-parity wavefunction experiences a $\cos\varphi$ component mixed in with the $\cos 2\varphi$ potential [Fig. 3.10(e)].

Similar to the single frustration case, the ground state doublet of a perfectly symmetric circuit at double frustration has a $4e$ dependence on the offset charge on the C_{sh} island. When the circuit has asymmetries between the two junctions in a plaquette, it still has a $4e$ dependence on the offset charge on the C_{sh} island, but now the gap remains open at $1e \mod 2e$.

Tuning the offset charge on the intermediate island between the two plaquettes will modulate Δ_{SA} periodically. Similar to the charge modulation of the ground-state doublet splitting with offset charge on the C_{sh} island, this is also equivalent to the Aharonov-Casher effect, because the tunneling paths forward and backward, or equivalently, clockwise or counterclockwise around the ring on the torus, along the constant parity direction can interfere with a phase that depends on the offset charge on the intermediate island. When α is 0, Δ_{SA} for both the even- and odd-parity closes with $4e$ periodicity. Thus, the levels cross at $1e \mod 2e$ [Fig. 3.11(a)]. For $\alpha \neq 0$, the energy levels for one parity will still have Δ_{SA} going to 0 at $1e \mod 2e$, but now Δ_{SA} for the other parity will not fully close [Fig .3.11(b)]. This is equivalent to the wavefunctions for one of the parities still experiencing a $\cos 2\varphi$ potential, while

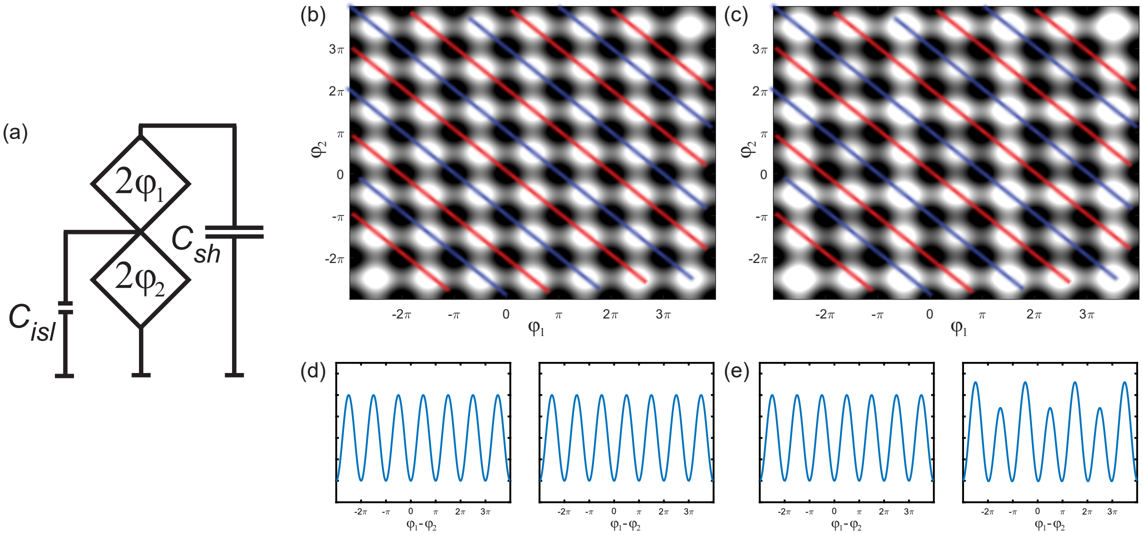

Figure 3.10: (a) Circuit schematic. (b) 2D potential when $\alpha = 0$ with unwrapping the compact phase variables so that they are no longer on a torus, but instead extend to $\pm\infty$. Red lines correspond to hybridization for even-parity wavefunctions, while blue lines correspond to hybridization for odd-parity wavefunctions. (c) 2D potential when α is non-negligible. (d) $\alpha = 0$: Left (right) plot is the 1D cut potential along the direction of hybridization for even- (odd-) parity wavefunctions, and they both have a $\cos 2\varphi$ potential. (e) $\alpha \neq 0$: Left/right plot is the 1D cut of the potential along the direction of hybridization for even- (odd-) parity wavefunctions. The even-parity wavefunctions experience a $\cos 2\varphi$ potential, while the odd-parity wavefunctions experiences a potential with a $\cos\varphi$ component mixed in with the $\cos 2\varphi$ potential.

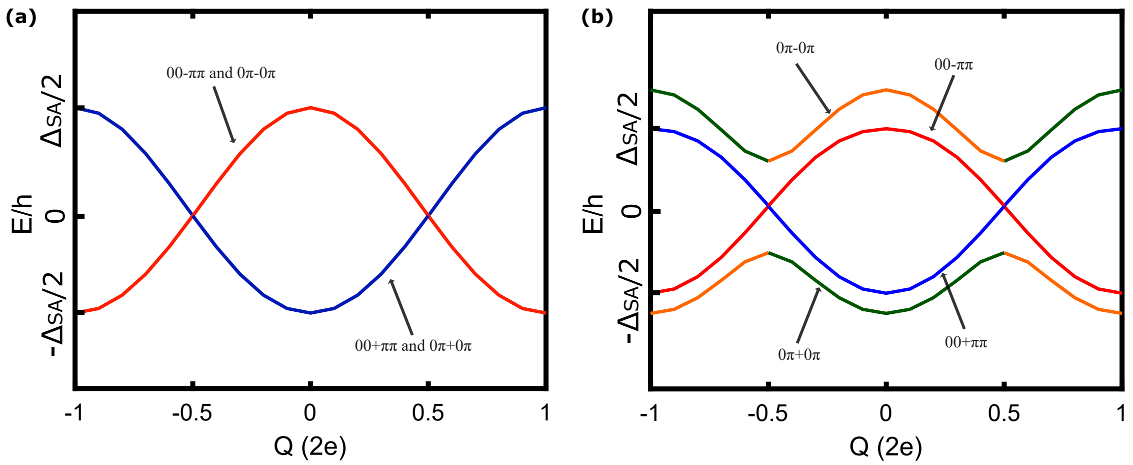

Figure 3.11: $4e$ dependence of modulation of Δ_{SA} at double frustration with offset charge bias on intermediate island for (a) symmetric plaquettes with $\alpha = 0$; (b) plaquettes with $\alpha \neq 0$.

for the other parity, there is a $\cos\varphi$ component mixed in [Fig. 3.10(e)]. Due to charge dynamics in the circuit environment, there can be offset charge jumps and fluctuations on the intermediate island [57, 54]. Thus, it is important to periodically tune the offset charge on the intermediate island to maintain it at $0 \mod 2e$ on a timescale faster than the jumps, which is typically tens of minutes. Because of the flat charge dispersion at $0 \mod 2e$, dephasing due to fluctuations of the intermediate island offset charge will be suppressed.

3.4 Concatenation and XX stabilizer

For two frustrated plaquettes in a chain, each plaquette can be treated like a spin-1/2 particle. The small intermediate island capacitance between the plaquettes corresponds to a coupling between the spins. The effective stabilizer term in the Hamiltonian is then [77]:

$$H_{X_iX_j} = -(\frac{\Delta_{SA_{i/j}}}{2})X_iX_j, \tag{3.2}$$

for plaquettes i and j. X_i is the Pauli σ_x^i matrix for Plaquette i, and $\Delta_{SA_{i/j}}$ is the splitting between the symmetric and antimsymmetric levels at double frustration for Plaquettes i and j. Thus, concatenation of the two plaquettes is equivalent to having an XX stabilizer built in the Hamiltonian, which provides protection against

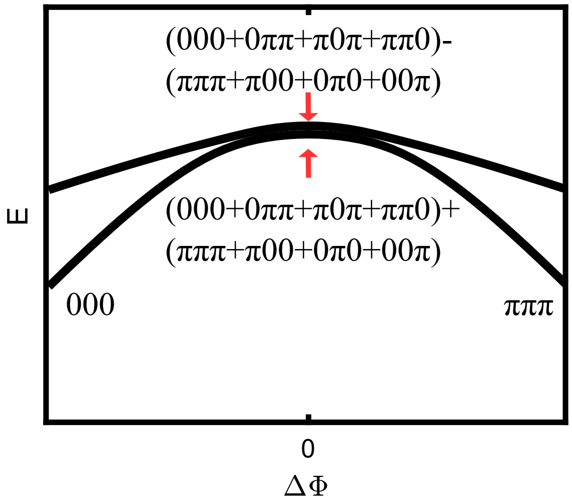

Figure 3.12: Schematic of triple frustration flux dispersion for the two lowest levels.

phase-flip errors.

3.5 Triple plaquette qubit

At triple frustration for a chain of three plaquettes, there will be eight potential wells: 000, 00π, $0\pi0$, $\pi00$, $0\pi\pi$, $\pi0\pi$, $\pi\pi0$, $\pi\pi\pi$. Similar to double plaquette circuit, the energy levels has largest curvature along 000 to $\pi\pi\pi$, and the flux dispersion of the difference between the computational levels along this direction sets the upper limit of the sensitivity the flux noise. At frustration, the computational states are the superposition of even-parity wells and odd-parity wells. A few mΦ_0 away from triple frustration, the lowest energy level corresponds to wavefunction localized in 000 or $\pi\pi\pi$ well. The second lowest levels correspond to superposition of 00π, $0\pi0$, $\pi00$ on the left and $0\pi\pi$, $\pi0\pi$, $\pi\pi0$ on the right. The energy level also has downward flux dispersion, so the transition of 0 state and 1 state flux dispersion is flatter than double frustration. This agrees with the effective coupling Hamiltonian being $-(\Delta_{SA_{1/2}}/2)X_1X_2 - (\Delta_{SA_{2/3}}/2)X_2X_3$ stabilizer. Similar to double plaquette qubit, we can bias the charge on both of the intermediate islands to be $0e$ to suppress the phase-flip errors due to charge noise.

Chapter 4

Numerical modeling of Charge-Parity Qubits

4.1 Introduction to SuperQuantPackage

Numerical modeling of simpler qubit designs, like transmon and fluxonium, is straightforward and computationally inexpensive, because their Hamiltonian has one phase degree of freedom. For the transmon, using ~ 40 charge states is sufficient to model the circuit. The truncated Hilbert space is ~ 40 and the matrix size is $\sim 40 \times 40$. Modeling multi-plaquette charge-parity qubits is much more challenging - our 3-plaquette chip with SQUID switch has eleven phase degrees of freedom, and the truncated Hilbert space is $\sim 2 \times 10^5$. Instead of choosing generalized coordinates manually, we use the SuperQuantPackage [78] to model the energy level spectra of charge-parity qubits.

The SuperQuantPackage software framework was developed by Andrey Klots with the supervision of Lev Ioffe. This package is capable of modeling the energy spectrum of superconducting circuits with arbitrary configurations of Josephson junctions, capacitors, and inductors. The circuit is divided into a series of independent harmonic oscillator coordinates, cyclic coordinates corresponding to islands with quantized charge, and a set of Josephson junctions that facilitate the interaction between the two sets of coordinates. With this choice of basis, the coordinates are maximally separated, and many portions of the Hamiltonian are automatically diagonalized, thus allowing us to extract the eigenvalues with minimal computational expense.

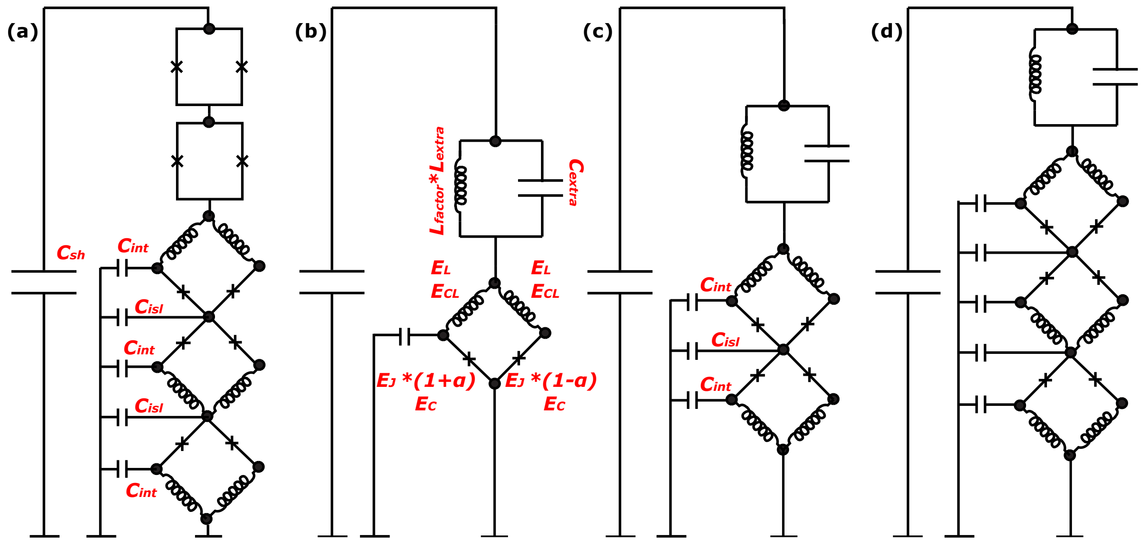

Figure 4.1: Circuit schematic. (a) 3-plaquette chip circuit schematic. (b) Schematic of single frustration modeling. (c) Schematic of double frustration modeling. (d) Schematic of triple frustration modeling.

Despite of this optimization of the numerics, modeling the full circuit of our most complex devices [Fig. 4.1(a)] would require at least several months on most powerful processor in the research group. Thus, we must devise our strategies for simplifying the modeled circuit to make the calculation practical. A plaquette or SQUID biased at unfrustration behaves like a superconducting inductive short with an effective shunt capacitance. For example, when modeling single frustration, we simplify the circuit to a single plaquette connected in series with a LC resonator that represents the other unfrustrated plaquettes and SQUID-switch elements [Fig. 4.1(b)]. The LC resonator inductance and capacitance are shown in Fig. 4.1(b) as L_{extra} and C_{extra}. As shown in Fig. 4.1, each plaquette contains two arms, each having one Josephson junction in series with a linear inductor. The Josephson junction is characterized by E_J and E_C, where E_J is the average energy of the Josephson junctions and E_C is the charging energy set by the junction capacitance. The linear inductor is characterized by E_L and E_{CL}, where E_L is the average inductive energy of the junction-chain inductor and E_{CL} is the charging energy across the junction-chain inductor. From our fabrication uniformity tests, our nominally identical junctions exhibit a spread in E_J of a few percent. We account for this asymmetry between the two junctions in a plaquette with the parameter $\alpha = (E_{JL} - E_{JR})/(E_{JL} + E_{JR})$, with E_{JL} and E_{JR} the Josephson energy of the left and right junction, respectively. Each arm has capacitance to ground and it is characterized by C_{int}. C_{sh} is the capacitance of the shunt. We introduce the parameter L_{factor} to account for variations in L_{extra} due to small flux offsets in the bias of the nominally unfrustrated plaquettes or SQUIDs. After this, we can input the circuit elements in the SuperQuantPackage.

The next step is finding the minimum number of states for each coordinate. We start by using three states for each cyclic coordinate and one state for each oscillator coordinate. We then vary the number of states from 1-20 for each coordinate, while tracking how the transition frequencies change. When the transition frequencies change by less than 5%, we choose the corresponding number of states for that coordinates for next iteration. Using the new number of states, We repeat the same procedure until the process converge. In Fig. 4.2, we show the convergence for each of the coordinates as a function of the number of states for double frustration.

The matrix is typically quite sparse, thus we can use the scipy.sparse.linalg.eigsh() function to find the eigenvalues and eigenvectors efficiently. This function only requires calculating the first few lowest eigenvalues, so the calculation speeds up. Typically, we only care about the first ∼16-32 eigenvalues, but when we need to calculate the transitions involving the cavity, we need to calculate the first 40 eigenvalues. SuperQuantPackage also allows inputting offset charge at specific nodes. To input offset flux in a loop, we need to introduce an inductor, then vary the phase across this inductor. The corresponding inductance needs to be small enough so that the mode couples to this inductor is at a sufficiently high energy that it does not affect the energy levels of interest. The parasitic capacitance of this inductance needs to be several order larger than the inductance, so that the characteristic impedance is small and the wavefunction is localized in the phase space and the phase slip across the inductor is suppressed. The typical inductance and capacitance we use is 10^{-5} pH and 1 fF.

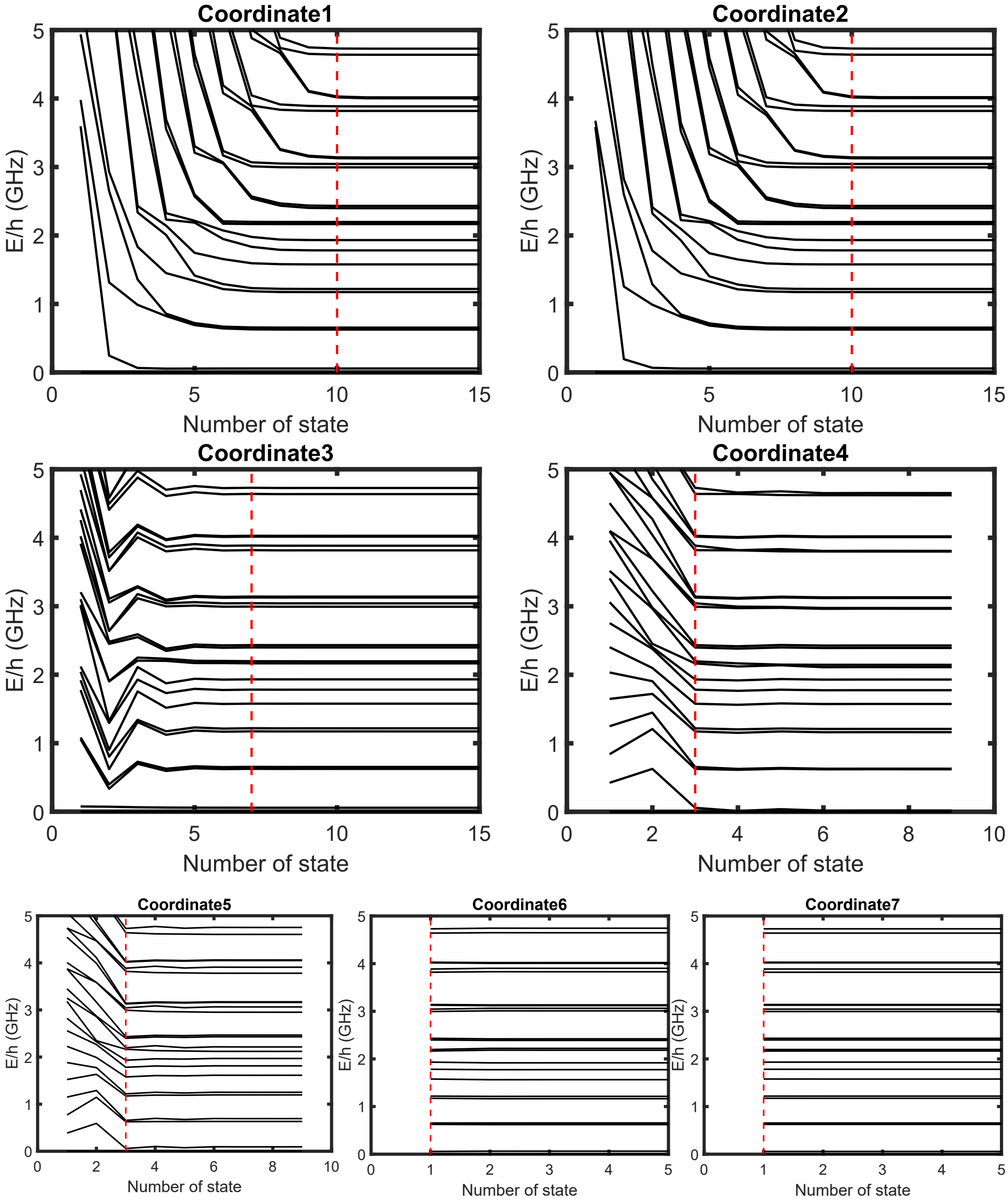

Figure 4.2: Convergence of transition frequencies at double frustration with respect to the number of states used for each coordinate in the simulation. The red dashed lines correspond to the number of states chosen for each coordinate for subsequent device simulations. Coordinates 1 and 2 are cyclic coordinates and coordinates 3-7 are oscillator coordinates.

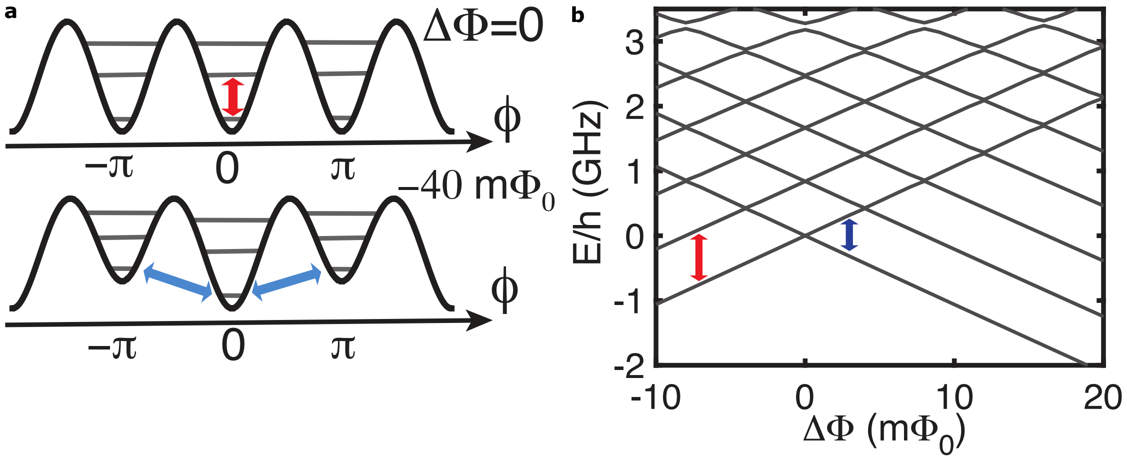

Figure 4.3: Single frustration energy levels and flux dispersion. (a) Schematic of potential energy vs. phase across $\cos 2\varphi$ element for single plaquette with symmetric junctions for exact flux frustration (top), and flux-bias 40 mΦ_0 away from frustration (bottom); lines indicate example plasmon (red) and heavy fluxon (blue) transitions. (b) Energy-level dispersion as a function of flux bias relative to single frustration for single plaquette with transitions indicated following earlier color scheme.

4.2 Single frustration modeling

In order to explore the implementation of stabilizers, we need to investigate the flux dispersion of the energy bands for different frustration conditions of the various plaquettes. First, we model single frustration by considering a single plaquette connected in series with an LC circuit [Fig. 4.1(b)]. Doing a similar convergence test as shown in Fig. 4.2, we assign 31 states to the one cyclic coordinate that is necessary here; we assign 15, 15, and 1 states to three oscillator coordinates. We only calculate the lowest 32 eigenstates to speed up the calculation.

4.2.1 Single frustration flux dispersion modeling

Using the single plaquette model, we plot the numerically modeled dispersion of the energy levels with flux for our experimental Plaquette 2 parameters in Fig. 4.3(b), where the flux bias of one plaquette is scanned near $\Phi_0/2$, while the other plaquettes and SQUID switch are kept at unfrustration with a flux bias of 0. The 0 and π wells both have ~ 7 energy levels below the barrier height of ~ 4.5 GHz [Fig. 4.3(a)]. If tunneling is non-negligible, for flux bias points where levels line up between the 0 and π wells, for example, at frustration, the wavefunctions will become doublets, with a symmetric and antisymmetric superposition, split by the tunneling energy. Following convention, we refer to transitions between levels in the same well, which disperse with the same sign with respect to flux, as *plasmons*; transitions between wells with opposite parity on the logical island that disperse with flux with the opposite sign are *heavy fluxons* because of the vanishingly small gap for low-lying level crossings due to the large effective mass from C_{sh}. The *plasmon* transitions depend on the shape of the potential, so they disperse gradually with flux. The *heavy fluxon* transitions depend on the relative height between the 0 well and π well, so they vary quickly with flux with a linear dispersion at single frustration; the typical slope of the fluxon transitions for our device parameters is $\partial f_{0L\to 0R}/\partial\Phi_{ext} \approx 200$ MHz/mΦ_0. With such a large slope, this circuit does not have protection against phase-flip errors caused by dephasing from flux noise. Our computational states are the ground state doublet and their separation is less than 100 kHz, so the coupling between the 0 well and π well is small. This corresponds to a small transition matrix element and long T_1 and thus a suppression of bit-flip errors.

4.2.2 Single frustration charge dispersion modeling

When the plaquette is biased at $\Phi_0/2$ and the offset charge on the logical island (Q_{sh}) is at $0e$, the lower energy state of the ground-state doublet corresponds to a symmetric superposition $|0\rangle + |\pi\rangle$ in the phase basis, and a superposition of even numbers of Cooper pairs on the logical island in the charge basis. As described in Ch. 3, the higher energy state of the ground-state doublet corresponds to an antisymmetric superposition $|0\rangle - |\pi\rangle$ in the phase basis, and a superposition of odd numbers of Cooper pairs on the logical island in the charge basis. When Q_{sh} is varied, the splitting of the ground-state doublet will modulate periodically due to an analogue of Aharonov-Casher interference, as described in Sec. 3.2. The energy levels for the symmetric/antisymmetric state have a $4e$ periodicity and cross at $\pm 1e \mod 2e$. In the phase basis, because the phase is a compact variable, the phase particle can tunnel either forward or backward from the 0 to the π wells, corresponding to a pair of Cooper pairs tunneling on or off the logical island. When $Q_{sh} = 0e \mod 2e$, tunneling along

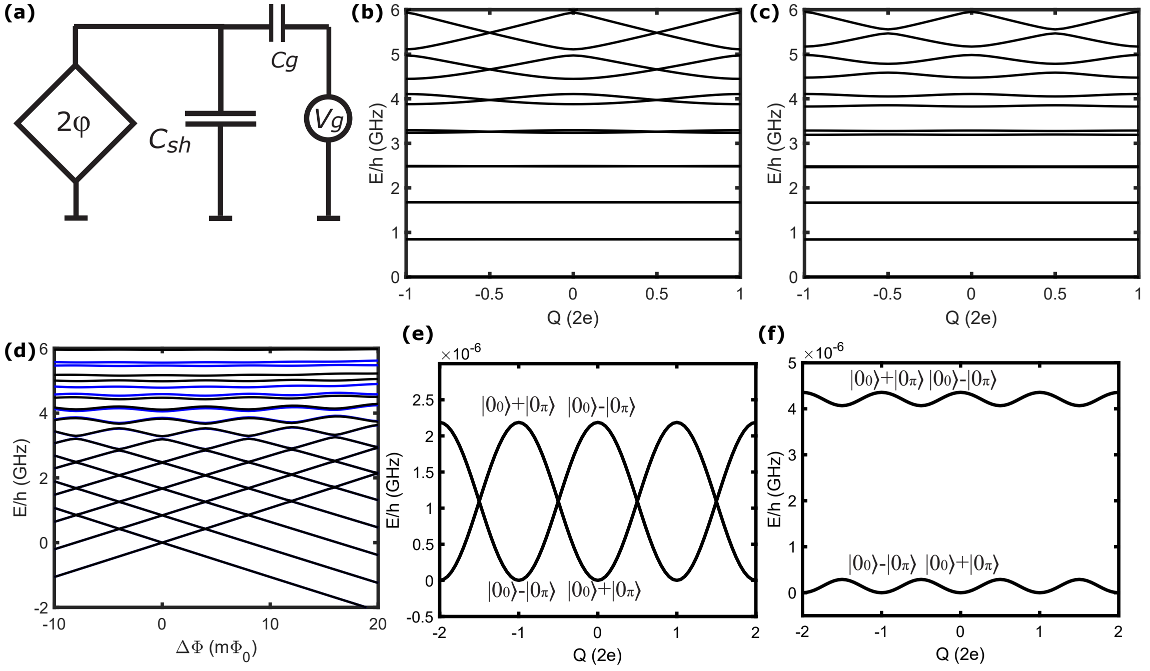

Figure 4.4: Single frustration energy levels and charge dispersion for $\Delta\Phi = 0$. (a) circuit diagram. (b) Single plaquette energy levels vs charge on the shunt capacitor, when $\alpha = 0$. (c) Single plaquette energy levels vs charge on the shunt capacitor, when $\alpha \approx 0.03$. (d) Energy levels vs. flux when the offset charge on the shunt capacitor is biased at $0e$ (black) and $1e$ (blue). Below 3.5 GHz, the levels for 0e and 1e appear to be on top of each other. (e) Zoomed-in single plaquette energy levels vs charge on the shunt capacitor for the ground-state doublet, when $\alpha = 0$. (f) Zoomed-in single-plaquette energy levels vs. charge on the shunt capacitor for the ground-state doublet when $\alpha \approx 0.03$.

these two paths exhibits constructive interference so that the splitting is maximum. When $Q_{sh} = 1e \mod 2e$, tunneling along the two paths interfere destructively and the splitting goes to zero. This vanishing of the splitting at $1e$ only occurs when the two junctions in the plaquette are perfectly symmetric [Fig. 4.4(b),(e)]. However, for the fabricated devices, there is always some variation between nominally identical junctions, with α typically between 0.01-0.03 for our plaquette junctions. For non-zero α, the corresponding potential is no longer a pure $\cos 2\phi$, but has a residual $\cos\varphi$ component (Fig. 3.2). This results in the tunneling along the two paths no longer being equivalent, and thus the destructive interference at $Q_{sh} = 1e \mod 2e$ is incomplete and the splitting remains non-zero. In the charge basis, this means there is the possibility that a single Cooper pair can tunnel on or off the logical island. Thus, the lower energy state no longer corresponds to purely a superposition of even numbers of Cooper pairs, but can also have have a small mixture of odd numbers of Cooper pairs. Similarly, the higher energy state is no longer purely a superposition of an odd numbers of Cooper pairs, but can include a small mixture of even numbers of Cooper pairs. The nonzero single Cooper pair tunneling that arises for $\alpha \neq 0$ results in a gap opening at $1e \mod 2e$ [Fig. 4.4(c),(f)]. Figure 4.4(d) shows the energy level flux dispersion when offset charge is biased at $0e$ (black) and $1e$ (blue) with $\alpha \approx 0.03$. The large C_{sh} suppresses the tunneling for the low-lying states, so, when combined with the non-zero junction assymetry, the charge-modulation of these levels is small and difficult to distinguish in our experimental data, which will be presented in Ch. 6. Nonetheless, the higher levels near the top of the barrier and above still tune strongly with offset charge. Because these higher levels are strongly coupled to the readout cavity, we are able to observe a clear modulation of the cavity signal.

4.3 Double frustration modeling

In this section, I describe the modeling of the flux- and charge-dispersion of the energy-level spectrum near double frustration, while the third plaquette and SQUID switch elements are remained at unfrustration. As explained earlier, we model these unfrustrated elements as a single LC circuit in series with the two plaquettes that are modeled near double frustration Fig. [4.1(c)].

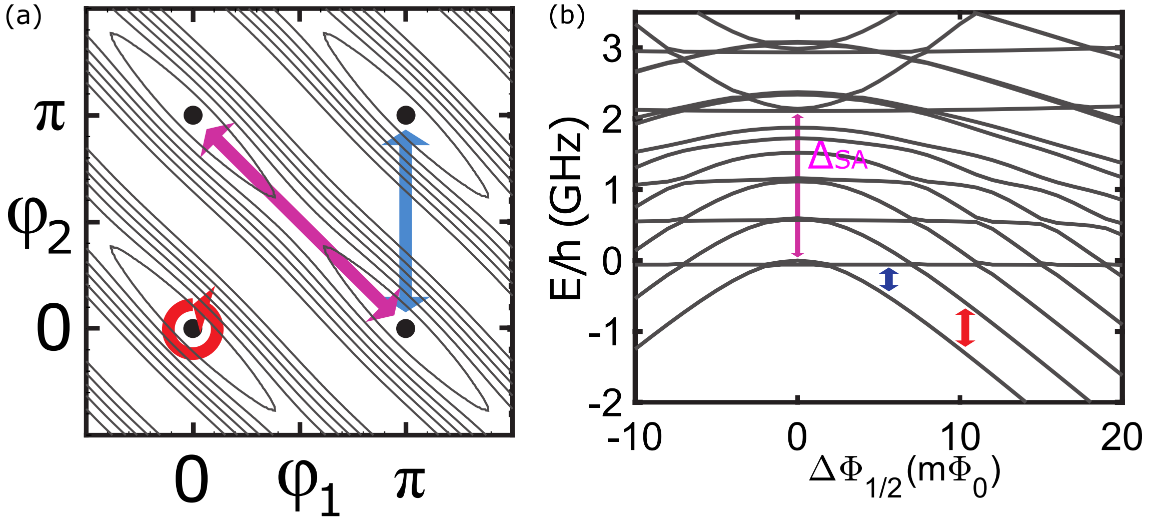

Figure 4.5: Modeling double plaquette flux dispersion. (a) Sketch of contour plot of effective potential at double frustration accounting for different effective masses plotted as a function of the phase across each plaquette with periodic boundary conditions; lines indicate plasmon (red), plus heavy (blue) and light (magenta) fluxon transitions. (b) Level diagrams around frustration for two concatenated plaquettes with E_J, E_C, $E_L, \alpha = 1.75\,\mathrm{K}$, $3.54\,\mathrm{K}$, $1.20\,\mathrm{K}$, 0.031.

4.3.1 Double frustration flux dispersion modeling

The potential energy landscape for the two frustrated plaquettes has four wells in the two-dimensional space of the two plaquette phases. Because the plaquette phases are compact variables, this potential follows the surface of a torus (Fig. 4.8). If the capacitance to ground of the intermediate island C_{isl} is sufficiently small, with a charging energy $E_C^{isl} = (2e)^2/2C_{isl} \sim E_J$, quantum fluctuations of the island phase along the direction between wells of the same parity lead to hybridization of $00/\pi\pi$ and $0\pi/\pi 0$ wells. In this case, the levels with the same parity of the plaquettes develop a splitting near double frustration, with the ground states corresponding to symmetric superpositions: $|00\rangle + |\pi\pi\rangle$ for even parity, and $|0\pi\rangle + |\pi 0\rangle$ for odd parity. In Fig. 4.5(a), we plot out the effective potential at double frustration accounting for different effective masses plotted as a function of the phase across each plaquette with periodic boundary conditions. The red lines correspond to plasmon transitions, the blue lines correspond to heavy fluxon transitions between hybridized states with different parities, and the magenta lines correspond to light fluxon transitions between the symmetric and antisymmetirc states with the same parity.

We plot numerically modeled energy-level diagrams for our experimental device parameters at double frustration, where Plaquettes 1 and 2 are biased near $\Phi_0/2$ and Plaquette 3 is biased at Φ_0 in Fig. 4.5(b). The bias flux in the two plaquettes is varied simultaneously in the direction from where 00 is the lowest well to where $\pi\pi$ is the lowest well. We begin our description by considering the lowest energy level with a downward parabolic dispersion, corresponding to the ground state in the 00 ($\pi\pi$) well for $\Delta\Phi$ well below (above) zero. When we bias the two plaquettes near double frustration, the large E_C^{isl} results in large quantum fluctuations between the 00 and $\pi\pi$ wells; in an effective potential picture, the barrier between the 00 and $\pi\pi$ wells is reduced, while the large C_{sh} across the plaquette chain maintains a large effective barrier between the $00/\pi\pi$ wells and the $0\pi/\pi0$ wells [Fig. 4.5(a)]. The wavefunctions are strongly hybridized between the 00 and $\pi\pi$ wells resulting in the qubit ground state being $|00\rangle + |\pi\pi\rangle$ and a large gap Δ_{SA} between the symmetric and antisymmetric levels. Because the other logical state is the $|0\pi\rangle + |\pi0\rangle$ level, which is flat with respect to this particular direction in flux space, the heavy fluxon transition near double frustration exhibits quadratic flux dispersion, compared to linear dispersion for single frustration.

The antisymmetric energy level from the hybridization of the states in the 00 and $\pi\pi$ wells is visible near 2 GHz with an upwards parabolic flux dispersion near frustration Fig. 4.5(b). When the flux is biased away from double frustration in the negative direction, this energy level corresponds to the qubit in the ground state of the $\pi\pi$ well; similarly, in the positive flux direction, the qubit is in the ground state of the 00 well. At frustration, this level corresponds to the $|00\rangle - |\pi\pi\rangle$ state.

The second lowest energy level near frustration has almost flat flux dispersion, and it corresponds to the wavefunctions hybridized between the 0π and $\pi0$ wells. When the flux is biased away from double frustration in the negative direction, the 0 well potential in each plaquette goes down and the π well potential goes up, and vice versa for flux bias in the positive direction. Thus, the flux dispersion of this hybridized odd-parity level is nearly flat.

There are an additional set of energy levels with a downward parabolic shape flux dispersion, which correspond to plasmon energy levels within the even-parity wells.

The set of energy levels with flat flux dispersion correspond to plasmon energy levels within the odd-parity wells. Near frustration, when the energy levels are about 2 GHz above the ground states, they are so close to the top of the barrier that the tunneling between the even or odd-parity states becomes significant. We can see an example of this at 8 mΦ_0 and 1 GHz, where there is an obvious anticrossing gap when the even-parity energy level crosses the odd-parity energy level.

A key feature of this circuit is that we can can engineer the effective mass along the directions of constant parity to be small, which results in a significant gap opening and flatter bands at double frustration, including the heavy fluxons between states of opposite parity. The wavefunction hybridization in such a direction corresponds to an effective coupling Hamiltonian $-(\Delta_{SA_{1/2}}/2)X_1X_2$, which is equivalent to implementing an XX stabilizer in superconducting hardware. This results in flatter flux dispersion and provides protection against dephasing due to flux noise. At the same time, the large C_{sh} still suppresses tunneling between the logical states of opposite parity. The modeled gap between the lowest even- and odd-parity levels is $\sim$100 MHz because the non-zero α results in differences in the potential for the even- and odd-parity wavefunctions (Sec. 3.3). It is important to maintain small α so the multi-plaquette circuit preserves the exponential protection against bit-flip errors.

4.3.2 Double frustration flux dispersion vs. intermediate island capacitance

We modeled double frustration flux dispersion with different intermediate island capacitance, and we present some of these results in Fig. 4.6. When $C_{isl} = 1$ fF, the effective mass is small along the magenta line in Fig. 4.5(a), and the quantum fluctuations are large in this direction. The wavefunction is hybridized strongly between the 00 and $\pi\pi$ wells, resulting in a large $\Delta_{SA} \approx 2.9$ GHz and rather flat ground-state energy band [Fig. 4.6(a)]. The ground state energy band is relatively flat near frustration. When $C_{isl} = 5$ fF, the effective mass along this direction is larger, but there is still somewhat effective hybridization between the 00 and $\pi\pi$ well [Fig. 4.6(b)]. In this case, $\Delta_{SA} \approx 1.3$ GHz, and the energy band curvature is larger. When $C_{isl} =$ 10 fF, the hybridization is significantly weaker [Fig. 4.6(c)]. $\Delta_{SA} \approx 0.5$ GHz and the antisymmetric level is now lower than the first excited plasmon state. Also, the energy bands have a nearly linear dispersion near double frustration. When $C_{isl} =$

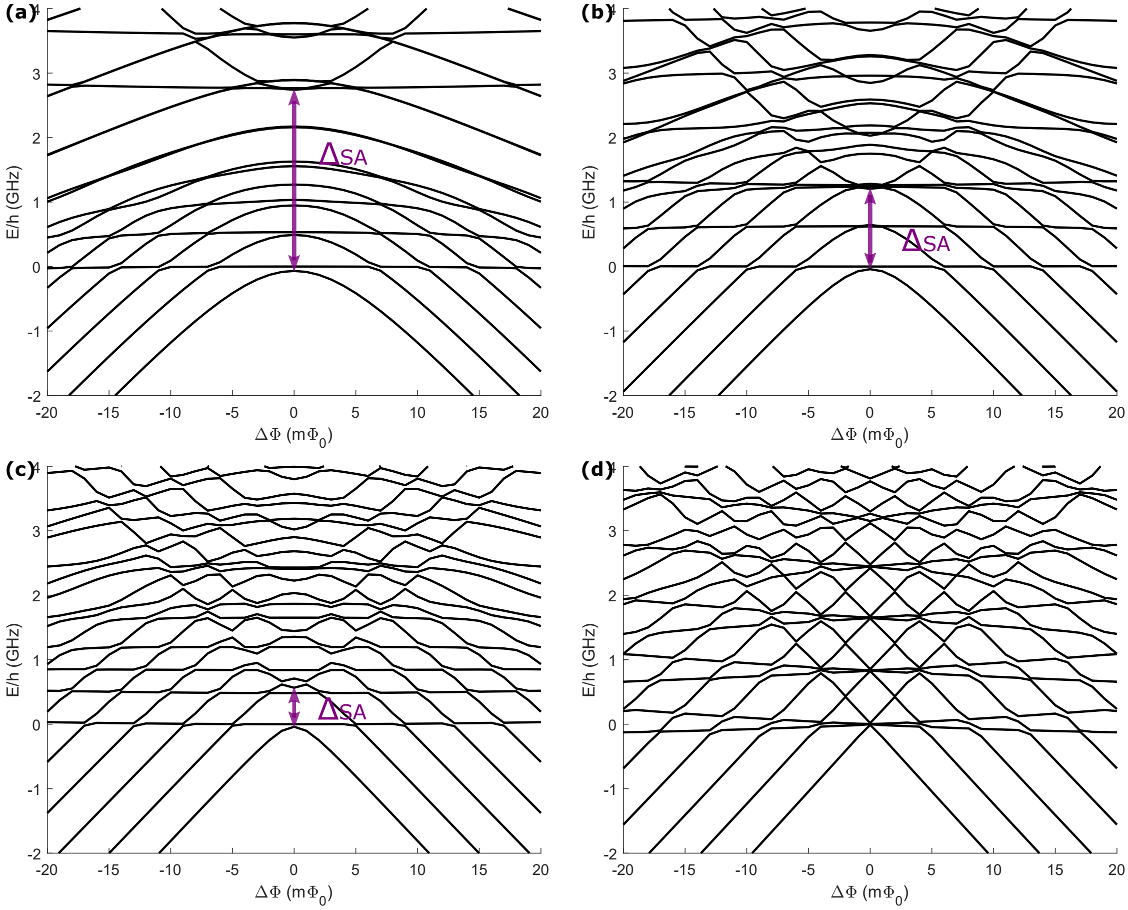

Figure 4.6: Double plaquette flux dispersion with different intermediate island capacitance (a) $C_{isl} = 1$ fF, which results in strong hybridization and $\Delta_{SA} \approx 2.9$ GHz. (b) $C_{isl} = 5$ fF. The hybridization is reduced and $\Delta_{SA} \approx 1.3$ GHz. (c) $C_{isl} = 10$ fF. The hybridization is significantly suppressed. $\Delta_{SA} \approx 0.5$ GHz, and the flux dispersion is close to linear. (d) $C_{isl} = 50$ fF. The hybridization is almost suppressed, the $\Delta_{SA} \approx 0$ GHz, and the flux dispersion is essentially linear.

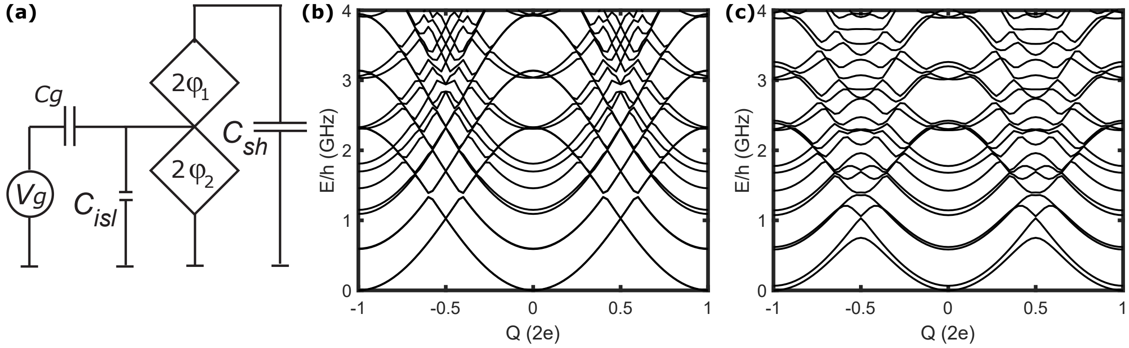

Figure 4.7: (a) Circuit schematic. (b) When $\alpha = 0$, the charge modulation for the symmetric/antisymmetric energy levels for even- and odd-parity (The even- and odd parity levels are on top of each other) have $4e$ dependence. They cross at $1e$ and the gap closes because of destructive interference. (c) When α =0.03, the charge modulation for the symmetric/antisymmetric energy levels for even- and odd-parity have $4e$ dependence. They cross at $1e$ and the gap closes for even-parity states, because of destructive interference; at the same time, the splitting remains open for odd-parity states, because of incomplete destructive interference.

50 fF, the effective mass is so large that all four wells are nearly independent with vanishing coupling between them [Fig. 4.6(d)]; $\Delta_{SA} \approx 0$ GHz and the flux dispersion near double frustration is essentially linear.

4.3.3 Double frustration charge dispersion at double frustration

As described in Sec. 3.3, with effective hybridization at double frustration, the splitting between symmetric and antisymmetric levels also exhibits Aharonov-Casher interference, similar to single frustration, but now based on the offset charge bias Q_{isl} of the intermediate island between the frustrated plaquettes (Fig. 4.7). When $\alpha = 0$, the symmetric/antisymmetric energy levels for both even and odd parity have $4e$ periodicity. When the symmetric and antisymmetric energy levels cross at $1e \mod 2e$, the gap closes [Fig. 4.7(b)], because the even- (odd-) parity wavefunctions both experience a $\cos 2\varphi$ potential [Fig. 4.8(d)]. When $\alpha \approx 0.03$ [Fig. 4.7(c)], Δ_{SA} vanishes at $1e \mod 2e$ for the even-parity energy levels because these wavefunctions still experience a $\cos 2\varphi$ potential, while Δ_{SA} for the odd-parity energy levels doesn't fully close because the potential for these wavefunctions is not exactly $\cos 2\varphi$ [Fig. 4.8(e)]. When

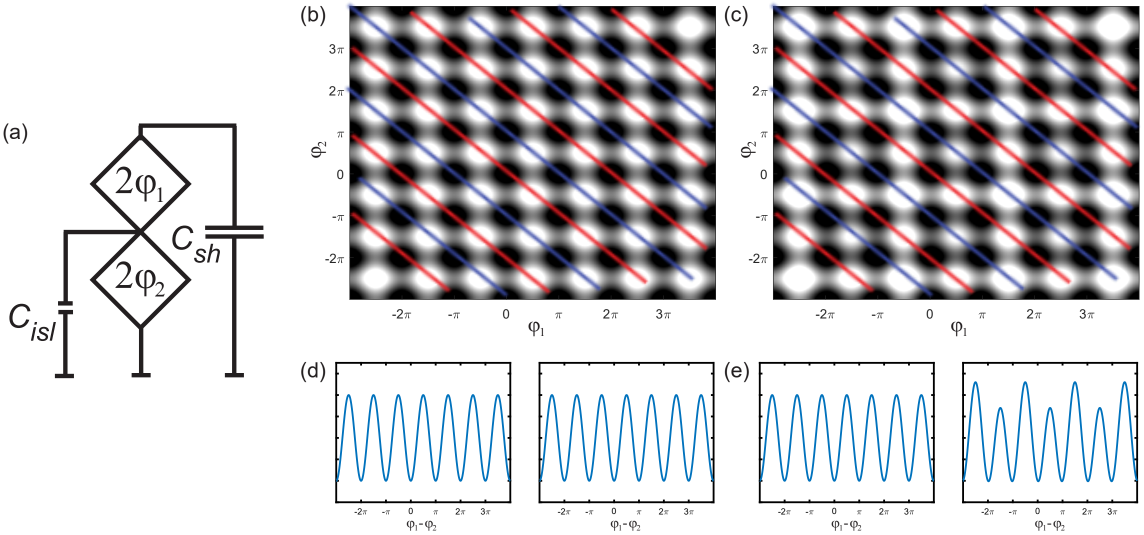

Figure 4.8: Same figure as Fig. 3.10, repeated here for emphasis. (a) Circuit schematic. (b) 2D potential when $\alpha = 0$ with unwrapping the compact phase variables so that they are no longer on a torus, but instead extend to $\pm\infty$. Red lines correspond to hybridization for even-parity wavefunctions, while blue lines correspond to hybridization for odd-parity wavefunctions. (c) 2D potential when α is non-negligible. (d) $\alpha = 0$: Left (right) plot is the 1D cut potential along the direction of hybridization for even- (odd-) parity wavefunctions, and they both have a $\cos 2\varphi$ potential. (e) $\alpha \neq 0$: Left/right plot is the 1D cut of the potential along the direction of hybridization for even- (odd-) parity wavefunctions. The even-parity wavefunctions experience a $\cos 2\varphi$ potential, while the odd-parity wavefunctions experiences a potential with a $\cos \varphi$ component mixed in with the $\cos 2\varphi$ potential.

we bias the the charge at $0e \mod 2e$, the transition between the even- and odd-parity logical states is first-order insensitive to charge noise on the intermediate island. However, there can be discrete charge jumps of order $1e$ [57, 54]. For the charge sensing area of the intermediate island on our device, this happens roughly every 10 minutes, providing enough time for us to detect the charge jump and tune the offset charge to stabilize it at $0e$. When quasiparticles tunnel on and off the intermediate island, this introduces a $1e$ change in Q_{isl} and Δ_{SA} closes. In this case, the system can end up in the antisymmetric excited state, corresponding to a leakage error. Minimizing quasiparticle poisoning on the intermediate islands is important for this system. We can reduce the quasiparticle poisoning rate in our system by doing gap engineering, using a more compact shunt capacitor to avoid absorbing pair-breaking radiation [54], and using backside metallization to downconvert pair-breaking phonons [79, 65].

4.3.4 Double frustration flux dispersion at different Q_{isl}

In Fig. 4.9, we plot the flux dispersion of the energy levels near double frustration for different Q_{isl}. We first look at when the circuit is perfectly symmetric and $\alpha = 0$. For $\alpha = 0$, with $Q_{isl} = 0$, the two paths between the 00 and $\pi\pi$ wells interfere constructively so the strong tunnel coupling results in a large Δ_{SA} [Fig. 4.9(a)]. This strong coupling results in large Δ_{SA}. When $Q_{isl} = 1e$, the two paths have destructive interference. The phase particle cannot tunnel and the coupling between the 00 well and $\pi\pi$ well is suppressed, so $\Delta_{SA} = 0$ [Fig. 4.9(b)]. Next, we consider when the two junctions in the plaquette are not symmetric and $\alpha = 0.03$. When $Q_{isl} = 0e \mod 2e$, the energy of the ground-state doublet is not degenerate at frustration, but degenerate away from frustration [Fig. 4.9(c)]. When $Q_{isl} = 1e \mod 2e$, Δ_{SA} for the even-parity energy levels still closes [Fig. 4.9(c)] because it experiences a $\cos 2\varphi$ potential [Fig. 4.8(e)], while Δ_{SA} for the odd-parity energy levels remains open [Fig. 4.9(c)] because it experiences a potential with a nonzero $\cos\varphi$ component.

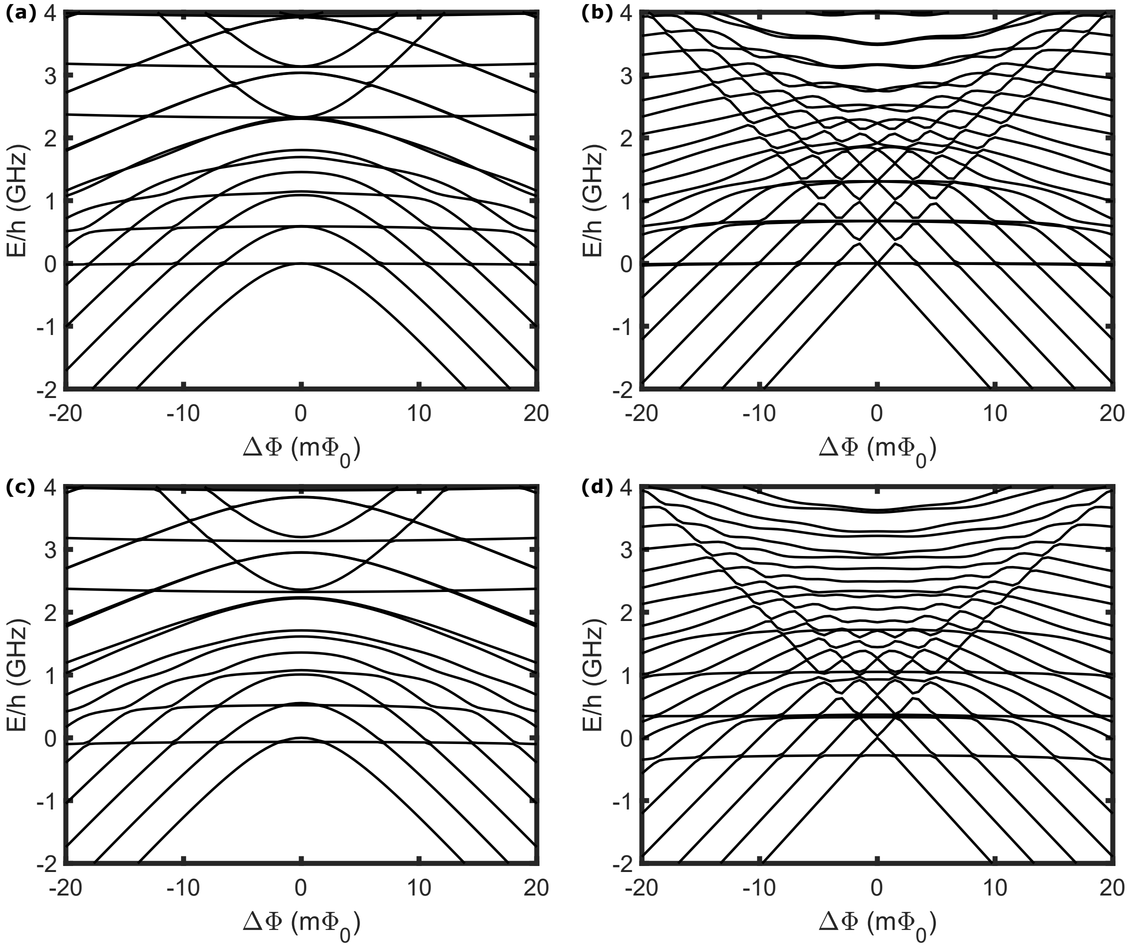

Figure 4.9: Energy levels vs. flux at double frustration with different intermediate island offset charge. (a,b) $\alpha = 0$: The phase particle can tunnel from 00 well to $\pi\pi$ well along two identical paths leading to Aharonov-Casher interference depending on the enclosed charge, in this case, the offset charge on the intermediate island. (a) When $Q_{isl} = 0e \mod 2e$, constructive interference results in significant tunneling between the 00 and $\pi\pi$ wells. (b) When $Q_{isl} = 1e \mod 2e$, the two paths have destructive interference and tunneling is suppressed, thus $\Delta_{SA} = 0$. (c,d) $\alpha = 0.03$: now the even- and odd-parity wavefunctions experience different potentials. (c) When $Q_{isl} = 0e \mod 2e$, the energy of the ground state doublet is not degenerate at frustration, but instead this degeneracy is moved away from frustration. (d) When $Q_{isl} = 1e \mod 2e1e$, the Δ_{SA} for even-parity energy levels still closes because it experiences a $\cos 2\varphi$ potential, while the Δ_{SA} for odd-parity energy levels remains open because it experiences a potential with a nonzero $\cos\varphi$ component.

4.4 Triple frustration modeling

4.4.1 Structureless plaquette model

Modeling a full three-plaquette circuit is computationally expensive. It has 11 nodes [Fig. 4.1(d)], and each node requires several charge states. The matrix size is 189,000×189,000, so it requires ∼300 GB RAM and takes weeks to calculate the energy levels, even with processors with 40 cores. As a more practical alternative, we can use the stuctureless plaquette model to approximate the full-structure plaquette model.

We first connect one arm of the plaquette to form a loop, then vary the flux in this loop to get the potential of this arm. We can extract the Fourier components of this potential. The structureless plaquette model replaces the Josephson potential with the potential we extract from one arm of the plaquette. Because of this, we do not need the linear inductor in the circuit and we reduce the effective nodes from 11 to 5, and the matrix size becomes 7,000×7,000. We add a renormalization factor in the junction capacitance to simulate the effect of higher internal levels. We find the structureless plaquette model has good agreement with the full-structure plaquette near frustration. We use the strucureless plaquette model for the rest of the section.

4.4.2 Triple frustration flux dispersion vs. intermediate island capacitance

We model the triple frustration flux dispersion for a simultaneous scan of the flux bias to each plaquette along a line from 000 to $\pi\pi\pi$ in Fig. 4.10 with C_{isl} = (a) 1 fF, (b) 8 fF, (c) 25 fF, (d) 50 fF. In Fig. 4.10(b), at frustration, the computational states are the superposition of even-parity wells (000,$0\pi\pi$,$\pi0\pi$,$\pi\pi0$) and the superposition of odd-parity wells ($\pi\pi\pi$,00π,$0\pi0$,$\pi00$).

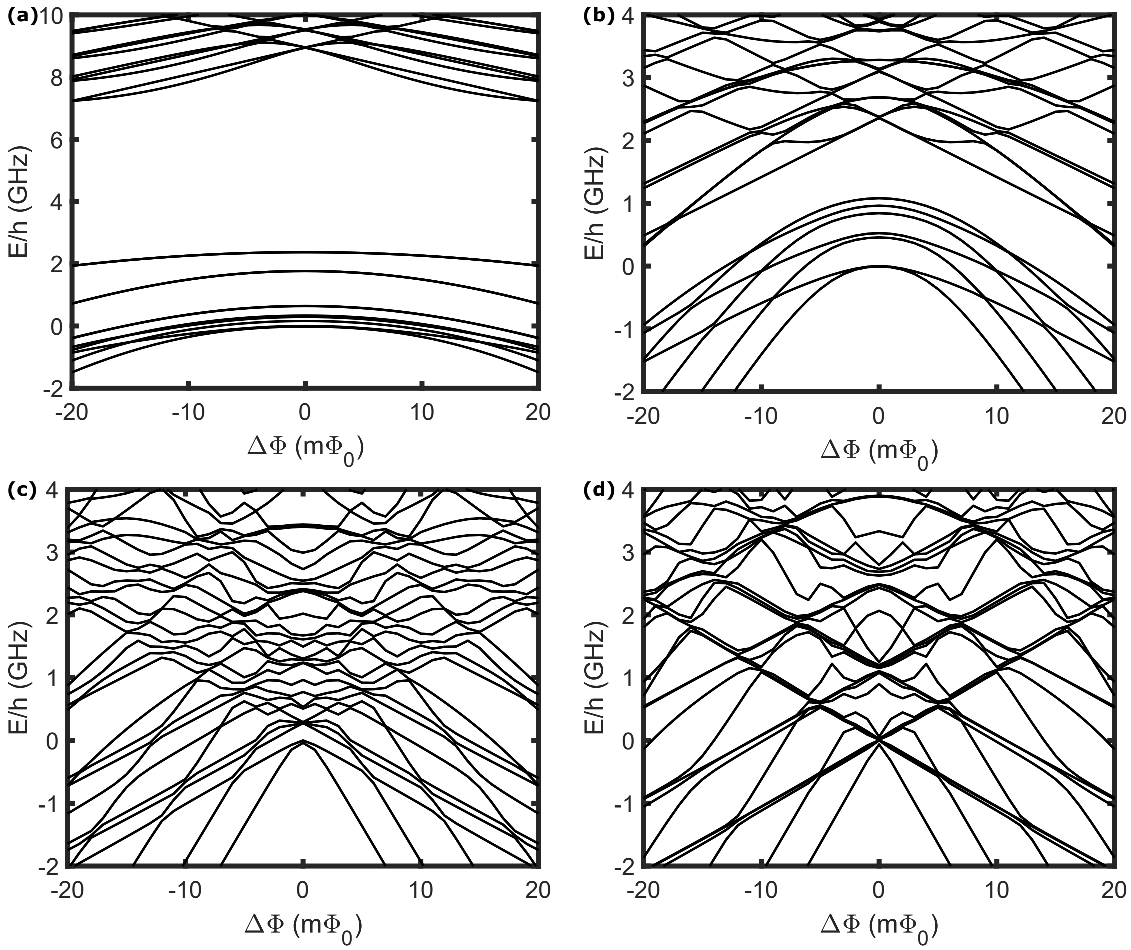

Figure 4.10: Structureless plaquette model. Energy level spectrum with $\alpha = 0$ at triple frustration for simultaneous scan of flux bias to each plaquette along a line from 000 to $\pi\pi\pi$ for C_{isl} = (a) 1 fF, (b) 8 fF, (c) 25 fF, (d) 50 fF.

Chapter 5

Device design and fabrication

In this chapter, I describe the choice of device parameters and device layout. Next, I present our simulations of capacitances between different islands, and inductances between flux bias lines and plaquette loops. Finally, I discuss our fabrication procedure towards the end of the chapter.

5.1 Device parameters

As discussed in Ch. 3, extablishing clear stabilizer behavior at double frustration requires plaquettes with a dominant π-periodic potential and large quantum fluctuations in the direction of constant $\varphi_1+\varphi_2$ in the space of common-mode phases across each plaquette. The π-periodicity comes from a dc SQUID consisting of two conventional Josephson junctions and a non-negligible loop inductance. The Josephson energy of the junction is described in Eq. (2.22). Each junction has a critical current given by Eq. (2.18). We implement inductors in each plaquette with chains of large-area Josephson junctions, similar to typical fluxonium designs [27]. The inductive energy of the junction chain can be extracted with $E_L = (\Phi_0\Delta/4e)/R_n^L$, where R_n^L is the junction chain resistance at room temperature. If the E_J/E_L ratio is too small, E_2 vanishes and we do not have a $\cos 2\varphi$ potential; if E_J/E_L is too large, the energy levels tune too strongly with flux so that even if there are large quantum fluctuations, the device will not have protection against flux noise. To have large quantum fluctuations in the direction of constant $\varphi_1 + \varphi_2$ for effective hybridization between the two plaquettes, we need large E_C and E_C^{isl} compared to the barrier height, which determines the coupling between the $00/\pi\pi$ wells and the $0\pi/\pi 0$ wells. For our device, we are considering energies in K and we target $E_J \sim 1.5\,\mathrm{K}$, $E_L \sim 1.5\,\mathrm{K}$ and $E_C \approx 3.5\,\mathrm{K}$ ($k_B = 1$). For a junction with large E_J and E_C, if the junction plasma frequency $\omega_p = \sqrt{2E_J E_C}/\hbar$ approaches 2Δ for the junction electrodes, the junction acquires an extra capacitance for quasiparticles on either side of the junction. The specific electronic capacitance can be expressed as $C_{elec}^{sp} = 3\hbar e J_C/16\Delta^2$ [80], where J_C is the critical current density of the junction and Δ is the superconducting gap. Our target E_J is ~1.5 K and junction area is $110\,\mathrm{nm} \times 130\,\mathrm{nm}$, and the corresponding $J_C \sim 4\ \mu\mathrm{A}/\mu\mathrm{m}^2$ and $C_{elec} \sim 0.3$ fF. Our estimated specific geometric capacitance is $\sim 50\ \mathrm{fF}/\mu\mathrm{m}^2$, so $C_{geo} \sim 0.7$ fF. The total capacitance of the junction is $C_J = C_{elec} + C_{geo} = 1$ fF, and $E_C \sim 4$ K. Junctions of this size are close to the lower limit where we can maintain reasonably small junction asymmetry with our fabrication. Thus, making smaller junctions to reduce C_{geo} is not practical. The simulated geometric charging energy of each intermediate island to the ground ($E_C^{isl} = (2e)^2/2C_{isl}$) is $\sim 4.6\,\mathrm{K}$ between Plaquette 1 and Plaquette 2, and $\sim 0.74\,\mathrm{K}$ between Plaquette 2 and Plaquette 3. The E_C^{isl} is significantly smaller between Plaquette 2 and Plaquette 3 because chains in Plaquette 2 contribute to the capacitance to ground of the intermediate island. The intermediate island also has capacitance to ground through the junction capacitors [Fig. 4.1], thus E_C of each each of the four junctions in the two plaquettes reduces the total charging energy of the intermediate island.

To estimate E_2 for this device, we model a circuit that embeds a plaquette in an rf SQUID, vary the flux across the rf SQUID loop, calculate the energy levels, and obtain the Fourier components for the lowest energy level. The E_2 value then corresponds to the Fourier component for the $\cos 2\varphi$ term. The extracted E_2 for this circuit is ~ 0.05 K. For effective concatenation, both E_C and E_C^{isl} need to be large compared to E_2. For this target value of E_2, we require a rather large shunt capacitor with C_{sh}=1200 fF in order to suppress single Cooper pair tunneling on/off the logical island. The charging energy for this shunt capacitor is $E_C^{sh} = 0.003$ K, and $E_C^{sh}/E_2 = 0.06$, so the coupling between the even- and odd-parity states will be suppressed.

When there are small asymmetries in the circuit, particularly between the E_J values of the two junctions in a plaquette, the even- or odd-parity states experience slightly different potentials and the states are not exactly degenerate at frustration (Fig. 4.8). This results in an increase in the coupling between the even- and odd-parity states and an increase in the gap between the computational states. The α in our circuit is $\sim$ 0.02 - 0.04, and the splitting between the even- and odd-parity is on the order of $\sim$100 kHz at single frustration.

5.2 Device design

In order to allow for local flux-biasing of the different plaquettes and charge-biasing of the various superconducting islands, our device incorporates a series of on-chip bias lines, indicated in Fig. 5.1. The heart of the device contains a chain of three plaquettes, each with two small Josephson junctions and two junction-chain inductors (17 junctions in series with size 140 nm × 1070 nm) (Fig. 5.3). As discussed in Sec. 5.1, minimizing C_{isl} for each intermediate island between two adjacent plaquettes is critical for successful concatenation. Thus, ideally the four Josephson junctions in two adjacent plaquettes will all be located near the island between the plaquettes so that the junction electrode that is closest to the island will be as short as possible and contribute a minimal amount of excess capacitance to ground. However, in a chain of three plaquettes, this is only possible for one of the two intermediate islands. The other island will necessarily have to be connected to the two inductors for one of the plaquettes, and the capacitance to ground for these inductors will enhance the effective island capacitance (Fig. 4.1). In addition, the 3-plaquette chain has dummy plaquettes at either end, which have the same geometry as the other plaquettes, but the small junctions and inductor-chain junctions are intentionally shorted out. The dummy plaquettes are included to symmetrize the geometry and minimize the inductive coupling of the on-chip flux-bias lines to the LC mode of oscillation of the plaquette chain, sometimes referred to as the M' coupling, as defined in Ref. [25].

There are four on-chip flux-bias lines for controlling the flux bias to each of the three plaquettes. Each flux-bias line has a coplanar geometry that splits into a T-shaped path adjacent to the plaquette chain, with the two ends of the T connected directly to the ground plane. In order to have a well-defined path for the return currents and to suppress slot-line modes between different portions of the ground plane, we fabricated superconducting ground straps across each flux-bias line in multiple

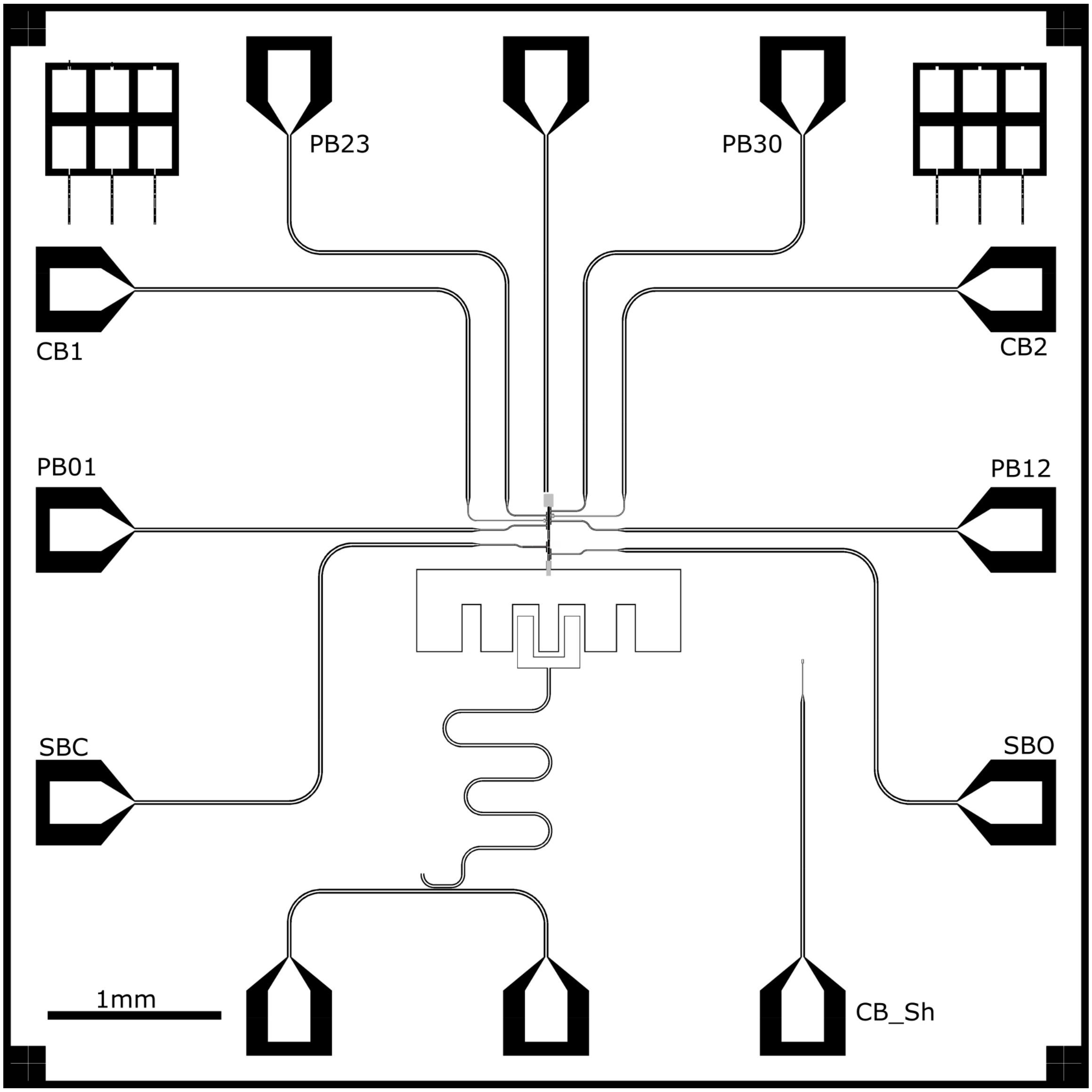

Figure 5.1: Device schematic. Plaquettes are in the middle of the figure and connect to the large shunt capacitor. We apply fluxes to different plaquettes through PB01, PB12, PB23, PB30 flux bias lines. We apply fluxes to the two SQUIDs that comprise the SQUID switch through SBC and SBO. We control the offset charges on the shunt capacitor through CB$_{sh}$ and the offset charge on the intermediate island through CB1 and CB2 charge bias lines.

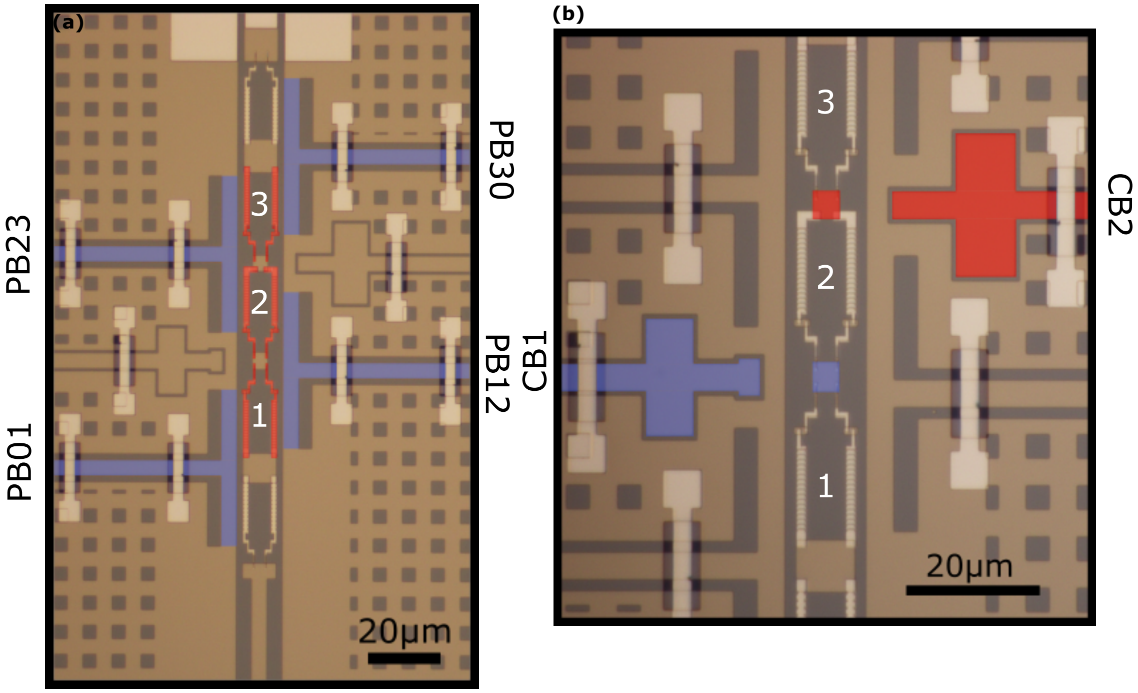

Figure 5.2: Image from optical microscope with (a) colorized flux lines (blue) and plaquette loops (red), (b) colorized charge lines and intermediate islands.

locations. In addition to the flux-bias lines, we also have three charge-bias lines for tuning the offset charge to the shunt capacitor electrode and each of the two intermediate islands between pairs of plaquettes. These charge-bias lines are isolated from ground, but also include similar ground straps to what is used on the flux-bias lines.

Our design also includes a pair of series dc SQUIDs between the plaquette chain and C_{sh} that could be used for gate operations in a future implementation of a protected qubit based on concatenated π-periodic plaquettes, which we will discuss in Ch. 8. For the experiments presented here, these SQUIDs, which have their own separate flux-bias lines from the plaquettes, were not used in the present measurements and were maintained at a flux bias of $0 \bmod \Phi_0$ throughout the experiment. At this bias point, the SQUIDs behave primarily as superconducting shorts, although we must still account for the nonlinearity of the SQUID junctions in modeling the energy levels for our device.

The target shunt capacitance, $C_{sh} \sim 1200\,\mathrm{fF}$ for our present device is rather large compared to more conventional superconducting qubits. Nonetheless, in the present

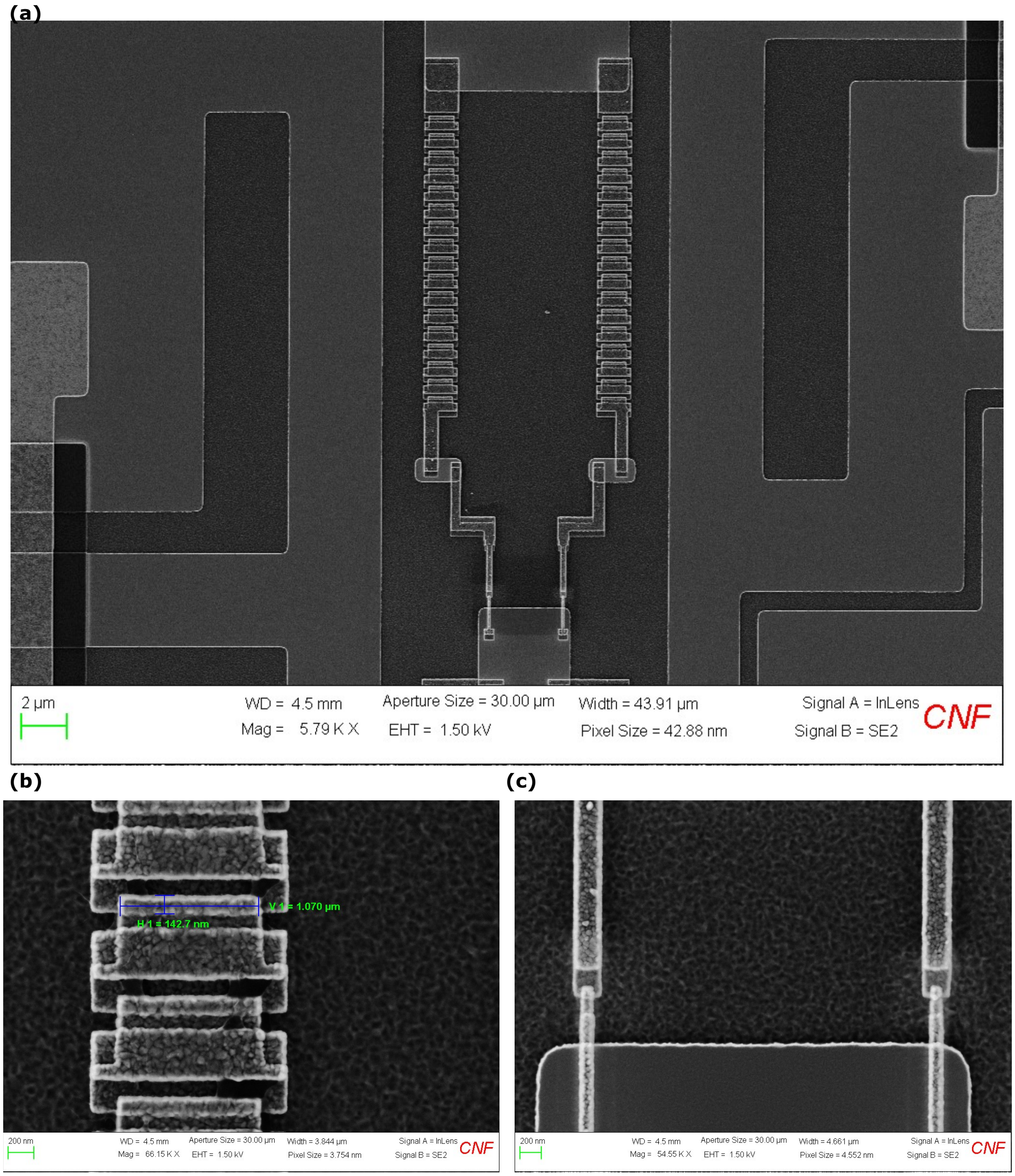
(a)
2 µm
WD = 4.5 mm
Mag = 5.79 K X
Aperture Size = 30.00 µm
EHT = 1.50 kV
Width = 43.91 µm
Pixel Size = 42.88 nm
Signal A = InLens
Signal B = SE2
CNF
(b)
V 1 = 1.070 µm
H 1 = 142.7 nm
200 nm
WD = 4.5 mm
Mag = 66.15 K X
Aperture Size = 30.00 µm
EHT = 1.50 kV
Width = 3.844 µm
Pixel Size = 3.754 nm
Signal A = InLens
Signal B = SE2
CNF
(c)
200 nm
WD = 4.5 mm
Mag = 54.55 K X
Aperture Size = 30.00 µm
EHT = 1.50 kV
Width = 4.661 µm
Pixel Size = 4.552 nm
Signal A = InLens
Signal B = SE2
CNF

Figure 5.3: SEM images of (a) plaquette, (b) junction chain, (c) small junctions.

experiment, we implemented C_{sh} with a planar superconducting Nb electrode with a small gap to the ground plane around the perimeter. Although this is the standard technique for making shunt capacitors for transmons, whose shunt capacitors are much smaller (∼50-80 fF), the large shunt capacitor has consequences for the device performance that will be discussed later. For example, it results in low-frequency spurious antenna modes, a large charge-sensing area for offset charge jumps, and enhanced quasiparticle poisoning.

For measuring our device, we have a coplanar waveguide (CPW) readout resonator with a fundamental resonance at 4.7 GHz. This is a 1/4-wave resonator with one end inductively coupled to a CPW feedline that is connected to our measurement circuitry; the other end of the resonator has a coupling capacitance $C_c = 36\,\mathrm{fF}$ to our device.

5.3 Simulation

For designing these complex devices, we must rely on numerical simulations of the circuit parameter values for different layouts. In this section, I first discuss the simulation of capacitances of the various islands and bias lines. Next, I describe our simulations of inductances between plaquette loops and flux-bias lines.

5.3.1 Capacitance simulation

The capacitances are simulated using a finite-element analysis software (ANSYS Q3D package) (Fig. 5.4). In Table 5.1, we show the capacitance between the islands and the charge bias lines. The CB1 and CB2 lines are close to the shunt capacitor and have a large capacitance to the shunt capacitor island. The intermediate island between Plaquette 1 and Plaquette 2 (Island 1) is small, so the offset charge on Island 1 is primarily tuned with CB1, although with a small crosstalk tuning from CB2. The island between Plaquette 2 and Plaquette 3 (Island 2) has the contribution from the junction-chain inductors in Plaquette 2, thus it has a signficantly larger capacitance to ground compared to Island 1. This, combined with the proximity to CB1, leads to a significant crosstalk capacitance between CB1 and Island 2.

In Table 5.1, we list different islands capacitances to ground. To estimate the ground capacitance of Island 1 (C_{isl1}), we need to include the junction electrode that directly connects to the intermediate island for simulation. C_{isl_2} for Island 2 is more

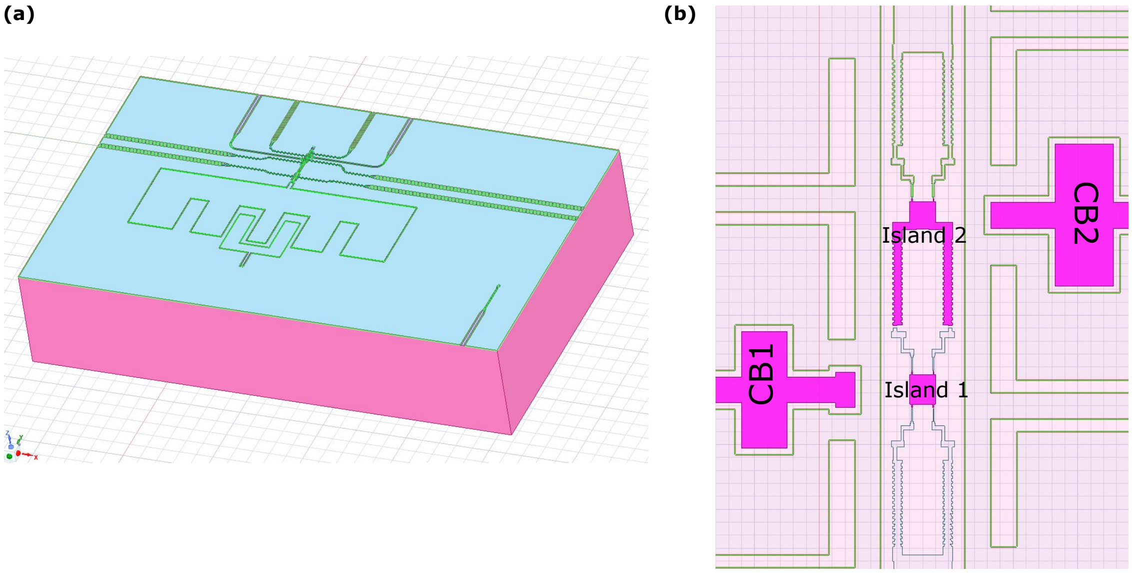

Figure 5.4: (a) Q3D simulation image. (b) Zoomed in Q3D image and the highlighted magenta color elements are CB1, CB2, Island 1 and Island 2. Island 2 is simulated including part of the junction chain inductor.

Simulated capacitance matrix (aF)			
	CB_{sh}	CB1	CB2
$Island_{sh}$	54	420	350
Island 1	0	36	8.0
Island 2	0	78	120

Table 5.1: Capacitances between the various charge bias lines (CB) and different islands.

Simulated ground capacitances (fF)		
$\text{Island}_{\text{sh}}$	Island 1	Island 2
1000	0.81	5.0

Table 5.2: Simulated island capacitance to ground

Simulated Inductance Matrix (pH)				
	PB01	PB12	PB23	PB30
Plaq1	0.594	0.775	-0.174	0.106
Plaq2	0.146	-0.688	-0.547	0.237
Plaq3	0.066	-0.201	0.599	0.756

Table 5.3: Simulated mutual inductances between flux-bias lines and plaquette loops.

complicated, because the junction chain acts like a superconducting short, and it partly contributes to C_{isl2}.

5.3.2 Inductance simulation

We import the device layout in InductEx [81], assign materials and film thicknesses to the different circuit elements, and assign ports for current flow in and out. InductEx can then simulate the mutual inductance between different circuit elements [82, 83]. The simulated inductances are given in Table 5.3. We target primary mutual inductances to each plaquette of roughly 1 pH to allow for biasing with fluxes of order 1 Φ_0 with sufficiently small currents to minimize heating in cryogenic cables; at the same time, these mutual inductances are small enough to minimize dissipation coupled inductively to the plaquettes through the bias-line circuitry.

5.4 Fabrication

The three-plaquette device presented in the subsequent chapters is fabricated on a high resistivity ($\geq$10 kΩ-cm) silicon wafer that was given a standard RCA clean, which is a standard set of wafer cleaning steps, followed by an etch step in a buffered-2% per volume HF bath to remove native oxides immediately before loading into the vacuum chamber for the base-layer metal deposition. The base layer of 60-nm thick niobium is sputter-deposited and is then coated with DSK101-4 anti-reflective-coating (ARC) and DUV210-0.6 photoresist before performing deep-UV photolithography on a photostepper to define the ground plane, feedline, resonator, flux/charge bias lines, and the logical islands. The exposed wafer is then baked at 135°C for 90 seconds, developed with AZ 726 MIF, briefly cleaned with an ARC etch to remove any remaining unwanted ARC, and then dry etched using BCl_3, Cl_2, and Ar in an inductively coupled plasma etcher. The wafer is then subject to another buffered HF dip to remove any further oxides that may have formed on the surface of the remaining niobium.

The next set of lithography steps creates ground straps that connect ground planes on either side of the flux, charge, and feedlines. The first step uses lift-off resist LOR3A and then DUV210-0.6 photoresist to expose a region underneath the intended ground straps where we deposit SiO_2 to function as an insulating dielectric support for the aluminum ground straps to follow. The SiO_2 is evaporated in an electron beam evaporator at a rate 3.5 Å/s until 100 nm is deposited. The wafer is then placed in 1165 Remover (N-Methly-2-pyrrolidone (NMP)) at 65°C to lift off the excess SiO_2 and resist and then another clean bath of 1165 Remover (NMP) at 65°C for further liftoff. The wafer is then sonicated for 10 seconds to remove any final remaining resist and SiO_2. The second layer of the ground strap process is exposed in the same way, using LOR3A and DUV photoresist, but this time the pattern lays over the existing SiO_2 and extends further so that once developed, there is an exposed region of the niobium ground plane for the aluminum to contact. The wafer is baked again and developed, and the ground straps are then deposited by electron beam evaporation of aluminum (100 nm thick). The wafer is once again subject to NMP to remove the remaining resist and excess aluminum.

Once clean, the wafer is put through a light oxygen plasma resist strip (Glen 1000) before a bilayer resist stack of MMA/PMMA is spun for electron beam lithography to define the Josephson junctions. The Al-AlO_x-Al junctions are written at 100 keV for a standard double-angle evaporation process. Following a brief ion mill, the first electrode is deposited by electron beam evaporation. The bottom (top) electrode is 40 (80) nm thick. Once the junctions are deposited, the wafer is covered in S1813 photoresist and then diced to $(6.25\text{ mm})^2$ chips. After the dicing, the aluminum metallization is lifted off. The inductors in this plaquette are formed from narrow granular-Al wires. The large kinetic inductance from the thin, narrow disordered

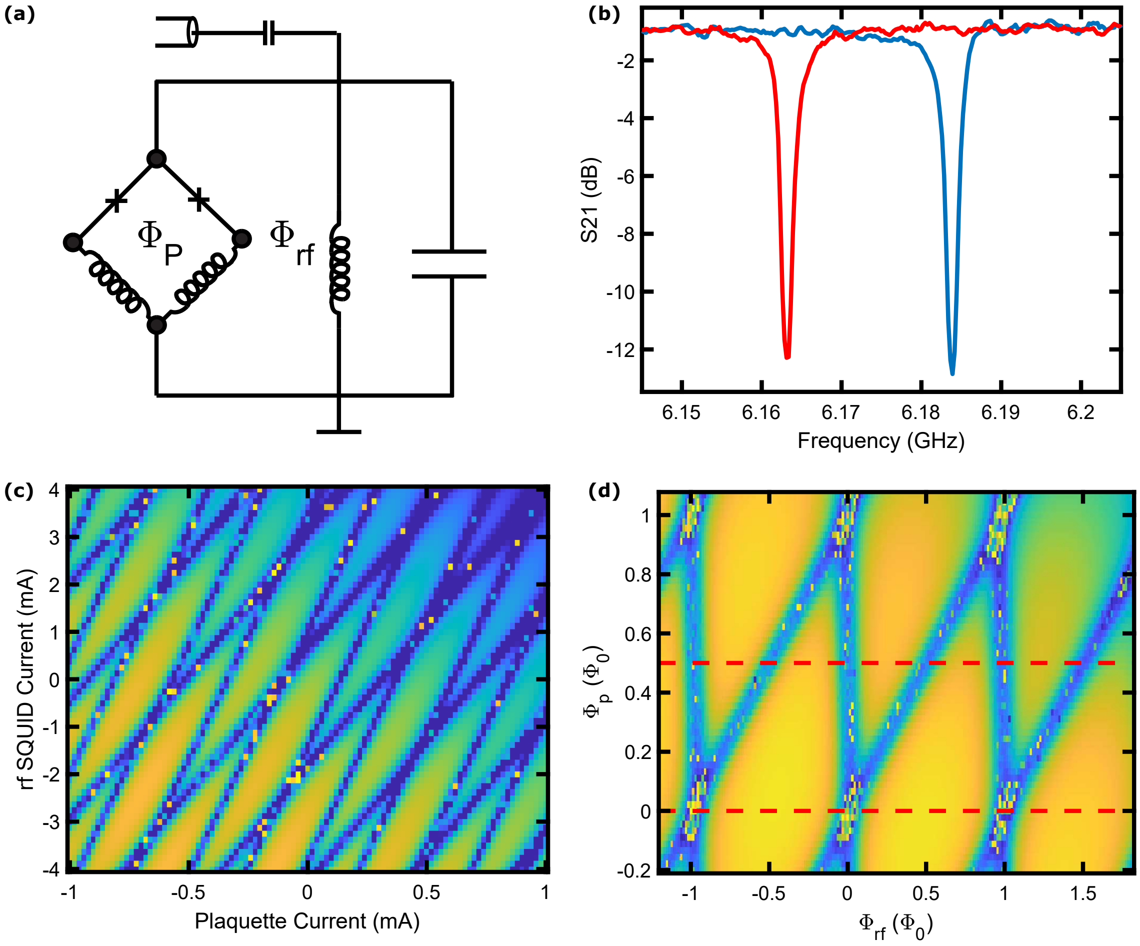

Figure 5.5: (a) Circuit schematic for a plaquette embedded in an rf SQUID loop with a shunt capacitor. (b) Resonance frequency at two different fluxes. (c) Resonance frequency vs. plaquette and rf SQUID flux-bias currents. (d) Resonance frequency vs. orthogonalized rf SQUID flux (Φ_{rf}) and plaquette flux (Φ_P). The yellow color in the two-dimensional plots corresponds to higher resonance frequency and the blue color corresponds to lower resonance frequency. The horizontal red dashed lines correspond to the locations of the cuts for the next figure.

superconducting traces allows us to achieve our target E_L. However, the granular-Al process is challenging to maintain good reproducibility, thus, for our subsequent plaquette-chain circuits, we use junction-chain inductors, as described previously.

5.5 Characterization of π-periodic Josephson element

To characterize and verify the π-periodic Josephson element, we design and fabricate a plaquette with E_J ~4 K, E_L ~3 K, E_C ~2 K, which can be tuned in and out of frustration with the flux Φ_P passing through the plaquette loop. The plaquette is embeded in an rf SQUID so that we can vary the phase across the plaquette by tuning the flux Φ_{rf} passing through the rf SQUID loop [Fig. 5.5(a)]. The rf SQUID is shunted by a capacitor to form a resonant circuit whose frequency can be tuned with Φ_{rf} or Φ_P due to the change of inductances.

We measure the resonance of this circuit in an Adiabatic Demagnetization Refrigerator (ADR) with a base temperature ~50 mK. Figure 5.5(b) shows an example of the change of resonance frequency at different flux. Figure 5.5(c) shows the resonance frequency modulating with the current through the plaquette flux bias line and the rf SQUID flux bias line. The yellow color in the two-dimensional plots corresponds to a higher resonance frequency and the blue color corresponds to a lower resonance frequency. After extracting the inductance matrix, we apply a pure rf SQUID flux in the rf SQUID loop and a pure plaquette flux in the plaquette loop [Fig. 5.5(d)]. When $\Phi_P = 0$, the resonance frequency has a Φ_0 periodicity with respect to Φ_{rf}; when Φ_P =0.5 Φ_0, the resonance frequency has a 0.5 Φ_0 periodicity with respect to Φ_{rf}, which which corresponds to the plaquette having a π-periodicity.

Figure 5.6 shows microwave transmission through the feedline vs. frequency and rf SQUID flux when $\Phi_P = 0$ and $\Phi_P = 0.5\ \Phi_0$, which also also exhibits the two regimes of 2π-periodicity and π-periodicity. Figure 5.7(a) shows the extracted resonance frequency vs. rf SQUID flux when $\Phi_P = 0.5\ \Phi_0$. When we zoom in near the higher resonance frequency, we observe a slightly imperfect π-periodicity [Fig. 5.7(b)], which could be caused either by an asymmetry in the two junctions or a deviation of Φ_P from exact frustration. From the measured variation, we estimate $E_1/E_2 \approx 0.02$, which corresponds to having a π-periodic device with a residual 2π-periodic component at the 2% level.

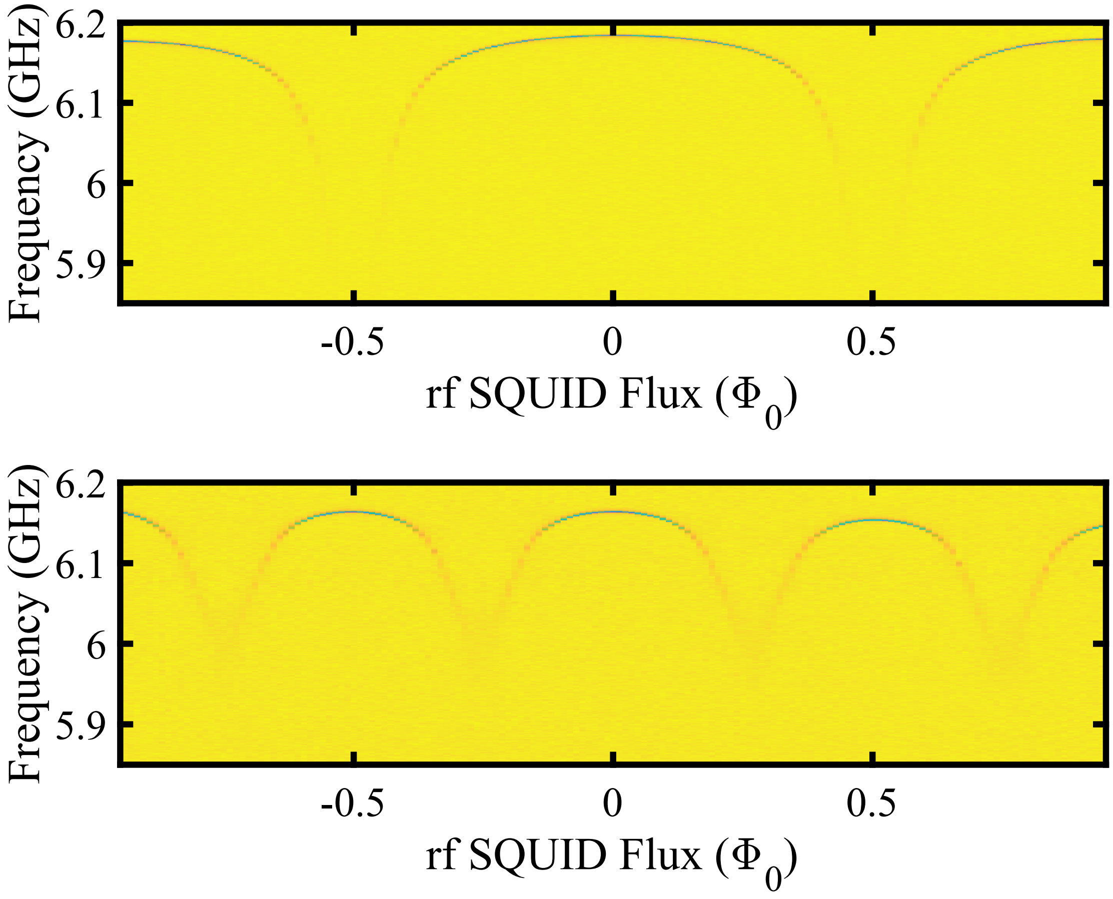

Figure 5.6: (a) Resonance frequency with respect to rf SQUID flux when $\Phi_P = 0$. (b) Resonance frequency with respect to rf SQUID flux when $\Phi_P = 0.5\ \Phi_0$.

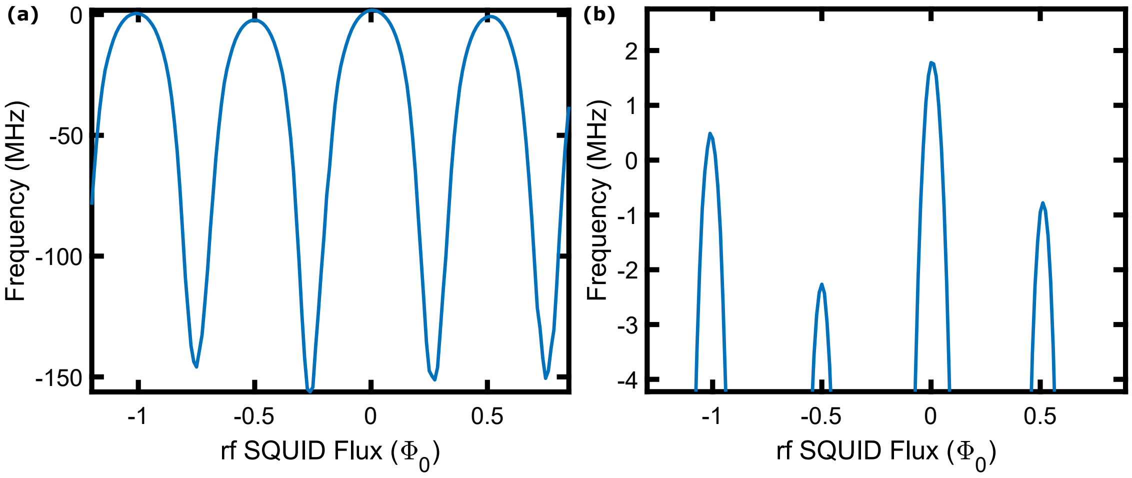

Figure 5.7: (a) Extracted resonance frequency vs. rf SQUID flux when $\Phi_P = 0$. (b) Zoomed-in plot near the upper frequency range.

Chapter 6

Measurement of 3-plaquette chip

In this chapter, I describe the measurement setup, cavity flux tuning, and spectroscopy measurements at single, double, and triple frustration.

6.1 Fridge setup

Our chip is packaged in an Al sample box, with the on-chip control lines connected to the coaxial cables in the fridge through wirebonds and PCB traces. We cover the sample box with an Al lid to prevent light leaks inside the box, and then place the box on the cold-finger in the BlueFors dilution refrigerator.

In Fig. 6.1, we show a schematic of the BlueFors fridge indicating the various stages at different temperatures: 300 K, 50 K still, heat exchanger, and mixing chamber, with temperatures in descending order. The sample is mounted on the mixing chamber stage, which runs at a temperature around 15 mK. At each stage, there is metal shielding to block the blackbody radiation from higher temperature stages. There is a mu-metal can inside the vacuum jacket of the fridge and a Cryoperm shield around the cold-finger where the device is mounted for a two-stage configuration for shielding against external magnetic fields.

We connect the room-temperature electronics and the coaxial cables from room-temperature down to the mixing chamber (Fig. 6.1). Because photons from blackbody radiation can leak from higher temperature stages to the plaquette chip through the coaxial cables, we include cryogenic attenuators to absorb these photons. The attenuators are essentially resistive dividers, so they heat up when they absorb microwave

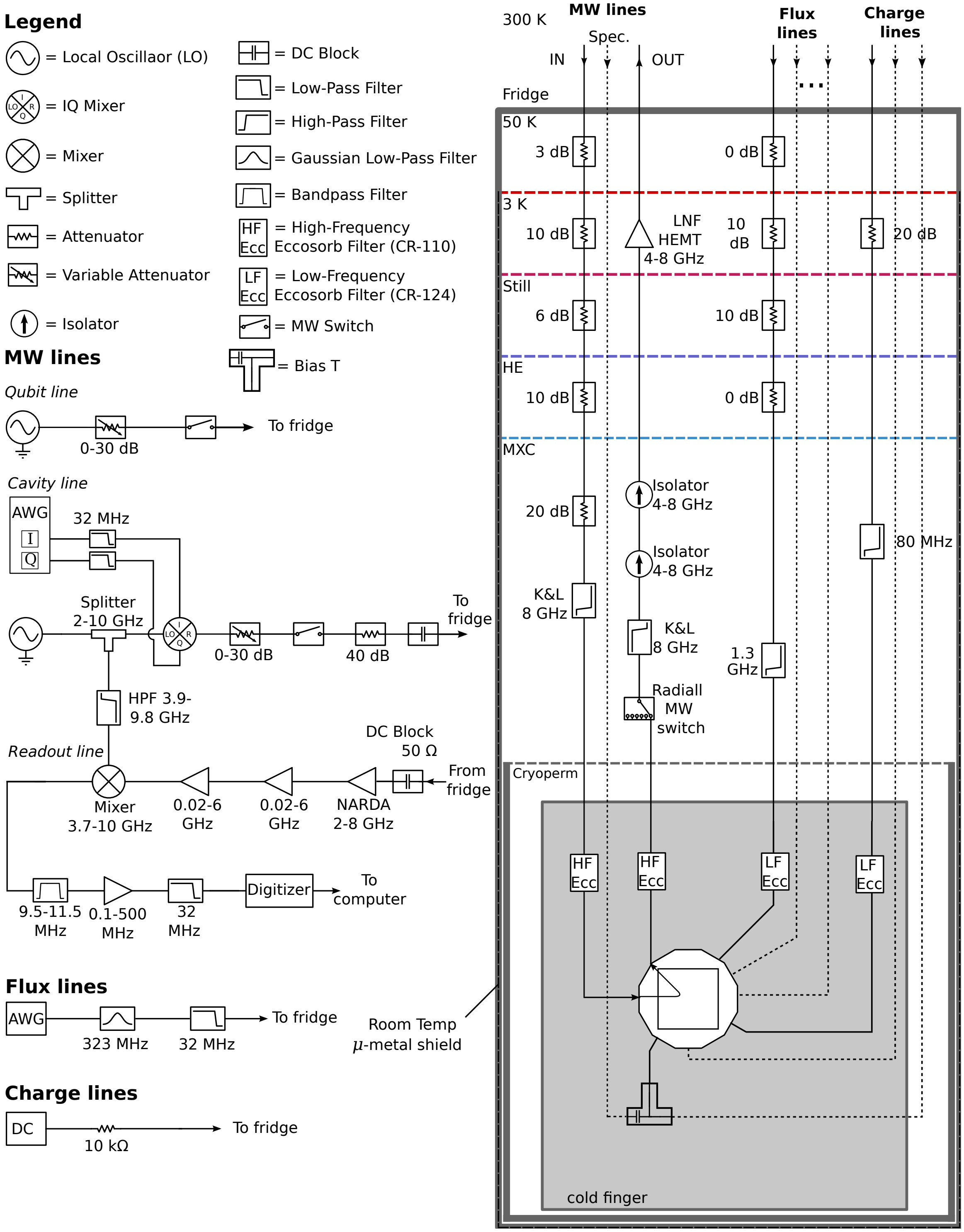
Legend
= Local Oscillaor (LO)
LO R I Q
= IQ Mixer
= Mixer
= Splitter
= Attenuator
= Variable Attenuator
= Isolator
= DC Block
= Low-Pass Filter
= High-Pass Filter
= Gaussian Low-Pass Filter
= Bandpass Filter
HF Ecc = High-Frequency Eccosorb Filter (CR-110)
LF Ecc = Low-Frequency Eccosorb Filter (CR-124)
= MW Switch
= Bias T
MW lines
Qubit line
0-30 dB
To fridge
Cavity line
AWG
I
Q
32 MHz
Splitter 2-10 GHz
0-30 dB
40 dB
To fridge
HPF 3.9-9.8 GHz
Readout line
DC Block 50 Ω
From fridge
Mixer 3.7-10 GHz
0.02-6 GHz
0.02-6 GHz
NARDA 2-8 GHz
9.5-11.5 MHz
0.1-500 MHz
32 MHz
Digitizer
To computer
Flux lines
AWG
323 MHz
32 MHz
To fridge
Charge lines
DC
10 kΩ
To fridge
Room Temp μ-metal shield
300 K
MW lines
Spec.
IN
OUT
Flux lines
Charge lines
...
Fridge
50 K
3 dB
0 dB
3 K
10 dB
LNF HEMT 4-8 GHz
10 dB
20 dB
Still
6 dB
10 dB
HE
10 dB
0 dB
MXC
20 dB
Isolator 4-8 GHz
Isolator 4-8 GHz
80 MHz
K&L 8 GHz
K&L 8 GHz
1.3 GHz
Radiall MW switch
Cryoperm
HF Ecc
HF Ecc
LF Ecc
LF Ecc
cold finger

Figure 6.1: Fridge setup and and room-temperature electronics setup.

signals. At the same time, an attenuator will emit photons with a noise power that depends on the physical temperature of the attenuator. Because the mixing chamber does not have enough cooling power to take away all the heat generated from the attenuators, instead of installing all the attenuators on the mixing chamber, we distribute them to different stages. For the microwave input line, there are also low-pass K&L filters and high frequency eccorsorb filters to block the unwanted photons.

Because the attenuators also suppress the signal we send in the microwave input line, we need to amplify the signal before readout. We do not put any attenuators in the output microwave line because this will further reduce the signal and degrade the signal-to-noise ratio. Instead, we use two-stage isolators and 8-GHz low-pass K&L filters to block the unwanted photons from higher temperature stages and the HEMT amplifier.

Because our waveform generators for supplying the flux-bias signals only have a +/- 1 V range, we only place 20 dB attenuators in the flux lines so that we can tune the flux by more than 2 Φ_0 in each of the loops. The flux-bias lines also have low-pass filters and eccorsorb filters on the mixing chamber to filter high-frequency noise. Each charge-bias line has a 20-dB attenuator at 3 K, along with a 10-kΩ series resistor at room-temperature for dividing the voltage delivered to the on-chip charge-bias line by a factor of 1000. The resistor to ground for the voltage divider is on the 3 K stage to reduce the Johnson–Nyquist noise. The charge-bias lines also have an 80 MHz Mini-Circuits low-pass filter and eccosorb filter on the mixing chamber to filter high-frequency noise.

6.2 Electronics setup

In Fig. 6.1, we show the electronics setup. We use a microwave source to generate the local oscillator for the cavity readout signal. The signal is then mixed with a 13 MHz waveform output from BBN APSII arbitrary waveform generator (AWG). It can output ±1 V with 14 bits of vertical resolution, and has a 1.2 GS/s sampling rate. The signal goes through a digital attenuator, microwave switch, and fixed attenuator before it goes into the fridge. The signal output from the fridge goes through a DC block, room-temperature amplifier (2-8 GHz Narda), two-stage Mini Circuits amplifer, then it is mixed with the local oscillator (LO) signal to downconvert the signal to 13 MHz. This downconverted signal then goes through two low-pass filters and an rf amplifier before it is digitized by our Alazar data acquisition card.

The flux control signals are generated by our BBN APSII, then go through a 323 MHz gaussian filter and a 32 MHz Mini-Circuits low-pass filter to filter out the high frequency noise on the signal lines.

The voltage signals for controlling the offset charges are provided by SRS SIM928 voltage sources. We have an Anritsu K250 bias-T for the shunt capacitor charge bias line on the mixing chamber. This is to allow sending the microwave signal to the shunt capacitor to drive transitions between the energy levels in the plaquette while also allowing the addition of a dc signal for scanning the offset charge bias to the shunt capacitor island.

6.3 Cavity flux tuning

The 3-plaquette device has three plaquette loops and two loops for the SQUID switch elements. Because the flux bias lines have non-negligible mutual inductances to the different loops, we have six on-chip flux bias lines so that we can control a pure flux to each of the loops, while keeping the fluxes in the other loops constant.

We first measure the readout cavity vs. voltage on the PB12 flux line [Fig. 6.2(b)]. The PB12 flux line mainly couples to the Plaquette 1 and Plaquette 2 loops. When either of the plaquettes is near frustration, the plaquette's frequency decreases due to increased inductance, thus causing the cavity to shift to lower frequency. However, from this measurement alone, it is impossible to identify which dips correspond to which plaquette being near frustration.

In order to differentiate the plaquettes at frustration, we scan two different flux lines while fixing the cavity excitation signal at the frequency of one plaquette being at frustration [Fig. 6.2(c,d)]. When the plaquettes are away from frustration, we are driving the cavity away from its resonant frequency, and get a higher transmission, which corresponds to yellow shades. When any of the plaquettes are near frustration, we are driving the cavity near its resonance frequency and get a lower transmission, which corresponds to blue shades. Thus, each of the three sets of parallel blue lines corresponds to one of the three plaquettes being at frustration. The crossing of two lines corresponds to double frustration, and the crossing of three lines corresponds to

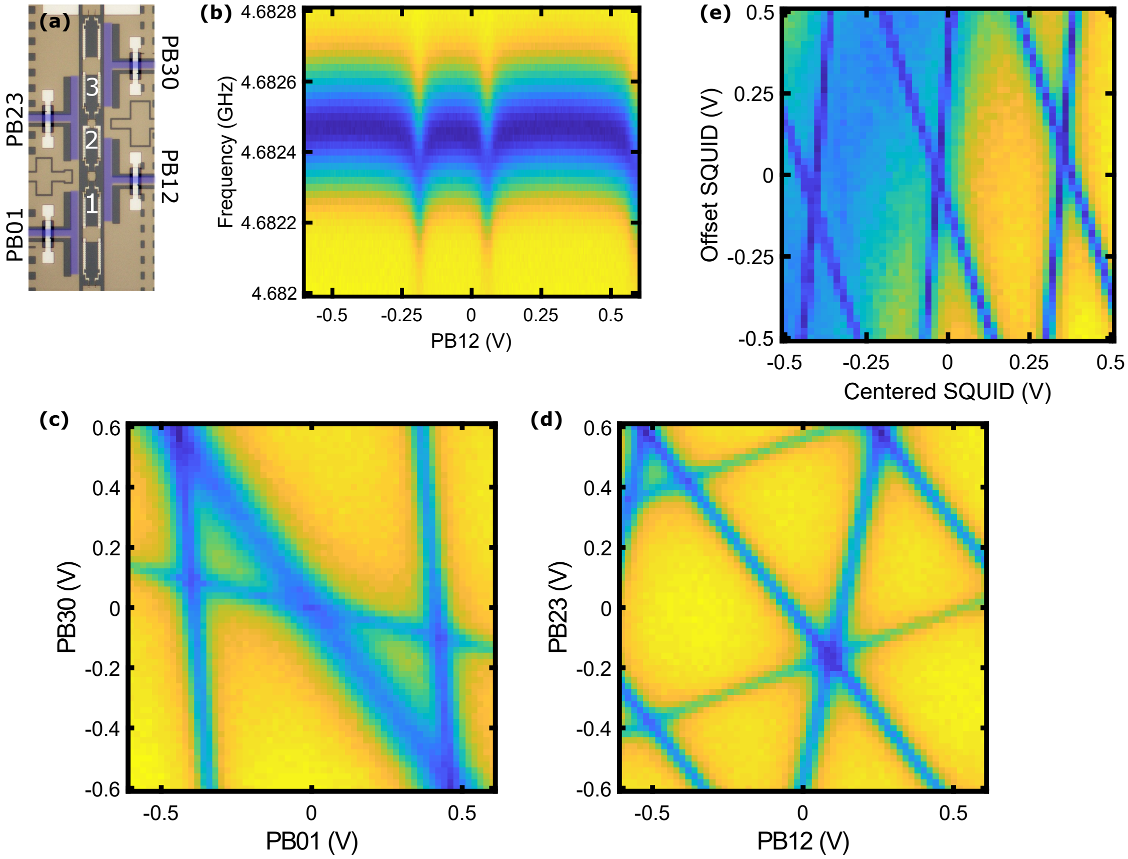

Figure 6.2: (a) Device image and blue false-color highlighting of the different plaquette flux-bias lines. (b) Readout cavity frequency vs. PB12 flux bias line. (c,d) Scanning different combinations of the plaquette flux lines, while fixing the cavity at the frequency of the resonance when one plaquette is at frustration. The three sets of parallel lines correspond to three plaquettes near frustration. (c) Scanning PB01 and PB30 flux bias lines. (d) Scanning PB12 and PB23 flux bias lines. (e) Scanning cavity transmission vs. the two SQUID flux lines, while fixing the cavity at the frequency of the resonance when one of the SQUIDs is at frustration. The two sets of parallel lines correspond to the two SQUIDs tuning through frustration.

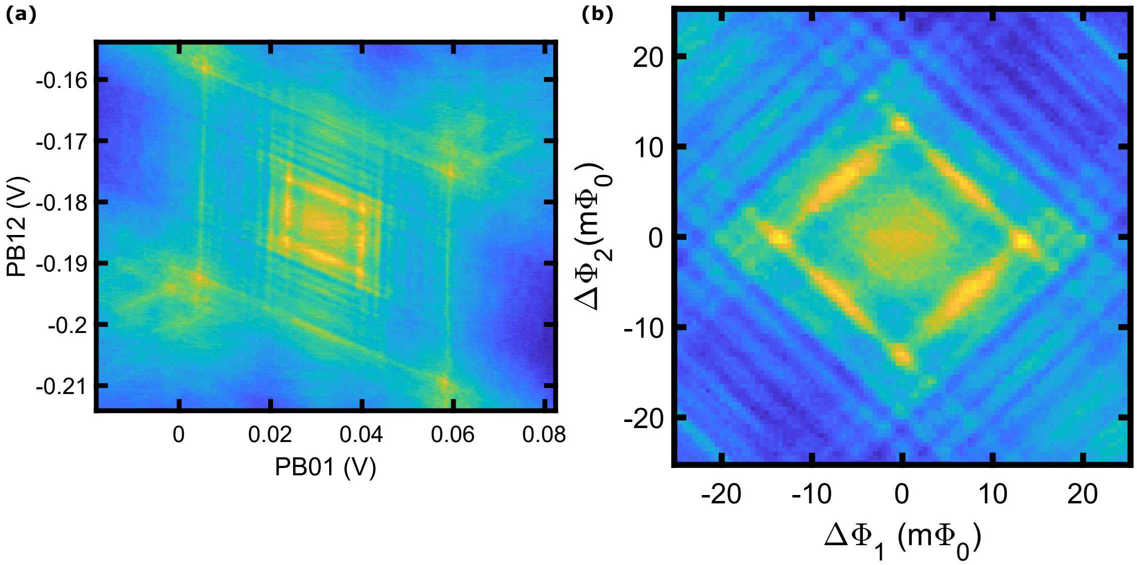

Figure 6.3: (a) Fine structure observed in a high-resolution scan of the cavity response while varying PB01 and PB12 near double frustration of Plaquettes 1 and 2. (b) Scanning pure Plaquette 1 and pure Plaquette 2 flux using the extracted inductance matrix, with centering at Plaquette 1/2 double frustration.

triple frustration.

To identify which plaquette corresponds to which set of parallel blue lines, we can look at Fig. 6.2(d). Plaquette 2 frustration corresponds to the negative slope blue lines, because PB12 and PB23 have the same sign of mutual inductance to the Plaquette 2 loop. Because PB12 and PB23 both have different sign of mutual inductance to the Plaquette 1 and Plaquette 3 loops, the two sets of positive slope parallel blue lines correspond to Plaquette 1 and Plaquette 3 frustration. PB12 is closer to Plaquette 1 than PB23. Thus, to maintain Plaquette 1 at frustration, a small change in PB12 requires a larger change in PB23, so the positive slope blue lines that have larger slopes correspond to Plaquette 1 being at frustration. The remaining set of blue lines corresponds to Plaquette 3 being at frustration. The period within the parallel lines corresponds to changing that plaquette loop by 1 Φ_0. We can calculate the inductance matrix from the different slopes and periods:

$$\vec{\Phi} = L\vec{I} + \vec{\Phi}_{offset}, \tag{6.1}$$

where $\vec{\Phi}$ is a vector that contains the three pure plaquette fluxes, $\vec{I}$ is a vector that

Simulated Inductance Matrix (pH)				
	PB01	PB12	PB23	PB30
Plaq1	0.594	0.775	-0.174	0.106
Plaq2	0.146	-0.688	-0.547	0.237
Plaq3	0.066	-0.201	0.599	0.756
Extracted Inductance Matrix (pH)				
	PB01	PB12	PB23	PB30
Plaq1	0.639	0.660	-0.146	0.053
Plaq2	0.201	-0.661	-0.539	0.155
Plaq3	0.134	-0.244	0.674	0.591

Table 6.1: Simulated and extracted inductance matrix.

contains the four plaquette bias currents, L is the mutual inductance matrix that has 3×4 matrix size, and $\vec{\Phi}_{offset}$ corresponds to the small background magnetic flux that can be trapped randomly near the plaquettes when the ground plane goes superconducting. These flux offsets can be stable for several weeks. We did a similar calculation for the SQUID switch elements [Fig. 6.2(e)], and then we bias the SQUID switches at unfrustration for all of the measurements shown here.

To protect the plaquettes from flux noise, we need to bias each plaquette at frustration to better than 1 mΦ_0 accuracy. The inductance matrix extracted based on Fig. 6.2 does not have such accuracy; instead, we rely on the symmetric fine structure observable in high-resolution flux scans of the cavity, such as the plot in Fig. 6.3(a), to refine the inductance matrix. As we tune the plaquettes towards double frustration, the higher level fluxon transitions disperse sharply and cross the cavity at small intervals, which causes the fine structure in the cavity signal. Calculating the slope and period based on the fine structure, we can get the flux accuracy of frustration to better than 1 mΦ_0. The corresponding extracted inductance matrix and simulated inductance matrix are shown in Table 6.1. The inductance matrix is simulated with InductEx, as mentioned in Ch. 5. Using this inductance matrix, we scan combinations of the plaquette flux lines to produce a scan of the pure Plaquette 1 flux and pure Plaquette 2 flux in Fig. 6.3(b), with centering at Plaquette 1/2 double frustration.

6.4 Spectroscopy measurement

In this section, I describe the initialization, spectroscopy vs. flux and spectroscopy vs. charge measurements of the 3-plaquette chip. The spectroscopy tone is joined with the shunt capacitor charge bias line with a bias-T on the mixing chamber. Because we are interested in a frequency range of 0.2 - 7 GHz, which is outside of our IQ mixer range, the spectroscopy pulse is controlled by a microwave switch without an IQ mixer. Our readout relies on the different cavity transmission when the plaquette chain is in different states.

6.4.1 Initialization

To describe the stabilizer behavior, we need to initialize the plaquettes in the $0/\pi$ basis for single frustration and even/odd basis for double frustration. We realize this by biasing the plaquettes we would like to frustrate to 100 mΦ_0 away from frustration in the direction where the π well is deep and the 0 well vanishes, thus allowing the phase particle to relax in the π well. In principle, we can choose an initialization flux larger than 100 mΦ_0, but applying a larger flux causes more significant flux distortions. If we choose an initialization flux smaller than 100 mΦ_0, the phase particle needs a longer time to fully relax in the π well. After initialization, we apply a fast flux pulse with a characteristic edge time of 500 ns, then we idle for 5 μs at this flux point, then apply a 5 μs spectroscopy pulse before reading out.

6.4.2 Single frustration

At single frustration, we initialize the plaquette in the π well. We show the single frustration flux dispersion data near single frustration in Fig. 6.4. The transitions that tune with flux gradually are plasmon transitions and the transitions that tune with flux rapidly are heavy fluxon transitions. The three sets of horizontal transitions near 2-2.5 GHz correspond to $|0_\pi\rangle \rightarrow |3_\pi\rangle$, $|1_\pi\rangle \rightarrow |3_\pi\rangle$, $|2_\pi\rangle \rightarrow |5_\pi\rangle$. The plaquette system has nonzero occupation in the higher energy states because the plasmon transition energies are rather low compared to k_BT and the large shunt capacitor acts as an antenna that absorbs high energy photons that drive spurious excitations of the plaquettes [68].

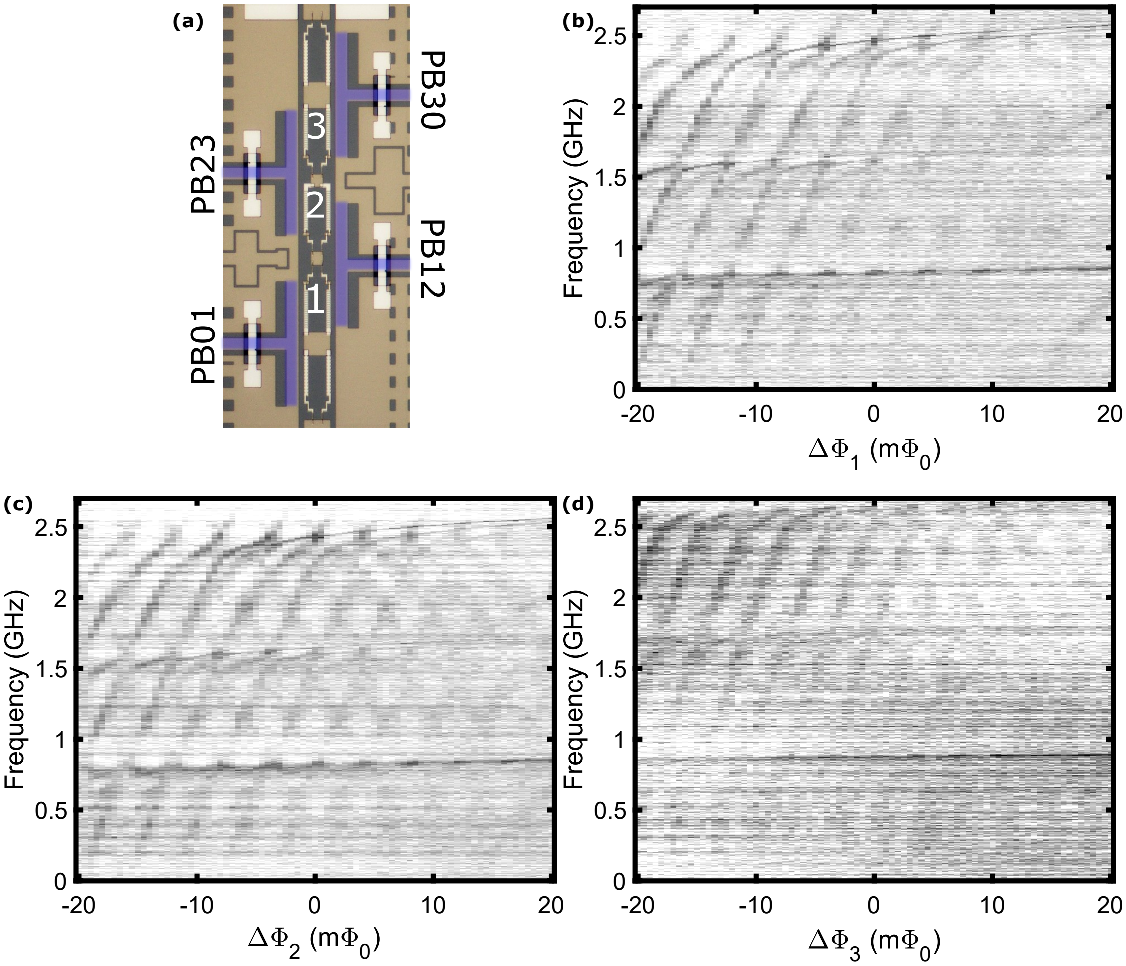

Figure 6.4: (a) Device image and blue false-color highlighting of plaquette flux-bias lines. Single frustration spectroscopy measurement vs. flux for (b) Plaquette 1, (c) Plaquette 2, (d) Plaquette 3.

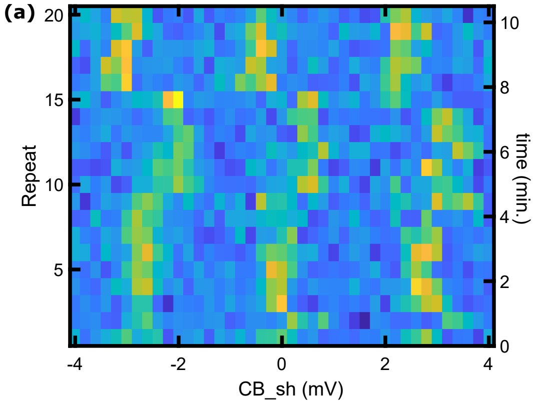

Figure 6.5: Repeated measurements of the cavity modulation with the offset charge bias to the shunt capacitor island.

We see multiple heavy fluxon transitions, which correspond to transitions from $|0_\pi\rangle, |1_\pi\rangle, |2_\pi\rangle$ to energy levels in the 0 well near the top of the barrier. Although the heavy fluxon transitions for $|0_\pi\rangle \rightarrow |0_0\rangle$ or $|1_\pi\rangle \rightarrow |1_0\rangle$ have small matrix elements because of the large C_{sh}, the heavy transitions from the lower energy in the π well to the energy levels near top of the barrier in the 0 well have larger matrix elements. The positive slope of the dominant heavy fluxon transitions shows that we initialize the plaquette predominantly in the π well.

As described in Ch. 3 and 4, the energy levels and transition frequencies tune with the offset charge on the logical island charge due to the Aharonov-Casher effect, but the large C_{sh} and large barrier cause the maximum splitting for the low-lying levels to be small. When α is 0, the splitting should modulate to 0 periodically with the offset charge. When α is not 0, the splitting modulates to a smaller value, but not to 0. We will discuss in Ch. 7 that the expected charge modulation amplitude is comparable to the spectroscopy line width for the actual value of α on our device, which prevents seeing the charge modulation directly of the low-lying level splittings with the C_{sh} offset charge. However, the higher-level transitions have significant charge modulation and are close to the readout cavity frequency. This results in the cavity transmission tuning with the offset charge on the logical island (Fig. 6.5). There are random shifts of the total background offset charge besides the offset charge induced by the charge bias line. This can be explained by high energy particles colliding with the Si substrate of our device, which generates a large number of electron-hole pairs that

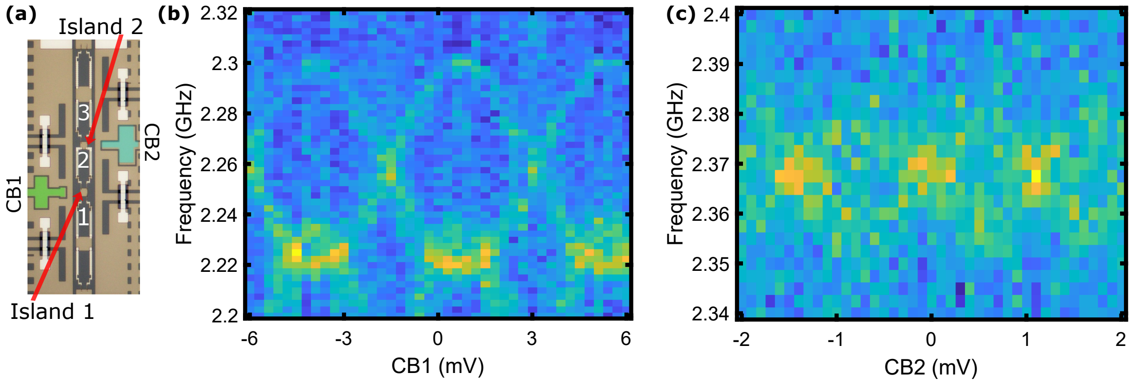

Figure 6.6: (a) Device image and false-color highlighting of charge-bias lines. (b) Plaquette 1/2 double frustration spectroscopy at 17 mΦ_0 vs. offset charge on island between Plaquette 1 and Plaquette 2 with two quasiparticle bands. (c) Plaquette 2/3 double frustration spectroscopy at 11 mΦ_0 vs. offset charge on island between Plaquette 1 and Plaquette 2 with two quasiparticle bands.

diffuse based on the band structure. Eventually, they are trapped in defects and change the local charge environment [57, 84, 54]. The background charges jump on average every few minutes because of the large charge sensing area of C_{sh} for this device. A future parallel-plate capacitor could be much more compact and have a much smaller sensing area, which we will discuss in Ch. 8.

6.4.3 Double frustration

Near double frustration, we initialize the two plaquettes in the $\pi\pi$ well, then do a 500 ns Gaussian ramp to a range of flux points along the direction from 00 to $\pi\pi$ and passing through double frustration. Analogous to the Aharonov-Casher effect, the energy levels near double frustration depend on the offset charge both on the shunt capacitor and on the intermediate island between the frustrated plaquettes. Similarly to the single frustration case, the modulation of the splittings for the low-lying levels with the offset charge on the shunt capacitor island has a rather small amplitude. However, the modulation amplitude for the offset charge on the intermediate is large due to the small C_{isl}. In Fig. 6.6(a), we measure the spectroscopy at 17 mΦ_0 near Plaquette 1/2 double frustration, while scanning the offset charge on the intermediate island between Plaquette 1/2, and the modulation amplitude is ~40 MHz. In

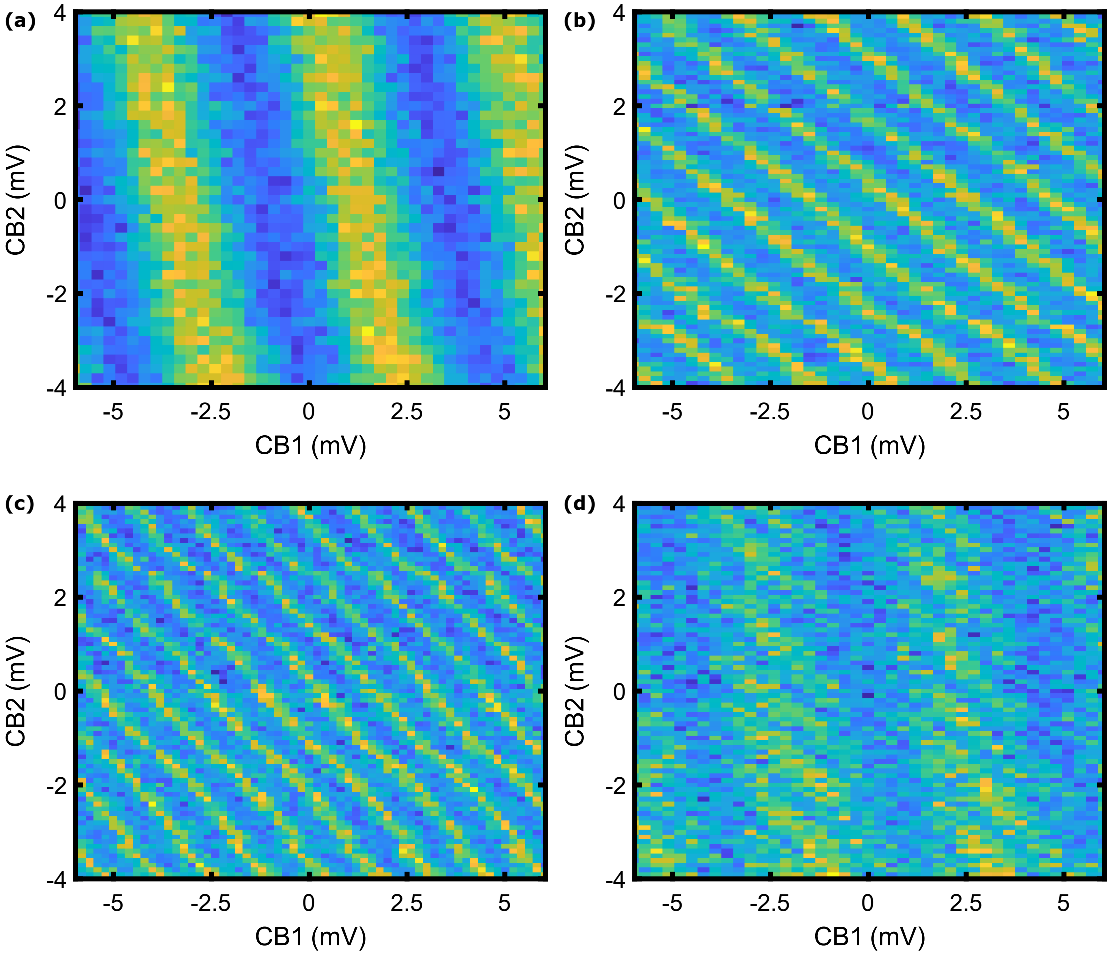

Figure 6.7: Cavity transmission vs. CB1 and CB2 for (a) Plaquette 1/2 double frustration, (b) Plaquette 2/3 double frustration, (c) Plaquette 1/3 double frustration, (d) Plaquette 1/2/3 triple frustration.

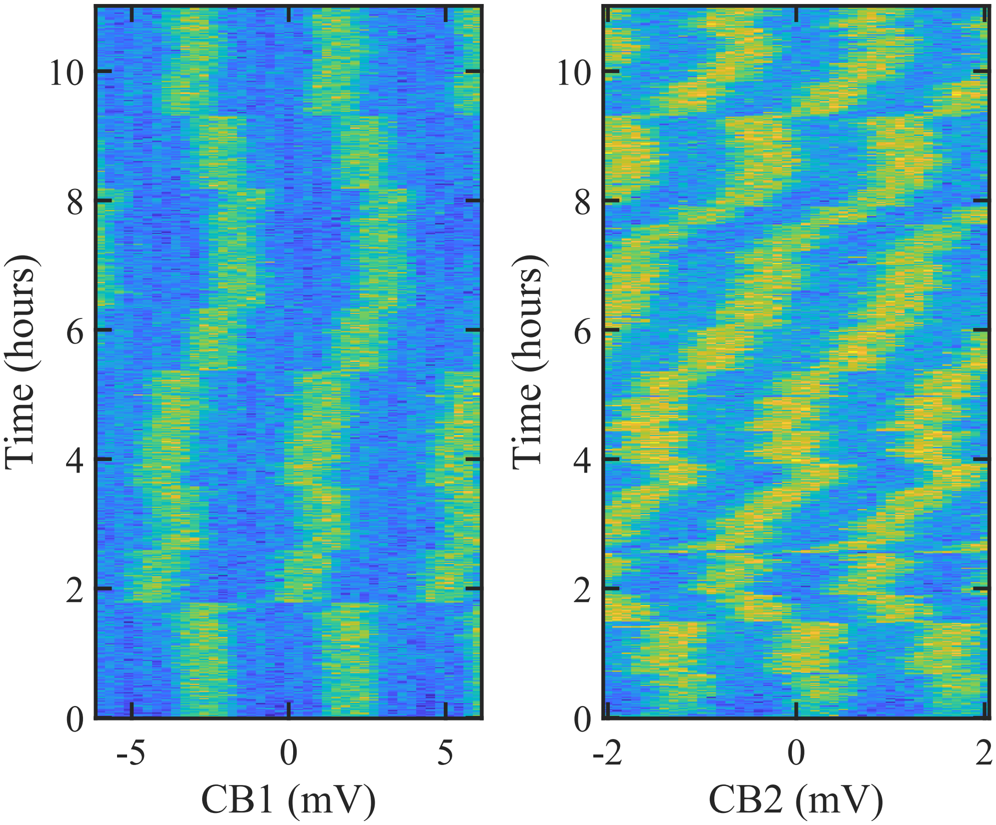

Figure 6.8: Island 1 and 2 charge modulation drift over 11-hour span. Nearly simultaneous measurement for the charge offset on Island 1 and Island 2. The scan is performed by first scanning island charge for Plaquette 1/2 double frustration while keeping Plaquette 3 at 50 mΦ_0. The flux is then pulsed quickly to Plaquette 2/3 double frustration, while keeping Plaquette 1 at 50 mΦ_0.

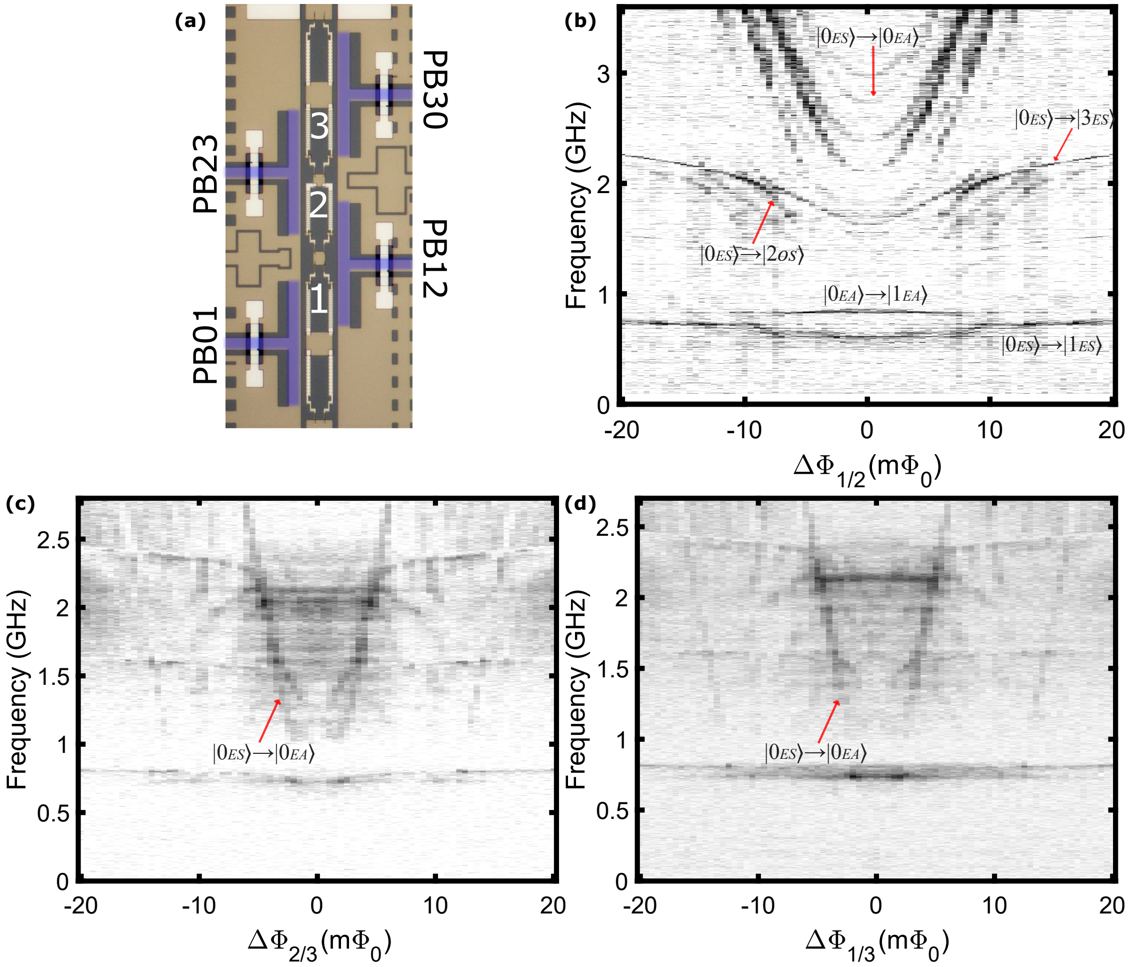

Figure 6.9: (a) Device image and false-color highlighting of flux-bias lines. Double frustration spectroscopy vs. flux for (a) Plaquette 1/2 double frustration, (b) Plaquette 2/3 double frustration, (c) Plaquette 1/3 double frustration. The flux for both plaquettes is scanned along the line from 00 to $\pi\pi$ and passing through double frustration.

Simulated capacitance matrix (aF)			
	$\mathrm{CB_{sh}}$	CB1	CB2
$\mathrm{Island_{sh}}$	54	419	351
Island 1	0	36	8
Island 2	0	78	122
Extracted capacitance matrix (aF)			
	$\mathrm{CB_{sh}}$	CB1	CB2
$\mathrm{Island_{sh}}$	57	501	327
Island 1	0	35	6
Island 2	0	73	120

Table 6.2: Simulated and experimentally extracted capacitances between the charge bias lines (CB) and different islands.

Fig. 6.6(b), we measure the spectroscopy at 11 mΦ_0 near Plaquette 2/3 double frustration, while scanning the offset charge on the intermediate island between Plaquette 2/3, and the modulation amplitude is ∼25 MHz. We can see the two quasiparticle bands clearly in these scans.

In Fig. 6.7, we show an example of the offset charge scan for Plaquette (a) 1/2, (b) 2/3, (c) 1/3, and (d) 1/2/3 frustrations. For Plaquette 1/2 double frustration, we can see the features modulate faster with the CB1 line because it is closer to Island 1. For the Plaquette 2/3 double frustration, we see a faster charge modulation for both CB1 and CB2. This is because part of the junction chain contributes to the Island 2 and makes the effective island bigger capacitance to ground. For Plaquette 1/3 double frustrtion, the charge modulation is even faster, because now the whole Plaquette 2 and the geometric Island 1 and Island 2 become the effective intermediate island. From these scans, we can extract the capacitance matrix and compare with the simulated capacitance matrix (Table 6.2); the agreement is good.

Because the intermediate island is much smaller than the shunt capacitor, the charge sensing area for the background offset charge drift and discrete jumps s smaller. We observe the intermediate island offset charge to be stable for timescales of roughly 30 minutes, compared to the 2-minute timescale between jumps of the offset charge on the much larger shunt capacitor island. In Fig. 6.8, we show a nearly simultaneous measurement for the charge offset on Island 1 and Island 2. The scan is performed by first scanning the island charge for Plaquette 1/2 double frustration, while keeping Plaquette 3 at 50 mΦ_0. We then pulse the flux bias quickly to Plaquette 2/3 double frustration while keeping Plaquette 1 at 50 mΦ_0. We observe somewhat larger drift and offset charge jumps for Island 2 compared to Island 1 because of the larger sensing area.

Because of the large modulation with offset charge on the intermediate island at double frustration, for long spectroscopy measurements, we must stabilize this offset charge at a particular value to compensate for occasional offset charge jumps. The charge stabilization is performed by applying a spectroscopy tone at the 0-1 transition while scanning one of the offset charge bias lines. The spectroscopy vs. flux data is shown in Fig. 6.9, with the offset charge on the intermediate island between the frustrated plaquettes stabilized at $0e$. In contrast to single frustration, the double frustration spectroscopy data is symmetric with respect to flux because the small C_{isl} causes strong coupling between the 00 and $\pi\pi$ wells. In the context of Landau-Zener tunneling [85], our coupling energy is $\sim$ 2.4 GHz for Plaquette 1/2 double frustration and $\sim$ 0.5 GHz for Plaquette 1/3 double frustration, and our fast ramp is 500 ns that corresponds to $\sim$2 MHz, so our ramp is an adiabatic process, which results in the plaquettes remaining in the ground state and transitioning smoothly from the 00 well to the $\pi\pi$ well upon passing through frustration. We choose a readout flux point for which the signal is strong for a $0e$ offset charge and weak for a $1e$ offset charge, so that even though we have fast quasiparticle poisoning, we only see the transitions at $0e$ offset charge and do not see the transitions at $1e$ offset charge.

For the double frustration flux spectroscopy scans in Fig. 6.9, the transitions that disperse gradually with flux are the plasmon transitions. Similar to single frustration, we see the transitions out of $|0_{ES}\rangle$ and $|1_{ES}\rangle$ states, where E corresponds to the even-parity energy levels, and S corresponds to symmetric energy levels. In addition to these transitions, near Plaquette 1/2 double frustration, we see a downward dispersing transition at $\sim$ 800 MHz. This is the $|0_{EA}\rangle \rightarrow |1_{EA}\rangle$ transition caused by the fast quasiparticle poisoning which results in some population in the $|0_{EA}\rangle$ excited state.

Near Plaquette 1/2 double frustration, we can see the heavy fluxon transitions below 2.25 GHz, which correspond to transitions between the even-parity energy levels and odd-party energy levels. For example, the transition near 2 GHz at around

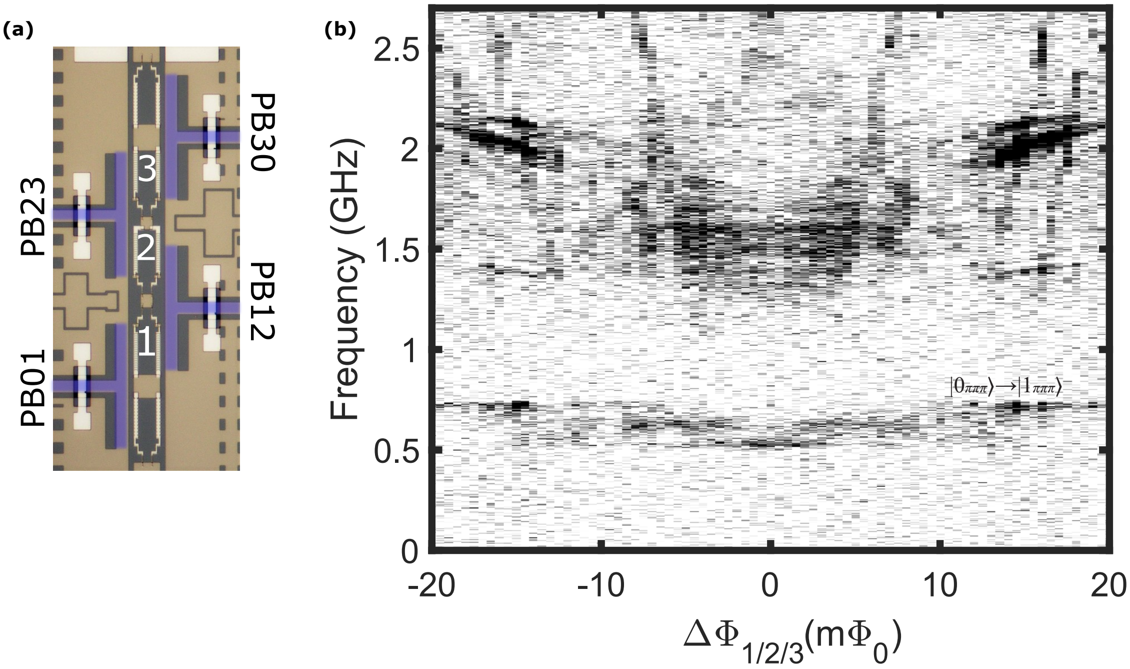

Figure 6.10: (a) Device image and false-color highlighting of the flux-bias lines. (b) Spectroscopy vs. flux at triple frustration by simultaenously scanning the three plaquette fluxes along the direction from 000 to $\pi\pi\pi$ and passing through triple frustration.

8 mΦ_0 corresponds to $|0_{ES}\rangle \rightarrow |2_{OS}\rangle$.

The transitions with the largest slopes correspond to light fluxon transitions, which are between levels with the same parity but between symmetric and antisymmetric levels. For example, within ±5 mΦ_0, the transitions above 2 GHz for 1/2 double frustration, the transitions between 1-2.7 GHZ for 2/3 double frustration, and the transitions between 0.5-2.7 GHz for 1/3 double frustration are the light fluxon transitions. Near Plaquette 2/3 and 1/3 double frustration near 12-18 mΦ_0, we observe another light fluxon transition, which is the transition involving an excitation in the readout cavity.

6.5 Triple frustration

In Fig. 6.7(d), we apply the spectroscopy tone at the 0-1 plasmon transition for the triple frustration, and scan the offset charge bias to the two intermediate islands between the plaquettes with CB1 and CB2. Because there are two relevant islands at triple frustration, we observe two periods: one along the pure Island 1 charge, the other along the pure Island 2 charge.

Near triple frustration, we initialize the three plaquettes in the $\pi\pi\pi$ well, then do a 500 ns Graussian ramp to a range of flux points along the direction from 000 to $\pi\pi\pi$ and passing through triple frustration. The transitions that tune with flux gradually are plasmon transitions. In general, we observe flatter curvature for the dispersion of the various transitions at triple frustration compared to double frustration.

Chapter 7

Fitting of spectroscopy measurements

In this chapter, I describe the process for fitting spectroscopy data vs. flux for single, double, and triple frustrations. I demonstrate that we can fit the plasmon, heavy fluxon, and light fluxon transitions within 10% difference of the spectroscopy data with parameter values that are consistent with our device design and fabrication.

7.1 General fitting strategy

Before fitting, we need to identify the transitions correctly in our model of the energy-level spectrum. To visualize this issue, we can study Fig. 7.1. Here, we use the notation that the levels without a subscript have the numerical value of the level counting up in energy from the ground state at 0 for a given flux; for the levels with subscripts, the subscript accounts for which well the level resides in (at least for the states below the barrier). Between 5 to 20 mΦ_0, the lowest transition ($|0\rangle \rightarrow |1\rangle$ transition) is the plasmon transition $|0_\pi\rangle \rightarrow |1_\pi\rangle$. However, between 0 to 4 mΦ_0, the lowest transition ($|0\rangle \rightarrow |1\rangle$ transition) corresponds to the heavy fluxon transition $|0_\pi\rangle \rightarrow |0_0\rangle$. Also, the $|0_\pi\rangle \rightarrow |1_\pi\rangle$ is the $|0\rangle \rightarrow |2\rangle$ transition between 0 to 4 mΦ_0. Between -4 to 0 mΦ_0, the $|0_\pi\rangle \rightarrow |1_\pi\rangle$ is the $|1\rangle \rightarrow |3\rangle$ transition. We use the initial parameters to calculate the energy levels, which generally match the data qualitatively, and from this we can identify most of the transitions. During the first round, we only fit the transitions that we have identified correctly. After that, the fitted energy levels typically match with the data quite well and we can identify more transitions. We then use the newly identified transitions to further refine the fit.

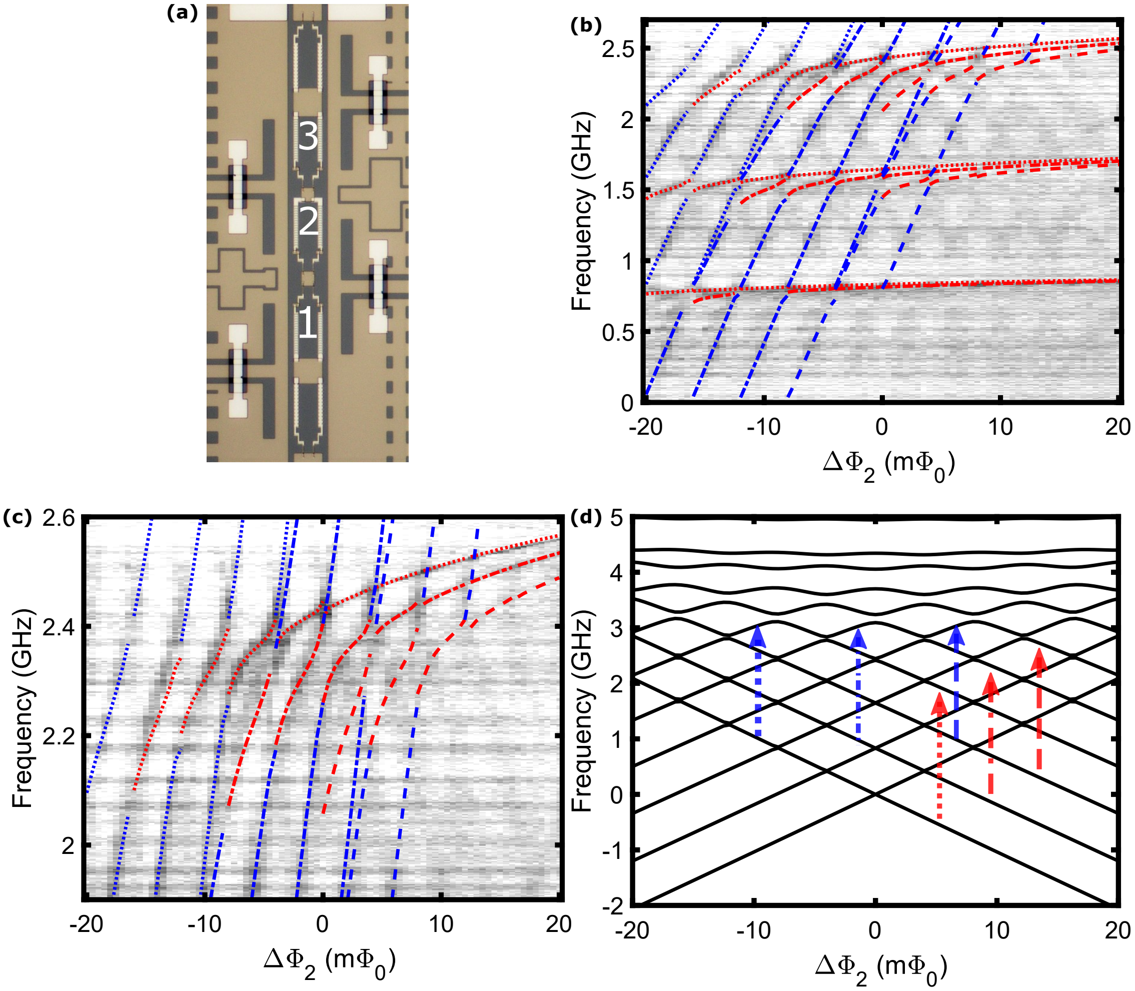

Figure 7.1: (a) Device image. (b) Plaquette 2 single frustration fitting. The red lines are plasmon transitions, blue lines are fluxon transitions. The dotted lines are transitions out of the $|0_\pi\rangle$ state. The dash-dotted lines are transitions out of $|1_\pi\rangle$ state. The dashed lines are transitions out of $|2_\pi\rangle$ state. (c) Zoomed-in plaquette 2 single frustration fitting. (d) Fitted energy levels with arrows indicating corresponding transitions from spectroscopy measurements.

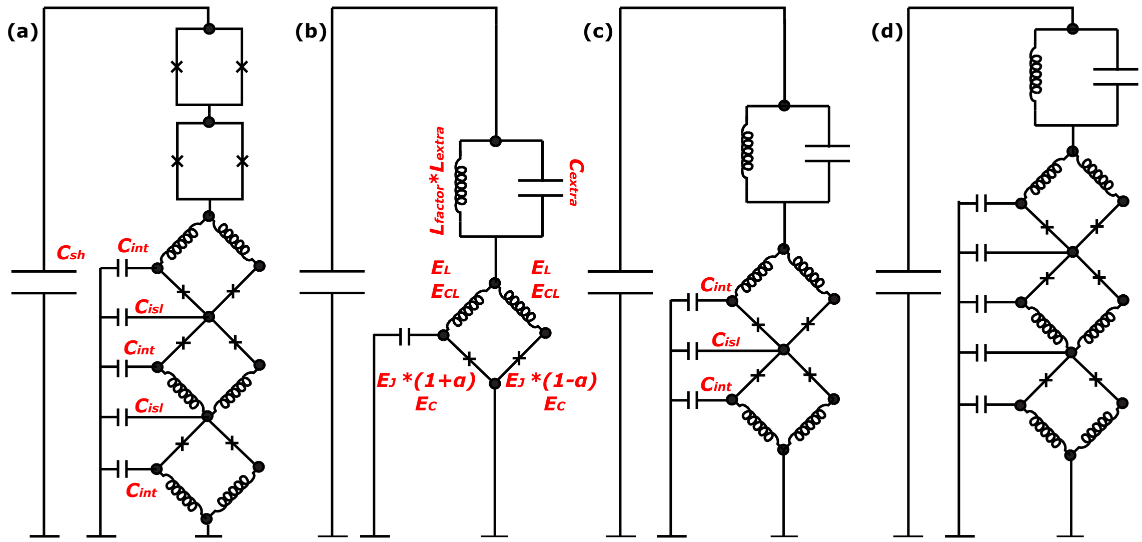

Figure 7.2: Circuit schematic. Same figure as Fig. 4.1. (a) 3-plaquette chip circuit schematic. (b) Schematic of single frustration modeling. (c) Schematic of double frustration modeling. (d) Schematic of triple frustration modeling.

After extracting the plasmon transitions, heavy fluxon transitions, light fluxon transitions, and anticrossings from the spectroscopy flux dependence and charge dependence data, we use the single (double) plaquette model for the energy-level spectra described in Ch. 4 to fit the single (double) frustration spectroscopy data. At single frustration, we fit E_J, E_C, E_L, E_{CL}, C_{sh}, α, L_{factor} using the model showed in Fig. 7.2(b). We fix C_{int} to be 1 fF, which is estimated from Q3D modeling and a theoretical estimation of the effect of the junction chain capacitance to ground. We introduce the parameter L_{factor} to account for variations in L_{extra} due to small flux offsets in the bias of the nominally unfrustrated plaquettes or SQUIDs. At double frustration, we fit the same parameter set as in the single frustration case, but with the addition of C_{isl}. Similarly to the single frustration case, we fix C_{int} to be 1 fF. We assume the two plaquettes at frustration share the same set of parameters, because the actual parameters between the two plaquettes are typically only different by a few percent based on our test structures during the device fabrication. This allows us to reduce the fitting parameters from 15 to 8, and thus makes the fitting more practical.

The cost function of our fitting procedure is $\sum_n W_n \Delta f_n^2$, where Δf_n is the difference between the modeled and experimental frequencies for transition n, and W_n is the weight that we assign to transition n. The goal of the fitting process is to minimize the cost function and find the parameter set that has less than a 10% difference between the modeled transitions and the experimental transitions. We use the scipy.optimize.minimize function in Python to do the fitting. We have 7 and 8 parameters for single and double frustration fitting, respectively. We find that the Nelder-Mead method fits better than gradient descent methods in terms of avoiding local minima.

With this high-dimensional fit, we need to choose the initial parameters carefully. We use the initial E_J and E_L values calculated from the Ambegaokar-Baratoff relation [Eq. (2.18)], using the on-chip test junction resistances. The initial α of the junctions is estimated from our test chips that each contain 6 identical junctions. As mentioned in Sec. 2.4.1, we will define the charging energy as $E_C \equiv (2e)^2/2C$. The initial E_C and E_{CL} values are calculated from the the relevant junction areas measured with scanning electron microscopy with a total specific capacitance ~70 fF/μm^2 specific capacitance. The initial C_{sh} is estimated from Q3D simulation. The initial L_{factor} is set to 1 because our unfrustrated plaquettes are nominally biased at unfrustration. We choose the initial simplex for the minimization so that it covers the possible parameter range, which is typically ±5% to ±30% of the initial values.

7.2 Single frustration fitting

Initially, we fit the single frustration data with our single plaquette model [Fig. 7.2(b)]. We put equal weight on different transitions by setting $W_n = 1$ for the fitting. The fit runs on a computer with a 12-core processor and takes ~1 day and 500 iterations to converge. In Fig. 7.1(b), we show the fitting of plaquette 2 single frustration. The red lines correspond to the fitted plasmon transitions, and the blue lines correspond to the fitted heavy fluxon transitions. The dotted lines are transitions out of the $|0_\pi\rangle$ state. The dash-dotted lines are transitions out of the $|1_\pi\rangle$ state. The dashed lines are transitions out of the $|2_\pi\rangle$ state. In Fig. 7.1(c), we zoom in near the anticrossings and show the anticrossings also fit well. The transitions match with the data within 10% error. In Fig. 7.1(d), we show the modeled energy levels using the fitting parameters

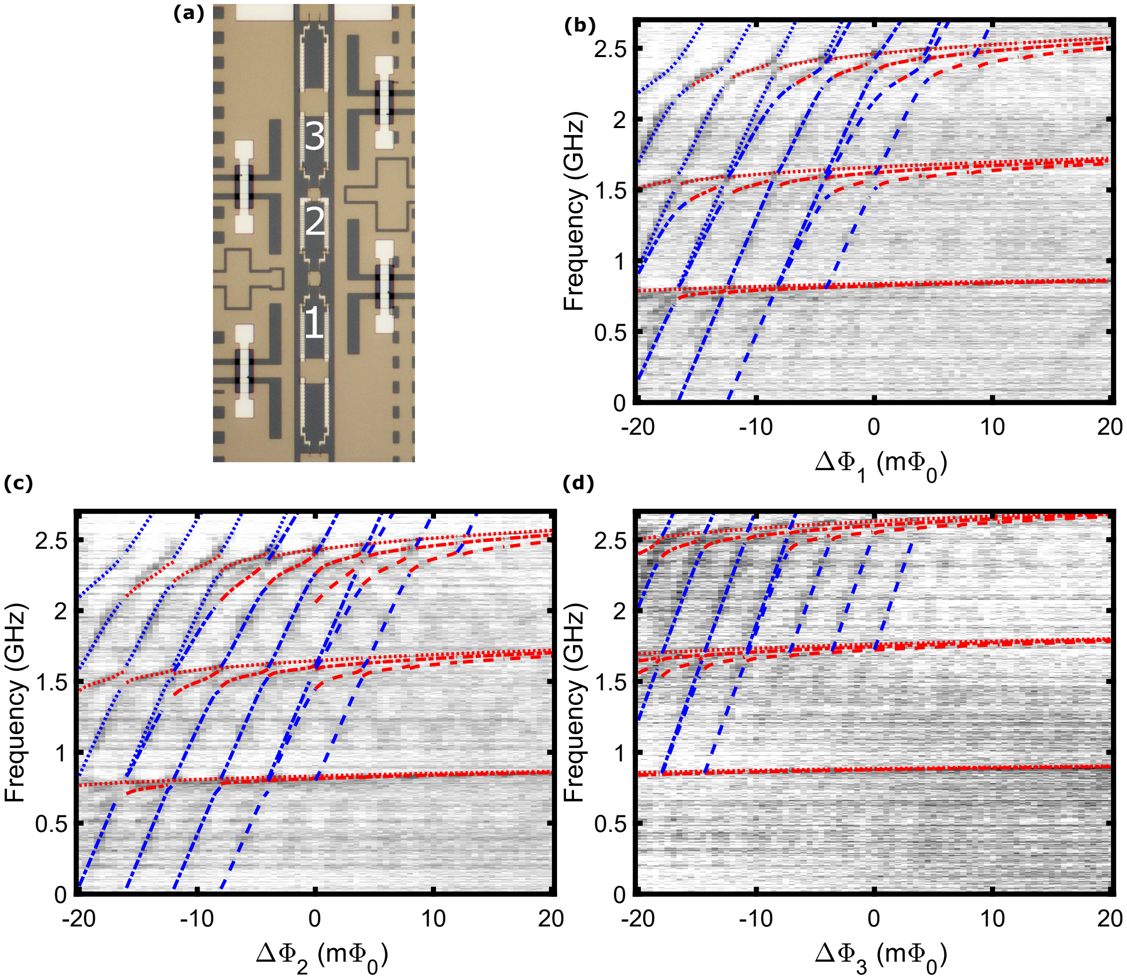

Figure 7.3: (a) Device image. Single frustration data and fitting of (b) Plaquette 1 , (c) Plaquette 2 and (d) Plaquette 3. The red lines are plasmon transitions, blue lines are fluxon transitions. The dotted lines are transitions out of the $|0_\pi\rangle$ state. The dash-dotted lines are transitions out of $|1_\pi\rangle$ state. The dashed lines are transitions out of $|2_\pi\rangle$ state.

	E_J (K)	E_C (K)	E_L (K)	E_{CL} (K)	C_{sh} (fF)	α	L_{factor}
Plaquette 1	1.65	3.65	1.12	5.60	1160	0.03	1.1
Plaquette 2	1.65	3.67	1.11	6.36	1190	0.02	1.1
Plaquette 3	1.97	4.00	1.27	6.66	1440	0.04	0.91
Estimated parameters	1.45	3.82	1.39	6.46	1000	0.02	1.0

Table 7.1: Single frustration fitted parameters and estimated parameters from design and fabrication tests.

and indicate some example plasmon and fluxon transitions out of the $|0_\pi\rangle$, $|1_\pi\rangle$ and $|2_\pi\rangle$ states.

In Fig. 7.3(b-d), we show the single frustration fitting of Plaquette 1, 2, 3 single frustration. Plaquette 1 behaves similarly to Plaquette 2, so the fitted transitions and parameter values are similar. Plaquette 3 single frustration behaves somewhat differently, and the fitted energy levels and parameters parameters differ by a larger amount compared to Plaquettes 1 and 2. The fitted parameters are listed in Table 7.1 and they are within 20% of the of the parameters that we estimate from the design and fabrication tests, although a few of the parameters for Plaquette 3 have a slightly larger discrepancy. The spectroscopy measurements at Plaquette 3 single frustration are not as clean as for Plaquettes 1 and 2 single frustration, thus potentially accounting for the larger variation with the estimated values. We will discuss estimates for bounds on the uncertainties in the fitting parameters in Sec. 7.5.

7.3 Double frustration fitting

We next use the model in Fig. 7.2(c) to fit the double frustration data. Because the Hilbert space is ∼11 times larger at double frustration using this model, we use a 48-core computer to do the fitting. This process takes between 4-7 days and ∼ 300 iterations to converge. The anticrossings between different transitions are important features to fit because they determine the coupling between the computational states, so we put ∼20 times more weight for the regions in the spectroscopy data that exhibit

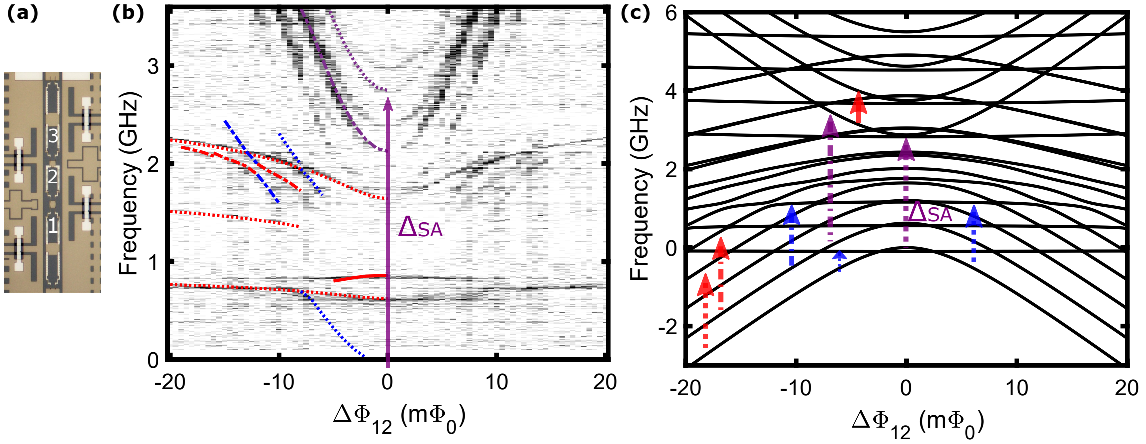

Figure 7.4: (a) Circuit image. (b) Flux spectroscopy data and fitting of Plaquette $1/2$ double frustration. The red lines are the fitted plasmon transitions, the blue lines are the fitted heavy fluxon transitions, the purple lines are the fitted light fluxon transitions. The dotted lines are transitions out of the $|0\rangle$ state of the symmetric energy levels in the even-parity wells. The dash-dotted lines are transitions out of $|1\rangle$ state of the symmetric energy levels in the even-parity wells. The dashed lines are transitions out of $|2\rangle$ state of the symmetric energy levels in the even-parity wells. The solid red line is the plasmon transition between the antisymmetric energy levels in the even-parity well. (c) Calculated energy-level spectrum using the fitting parameters with arrows indicating the various corresponding transitions from the spectroscopy data.

significant anticrossings. We also simultaneously fit the corresponding charge modulation data and we only use the minimum and maximum of the charge modulation for fitting. In order to compensate for the relatively small number of charge modulation data points, we put $\sim$50 times more weight for these features in the fitting.

In Fig. 7.4(b), we show the Plaquette $1/2$ double frustration data and fitted transitions. The red lines are the fitted plasmon transitions, the blue lines are the fitted heavy fluxon transitions, the purple lines are the fitted light fluxon transitions. The dotted lines are transitions out of the $|0_{ES}\rangle$ state, where E corresponds to the even-parity hybridized well between Plaquettes 1 and 2, S corresponds to the symmetric hybridized energy level of Plaquettes 1 and 2 and 0 corresponds to the lowest energy level with these conditions. The dash-dotted lines are transitions out of $|1_{ES}\rangle$ and the

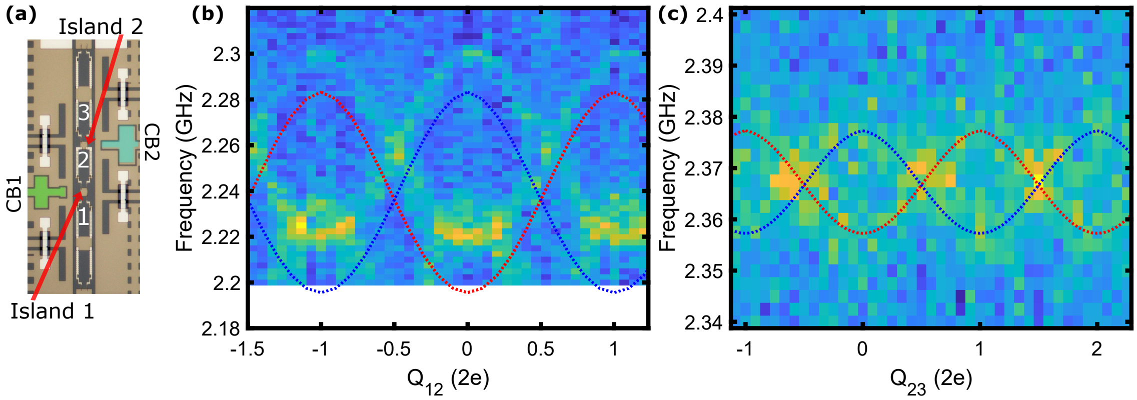

Figure 7.5: (a) Circuit image. (b) Plaquette 1/2 double frustration charge modulation data of $|0_{ES}\rangle \rightarrow |3_{ES}\rangle$ transition at 17 mΦ_0. The red and blue dotted lines are the fitted transitions that correspond to different quasiparticle parity on intermediate Island 1. (c) Plaquette 2/3 double frustration charge modulation data of $|0_{ES}\rangle \rightarrow |3_{ES}\rangle$ transition at 11 mΦ_0. The red and blue dotted lines are the fitted transitions that correspond to different quasiparticle parity on intermediate Island 2.

dashed lines are transitions out of $|2_{ES}\rangle$ state. The red solid line is $|0_{EA}\rangle \rightarrow |1_{EA}\rangle$, which is the transition out of the 0 state of the antisymmetric energy levels in the even-parity wells to the 1 state of the antisymmetric energy levels in the even-parity wells. We see this transition because we have quasiparticle poisoning on the intermediate islands that is faster than our measurement timescale. When we prepare the qubit in the $|0_{ES}\rangle$ state, the fast quasiparticle poisoning closes and opens the symmetric and antisymmetric gap randomly, which allows the system to occasionally transfer population from the $|0_{ES}\rangle$ to $|0_{EA}\rangle$ states, thus leaving population in the excited antisymmetric state. This results in the transition indicated by the solid red line in Fig. 7.4(b). In Fig. 7.5(b), we show the Plaquette 1/2 double frustration charge modulation data of the $|0_{ES}\rangle \rightarrow |3_{ES}\rangle$ transition at 17 mΦ_0. We can see clearly two quasiparticle bands. The red and blue dotted lines are the fitted transitions that correspond to different quasiparticle bands. We show the fitted energy levels and corresponding transitions in Fig. 7.4(c). In Fig. 7.5(c), we show the Plaquette 2/3 double frustration charge modulation data of $|0_{ES}\rangle \rightarrow |3_{ES}\rangle$ transition at 11 mΦ_0.

In Fig. 7.6(b-d), we show the fit results for the flux spectroscopy at Plaquette 1/2,

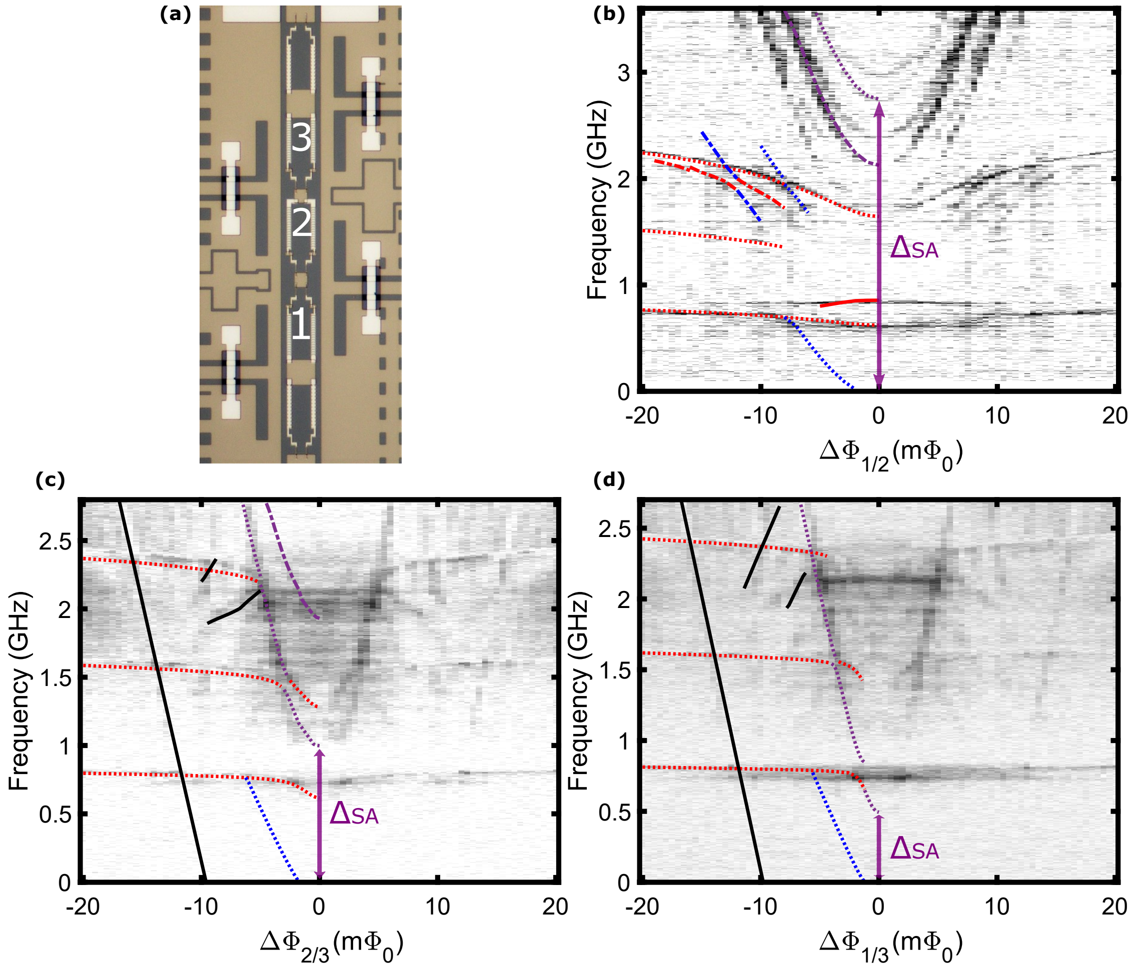

Figure 7.6: (a) Device images and plaquette labeling. Flux spectroscopy data and fitting of (b) Plaquette 1/2, (c) Plaquette 2/3 and (d) Plaquette 1/3. The red lines are the fitted plasmon transitions, the blue lines are the fitted heavy fluxon transitions, the purple lines are the fitted light fluxon transitions. The dotted lines are transitions out of the 0 state of the symmetric energy levels in the even-parity wells. We denote it as $|0_{ES}\rangle$. The dash-dotted lines are transitions out of 1 state of the symmetric energy levels in the even-parity wells, $|1_{ES}\rangle$. The dashed lines are transitions out of $|2_{ES}\rangle$ state. The solid black lines between -20 to -10 $\mathrm{m}\Phi_0$ in the Plaquette 2/3 and 1/3 double frustration correspond to transitions involving the cavity: $|0_{ES}, n\rangle \rightarrow |1_{EA}, n-1\rangle$, where n and $n-1$ inside the ket are the photon numbers in the cavity. The solid black lines between -10 to -0 $\mathrm{m}\Phi_0$ in the Plaquette 2/3 double frustration correspond to $|0_{OS} \rightarrow 5_{ES}\rangle$ and $|1_{OS} \rightarrow 6_{ES}\rangle$. The solid black lines between -10 to -0 $\mathrm{m}\Phi_0$ in the Plaquette 1/3 double frustration correspond to $|0_{OS} \rightarrow 4_{ES}\rangle$ and $|0_{EA} \rightarrow 4_{OA}\rangle$.

	E_J (K)	E_C (K)	E_L (K)	E_{CL} (K)	C_{sh} (fF)	α	C_{isl} (fF)	L_{factor}
plaquette 1/2	1.75	3.54	1.20	6.34	1240	0.03	1.52	0.99
plaquette 2/3	1.76	3.53	0.900	7.40	1290	0.04	5.68	1.0
plaquette 1/3	1.73	3.48	0.903	6.62	1310	0.03	8.14	0.98
Estimated parameters	1.45	3.82	1.39	6.46	1000	0.02	Vary	1.0

Table 7.2: Double frustration fitted parameters and estimated parameters
The estimated C_{isl} for Plaquette 1/2 and 2/3 double frustration are 1.17, 3.10.

2/3, and 1/3 double frustration. The Δ_{SA} for 1/2, 2/3 and 1/3 double frustration are $\sim$ 2.7, 0.8 and 0.5 GHz, as expected for a decreasing Δ_{SA} and less weaker hybridization for a larger intermediate island capacitance to ground. The fitted curves capture the transitions, anticrossings, and charge modulation to within 10% error. The fitted parameters are show in Table 7.2. The fitted parameters are close to our estimated parameters.

In Fig. 7.6(c,d), the solid black lines between -20 to -10 mΦ_0 in the Plaquette 2/3 and 1/3 double frustration correspond to transitions involving the readout cavity: $|0_{ES}, n\rangle \rightarrow |1_{EA}, n-1\rangle$, where n and $n-1$ inside the ket are the photon numbers in the cavity. The solid black lines between -10 to -0 mΦ_0 in the Plaquette 2/3 double frustration correspond to $|0_{OS} \rightarrow 5_{ES}\rangle$ and $|1_{OS} \rightarrow 6_{ES}\rangle$. The solid black lines between -10 to -0 mΦ_0 in the Plaquette 1/3 double frustration correspond to $|0_{OS} \rightarrow 4_{ES}\rangle$ and $|0_{EA} \rightarrow 4_{OA}\rangle$.

7.4 Triple frustration modeling

We model the triple frustration data with the model in Fig. 4.1(d). The Hilbert space of this triple frustration model is ~100 times larger than double frustration model. Modeling one flux point takes ~10 days, so it is impossible to model several flux

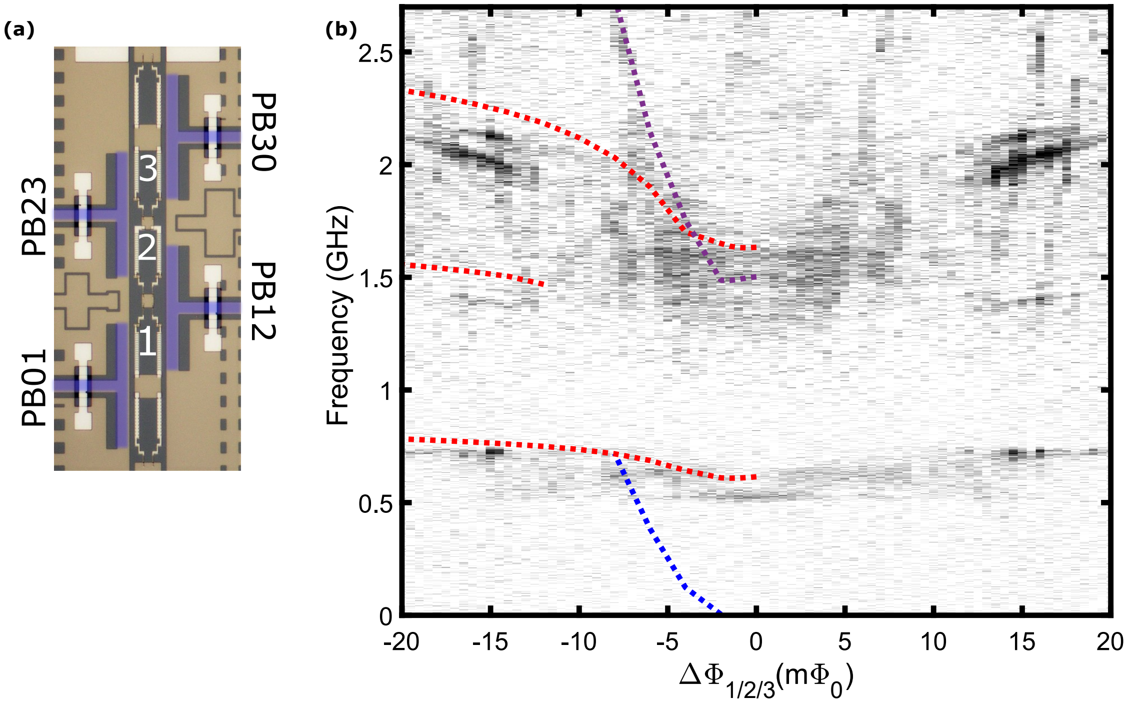

Figure 7.7: (a) Device image. (b) Flux spectroscopy data and fitting of Plaquette 1/2/3. The red lines are the modeled plasmon transitions, the blue line is the modeled heavy fluxon transition, the purple line is the modeled light fluxon transition. The dotted lines are transitions out of the 0 state of the symmetric energy levels in the even-parity wells.

points and fit to the triple frustration data. We model the triple frustration energy levels by simultaneously modeling different flux points on four virtual machines in parallel, which have 48-, 24-, 12- and 12-core processors, respectively. In each of the virtual machines, we use the multiprocess function in Python to model different flux points in parallel so that it uses all the computational power in that virtual machine. Because we cannot do the fitting, we use the fitted parameters from single and double frustration, and only adjust the L_{factor} to account for the SQUIDs not being at exact frustration. Figure 7.7 shows the triple frustration flux spectroscopy data and modeled transitions for Plaquette 1/2/3. The red lines are the modeled plasmon transitions, the blue line is the modeled heavy fluxon transition, the purple line is the modeled light fluxon transition. The dotted lines are transitions out of the 0 state of the symmetric energy levels in the even-parity wells. Based on our modeling, we find the plasmon and light fluxon transitions are in good agreement between our modeled curve and the triple frustration data. Thus, in general, the transitions at triple frustration have an even flatter dispersion with respect to flux compared to double frustration.

7.5 Fitted parameter error estimation

Each different type of transition has a different sensitivity to the various fitting parameters for the device. In order to estimate the error range for each fitted parameter, we compute the energy level spectrum while varying each parameter one at a time and keeping the other parameters at their best-fit values. We thus find the range over which each parameter can be varied while keeping the transition frequencies within 10% of the measured values. In Fig. 7.8, we show the four transitions we choose to estimate the fitted errors. In Table 7.3, we list the fitted errors obtained with this method for the $|0_{ES}\rangle \rightarrow |3_{ES}\rangle$ plasmon transition at 20 mΦ_0. From this table, we see the plasmon transition is sensitive to E_J, E_C, E_L, C_{sh} and L_{factor}, so we are confident of the parameters extracted from fitting the plasmon transitions. In Table 7.4, we list the fitted errors for the $|0_{ES}\rangle \rightarrow |2_{OS}\rangle$ heavy fluxon transition at 6.5 mΦ_0. The heavy fluxon transition is especially sensitive to E_J, E_C, while moderately sensitive to the rest of the parameters, so by fitting to the heavy fluxon transition, we can trust the fitted E_J, E_C with especially high confidence, with moderate confidence in the rest

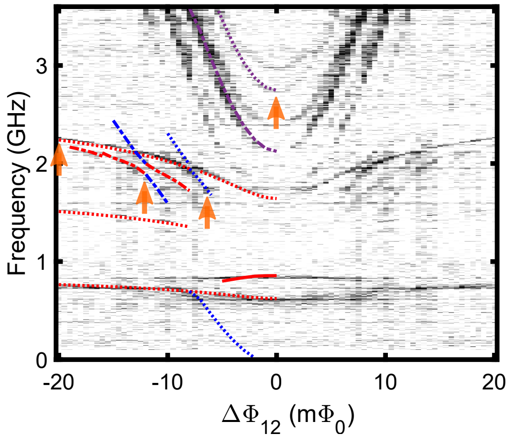

Figure 7.8: Flux spectroscopy data and fitting of Plaquette 1/2 double frustration. The four orange arrows point to the four transitions we use to estimate the fitted errors.

Error estimation based on plasmon transition ($\|0_{ES}\rangle \rightarrow \|3_{ES}\rangle$ transition at 20 mΦ_0)									
	E_J (K)	E_C (K)	E_L (K)	E_{CL} (K)	C_{sh} (fF)	α	C_{isl} (fF)	C_{int} (fF)	L_{factor}
Within 10% error	1.65 ∼ 1.85	3.00 ∼ 4.00	0.770 ∼ 1.35	3.50 ∼ 15.0	1100 ∼ 1400	0.0 ∼ 0.1	0.200 ∼ 6.00	0.800 ∼ 2.10	0.83 ∼ 1.1

Table 7.3: Fitted parameter error estimation based on plasmon transition.

of the parameters. In Table 7.5, we list the fitted errors for the $|0_{ES}\rangle \rightarrow |0_{EA}\rangle$ light fluxon transition at 0 mΦ_0. The light fluxon transition is very sensitive to E_J, E_C, E_L, E_{CL}, C_{isl} and C_{int}, so these fitted parameters extracted from fitting the light fluxon transition have very small errors. In Table. 7.6, we list the fitted errors for the anticrossing between the $|1_{ES}\rangle \rightarrow |4_{ES}\rangle$ transition and the $|1_{ES}\rangle \rightarrow |2_{OS}\rangle$ transition at 12 mΦ_0. The anticrossing is highly sensitive to E_J, E_C, E_L, so the errors for these fitted parameters by fitting the anticrossing are very small. Our fitting method fits all four types of transitions, so we are confident that the parameters of the actual chip are within the intersection of the estimated errors extracted from the four type of transitions, as shown in Table. 7.7.

Error estimation based on heavy fluxon transition ($\|0_{ES}\rangle \rightarrow \|2_{OS}\rangle$ transition at 6.5 mΦ_0)									
	E_J (K)	E_C (K)	E_L (K)	E_{CL} (K)	C_{sh} (fF)	α	C_{isl} (fF)	C_{int} (fF)	L_{factor}
Within 10% error	1.73 ~ 1.77	3.30 ~ 3.70	1.10 ~ 1.30	5.50 ~ 8.00	1050 ~ 1300	0.00 ~ 0.04	1.26 ~ 2.09	0.880 ~ 1.13	0.83 ~ 1.1

Table 7.4: Fitted parameter error estimation based on heavy fluxon transition.

Error estimation based on light fluxon transition ($\|0_{ES}\rangle \rightarrow \|0_{EA}\rangle$ transition at 0 mΦ_0)									
	E_J (K)	E_C (K)	E_L (K)	E_{CL} (K)	C_{sh} (fF)	α	C_{isl} (fF)	C_{int} (fF)	L_{factor}
Within 10% error	1.73 ~ 1.77	3.45 ~ 3.62	1.15 ~ 1.22	5.40 ~ 7.80	1000 ~ 1500	0.00 ~ 0.05	1.48 ~ 1.66	0.970 ~ 1.06	0.71 ~ 1.1

Table 7.5: Fitted parameter error estimation based on light fluxon transition.

Error estimation based on anticrossing between the $\|1_{ES}\rangle \rightarrow \|4_{ES}\rangle$ transition and the $\|1_{ES}\rangle \rightarrow \|2_{OS}\rangle$ transition at 12 mΦ_0									
	E_J (K)	E_C (K)	E_L (K)	E_{CL} (K)	C_{sh} (fF)	α	C_{isl} (fF)	C_{int} (fF)	L_{factor}
Within 10% error	1.71 ~ 1.76	3.50 ~ 3.85	1.14 ~ 1.38	5.80 ~ 12.5	1000 ~ 1500	0.02 ~ 0.06	0.980 ~ 1.67	0.880 ~ 1.01	0.91 ~ 1.2

Table 7.6: Fitted parameter error estimation based on plasmon-fluxon anticrossing.

Intersection of fitted errors estimated from four types of transitions								
E_J (K)	E_C (K)	E_L (K)	E_{CL} (K)	C_{sh} (fF)	α	C_{isl} (fF)	C_{int} (fF)	L_{factor}
1.73	3.50	1.15	5.80	1100	0.02	1.48	0.970	0.91
$\sim$	$\sim$	$\sim$	$\sim$	$\sim$	$\sim$	$\sim$	$\sim$	$\sim$
1.76	3.62	1.22	7.80	1300	0.04	1.66	1.01	1.1

Table 7.7: Intersection of fitted errors estimated from four types of transition.

Chapter 8

Summary and Future Directions

8.1 Summary

The plaquette devices are fabricated with arrays of Josephson junctions, with multiple on-chip flux- and charge-bias lines for local biasing of the various device elements. Microwave spectroscopy measurements allow for a characterization of the transitions between the different energy levels of the plaquette chain and their dispersion with flux and charge bias of the various device elements. Extensive numerical modeling of the energy-level structure and comparison with the measured transition spectra indicates that the device corresponds to a hardware implementation of stabilizer terms between plaquettes in the Hamiltonian and thus exhibits protection against local noise. This work paves the way for future qubits based on this design with optimized parameters and implementations that are capable of achieving dramatic reductions in error rates beyond the current state of the art.

In this thesis, I describe the experimental realization of quantum stabilizers in superconducting hardware with the plaquette-chain devices. The plaquette devices are fabricated with arrays of Josephson junctions and junction chains, with multiple on-chip flux- and charge-bias lines for local biasing of the various device elements. We characterize the transitions between different energy levels of the plaquette chain with respect to the flux and charge offset with microwave spectroscopy measurements. We indicate the protection against local noise by extensive numerical modeling of the energy-level structure and comparison with the measured transition spectra. In particular, we can relate the heavy fluxon transitions to the protection against bit-flip

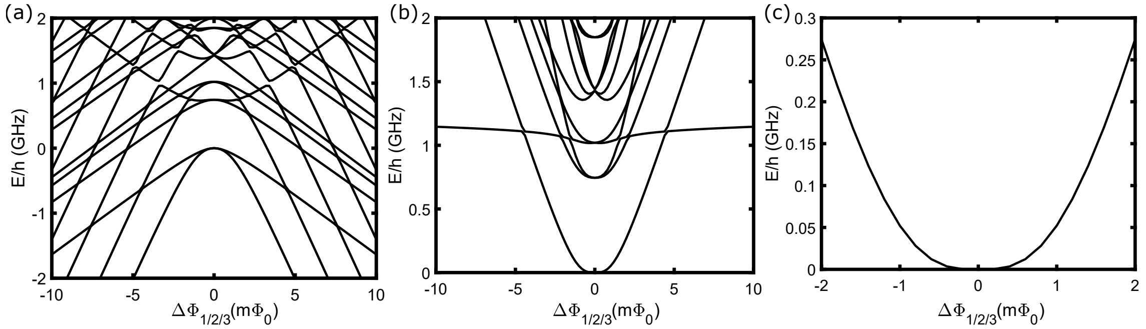

Figure 8.1: (a) Modeled energy levels near triple frustration with improved parameters, as described in text. (b) Modeled transitions near triple frustration. (c) Zoomed-in transition plot between 0 to 0.3 GHz.

errors and light fluxon transitions to the protection against phase-flip errors from flux noise. The presence of the light fluxon transition with a significant Δ_{SA} at double frustration is an indication of the implementation of an XX stabilizer between the two frustrated plaquettes.

In order to operate this circuit as a qubit, we need to improve our circuit parameters. We can replace the large planar shunt capacitor with a compact parallel-plate capacitor to reduce the effects of spurious antenna modes from the current large capacitor. To enhance the wavefunction hybridization, we can target larger E_C by reducing the electronic capacitance through an enhancement of the superconducting gap in the junction electrodes, either by using thin Al or granular Al grown in the presence of oxygen. We can operate the qubit without leaving the protected states by implementing protected gates with the SQUID switch.

8.2 Improved parameters

In Fig. 8.1, we show the triple plaquette modeling with improved parameters: E_J, E_C, E_L, C_{sh} and $\alpha = 3$ K, 5 K, 2 K, 1000 fF, 0.01. The E_J, E_L, E_J/E_L and C_{sh} are chosen so that we have large E_2 and large effective mass to suppress bit-flip errors. The ground-state doublet splitting Δ_{EO} near triple frustration is < 50 kHz. Assuming we fabricate a parallel-plate shunt capacitor using electron-beam evaporated SiO_2, which is compatible with our current ground-strap process, we must consider the loss tangent of the $\mathrm{SiO_2}$, which is ~1/300 [86]. The transition matrix element between the even-parity and odd-parity ground states at triple frustration for the above parameters is $\left|\langle O|\hat{N}|E\rangle\right| \sim 2\times10^{-5}$. We can then estimate T_1 between the ground-state doublet caused by dielectric loss in the parallel-plate by $T_1 \sim 1/\left|\langle O|\hat{N}|E\rangle\right|^2 \Delta_{EO}\tan\delta >> 1$ s.

The flux dispersion slope and curvature at triple frustration for a device with the parameters listed above is $\sim 1\times10^{-3}$ GHz/mΦ_0 and $\sim 3\times10^{-4}$ GHz/mΦ_0^2. The slope at exact triple frustration is not zero because $\alpha \neq 0$. Our flux bias precision limited by our equipment is $\sim 100\mu\Phi_0$. Assuming we can bias the plaquettes within $100\,\mu\Phi_0$ of triple frustration and assuming a $1/f$ flux-noise amplitude of $1\,\mu\Phi_0/\sqrt{\mathrm{Hz}}$ at 1 Hz, the T_2 predicted by our theory collaborators is ~1 ms.

8.3 Parallel plate capacitor

We use a planar shunt capacitor in the current design, so the area of the capacitor needs to be quite large to achieve C_{sh} ~1000 fF. The large-area shunt capacitor is very sensitive to background charge drift and acts as an antenna that absorbs energy from background radiation in the qubit environment that excites the qubit to higher levels and breaks Cooper pairs in the plaquette junctions. In order to mitigate these effects, it is important to make significantly more compact capacitors. In the future, we can achieve this by making parallel-plate capacitors, which will result in a much smaller footprint and thus higher spurious antenna mode frequencies and reduced charge sensing area.

8.4 Reducing electronic capacitance

As mentioned in Ch. 5, the electronic capacitance increases the total effective capacitance of the intermediate island, thus suppressing the effectiveness of the wavefunction hybridization at double and triple frustration. In order to have a large E_J in a junction with a simultaneous large E_C, this requires a large J_c. Thus, suppressing the electronic capacitance requires a larger Δ. This can be achieved in junctions with Al electrodes either by using thin Al or growing the Al in the presence of oxygen, both of which enhance Δ. The T_C of our conventional Al electrode is ~1.2 K, while thin Al or granular-Al films can have T_c as high as 2 K [87], thus suppressing the electronic

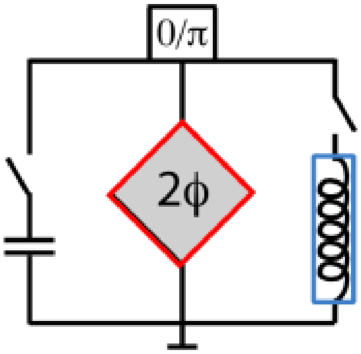

Figure 8.2: Schematic for implementing protected gates on charge-parity qubit. The $\cos 2\varphi$ element connects to the shunt capacitor or the superinductor through SQUID switches. The SQUID switch between the $\cos 2\varphi$ element and the shunt capacitor is normally closed, and opened briefly for X gates in the phase basis; the SQUID switch between the $\cos 2\varphi$ element and the superinductor is normally open, and closed briefly for Z gates in the phase basis.

capacitance by nearly a factor of 3.

8.5 Protected gates

We can operate a future charge-parity qubit with protected gates, so that during the gate operation, the qubit never leaves the protected state [88]. In Figure 8.2, we show the schematic for implementing protected gates on a charge-parity qubit. The $\cos 2\varphi$ element connects to the shunt capacitor or the superinductor through SQUID switches. The SQUID switch between the $\cos 2\varphi$ element and the shunt capacitor is normally closed, and opened briefly for X gates in the phase basis; the SQUID switch between the $\cos 2\varphi$ element and the superinductor is normally open, and closed briefly for Z gates in the phase basis.

Bibliography

[1] P. W. Shor. Algorithms for quantum computation: discrete logarithms and factoring. In *Proceedings 35th Annual Symposium on Foundations of Computer Science*, pages 124–134. IEEE, November 1994.

[2] Peter W. Shor. Polynomial-Time Algorithms for Prime Factorization and Discrete Logarithms on a Quantum Computer. *SIAM Rev.*, August 2006.

[3] Lov K. Grover. Quantum Mechanics Helps in Searching for a Needle in a Haystack. *Phys. Rev. Lett.*, 79(2):325–328, July 1997.

[4] John Preskill. Quantum Computing in the NISQ era and beyond. *Quantum*, 2:79, August 2018.

[5] Lawrence W. Cheuk, Matthew A. Nichols, Katherine R. Lawrence, Melih Okan, Hao Zhang, Ehsan Khatami, Nandini Trivedi, Thereza Paiva, Marcos Rigol, and Martin W. Zwierlein. Observation of spatial charge and spin correlations in the 2D Fermi-Hubbard model. *Science*, 353(6305):1260–1264, September 2016.

[6] Ala'n Aspuru-Guzik, Anthony D. Dutoi, Peter J. Love, and Martin Head-Gordon. Simulated Quantum Computation of Molecular Energies. *Science*, 309(5741):1704–1707, September 2005.

[7] Alberto Peruzzo, Jarrod McClean, Peter Shadbolt, Man-Hong Yung, Xiao-Qi Zhou, Peter J. Love, Alán Aspuru-Guzik, and Jeremy L. O'Brien. A variational eigenvalue solver on a photonic quantum processor. *Nat. Commun.*, 5(4213):1–7, July 2014.

[8] Cornelius Hempel, Christine Maier, Jonathan Romero, Jarrod McClean, Thomas Monz, Heng Shen, Petar Jurcevic, Ben P. Lanyon, Peter Love, Ryan Babbush,

Alán Aspuru-Guzik, Rainer Blatt, and Christian F. Roos. Quantum Chemistry Calculations on a Trapped-Ion Quantum Simulator. *Phys. Rev. X*, 8(3):031022, July 2018.

[9] Google A. I. Quantum Collaborators∗†, , Frank Arute, Kunal Arya, Ryan Babbush, Dave Bacon, Joseph C. Bardin, Rami Barends, Sergio Boixo, Michael Broughton, Bob B. Buckley, David A. Buell, Brian Burkett, Nicholas Bushnell, Yu Chen, Zijun Chen, Benjamin Chiaro, Roberto Collins, William Courtney, Sean Demura, Andrew Dunsworth, Edward Farhi, Austin Fowler, Brooks Foxen, Craig Gidney, Marissa Giustina, Rob Graff, Steve Habegger, Matthew P. Harrigan, Alan Ho, Sabrina Hong, Trent Huang, William J. Huggins, Lev Ioffe, Sergei V. Isakov, Evan Jeffrey, Zhang Jiang, Cody Jones, Dvir Kafri, Kostyantyn Kechedzhi, Julian Kelly, Seon Kim, Paul V. Klimov, Alexander Korotkov, Fedor Kostritsa, David Landhuis, Pavel Laptev, Mike Lindmark, Erik Lucero, Orion Martin, John M. Martinis, Jarrod R. McClean, Matt McEwen, Anthony Megrant, Xiao Mi, Masoud Mohseni, Wojciech Mruczkiewicz, Josh Mutus, Ofer Naaman, Matthew Neeley, Charles Neill, Hartmut Neven, Murphy Yuezhen Niu, Thomas E. O'Brien, Eric Ostby, Andre Petukhov, Harald Putterman, Chris Quintana, Pedram Roushan, Nicholas C. Rubin, Daniel Sank, Kevin J. Satzinger, Vadim Smelyanskiy, Doug Strain, Kevin J. Sung, Marco Szalay, Tyler Y. Takeshita, Amit Vainsencher, Theodore White, Nathan Wiebe, Z. Jamie Yao, Ping Yeh, and Adam Zalcman. Hartree-Fock on a superconducting qubit quantum computer. *Science*, 369(6507):1084–1089, August 2020.

[10] Edward Farhi and Hartmut Neven. Classification with quantum neural networks on near term processors. *arXiv preprint arXiv:1802.06002*, 2018.

[11] Iris Cong, Soonwon Choi, and Mikhail D. Lukin. Quantum convolutional neural networks. *Nat. Phys.*, 15:1273–1278, December 2019.

[12] Sergey Bravyi, David Gosset, and Robert König. Quantum advantage with shallow circuits. *Science*, 362(6412):308–311, October 2018.

[13] C. J. Ballance, T. P. Harty, N. M. Linke, M. A. Sepiol, and D. M. Lucas. High-Fidelity Quantum Logic Gates Using Trapped-Ion Hyperfine Qubits. *Phys. Rev. Lett.*, 117(6):060504, August 2016.

[14] W. Huang, C. H. Yang, K. W. Chan, T. Tanttu, B. Hensen, R. C. C. Leon, M. A. Fogarty, J. C. C. Hwang, F. E. Hudson, K. M. Itoh, A. Morello, A. Laucht, and A. S. Dzurak. Fidelity benchmarks for two-qubit gates in silicon. *Nature*, 569:532–536, May 2019.

[15] M. A. Rol, F. Battistel, F. K. Malinowski, C. C. Bultink, B. M. Tarasinski, R. Vollmer, N. Haider, N. Muthusubramanian, A. Bruno, B. M. Terhal, and L. DiCarlo. Fast, High-Fidelity Conditional-Phase Gate Exploiting Leakage Interference in Weakly Anharmonic Superconducting Qubits. *Phys. Rev. Lett.*, 123(12):120502, September 2019.

[16] Petar Jurcevic, Ali Javadi-Abhari, Lev S. Bishop, Isaac Lauer, Daniela F. Bogorin, Markus Brink, Lauren Capelluto, Oktay Günlük, Toshinari Itoko, Naoki Kanazawa, Abhinav Kandala, George A. Keefe, Kevin Krsulich, William Landers, Eric P. Lewandowski, Douglas T. McClure, Giacomo Nannicini, Adinath Narasgond, Hasan M. Nayfeh, Emily Pritchett, Mary Beth Rothwell, Srikanth Srinivasan, Neereja Sundaresan, Cindy Wang, Ken X. Wei, Christopher J. Wood, Jeng-Bang Yau, Eric J. Zhang, Oliver E. Dial, Jerry M. Chow, and Jay M. Gambetta. Demonstration of quantum volume 64 on a superconducting quantum computing system. *Quantum Sci. Technol.*, 6(2):025020, March 2021.

[17] Google A. I. Quantum, B. Foxen, C. Neill, A. Dunsworth, P. Roushan, B. Chiaro, A. Megrant, J. Kelly, Zijun Chen, K. Satzinger, R. Barends, F. Arute, K. Arya, R. Babbush, D. Bacon, J. C. Bardin, S. Boixo, D. Buell, B. Burkett, Yu Chen, R. Collins, E. Farhi, A. Fowler, C. Gidney, M. Giustina, R. Graff, M. Harrigan, T. Huang, S. V. Isakov, E. Jeffrey, Z. Jiang, D. Kafri, K. Kechedzhi, P. Klimov, A. Korotkov, F. Kostritsa, D. Landhuis, E. Lucero, J. McClean, M. McEwen, X. Mi, M. Mohseni, J. Y. Mutus, O. Naaman, M. Neeley, M. Niu, A. Petukhov, C. Quintana, N. Rubin, D. Sank, V. Smelyanskiy, A. Vainsencher, T. C. White, Z. Yao, P. Yeh, A. Zalcman, H. Neven, and J. M. Martinis. Demonstrating a Continuous Set of Two-Qubit Gates for Near-Term Quantum Algorithms. *Phys. Rev. Lett.*, 125(12):120504, September 2020.

[18] Google Quantum AI. Exponential suppression of bit or phase errors with cyclic error correction. *Nature*, 595:383–387, July 2021.

[19] Jay M. Gambetta, Jerry M. Chow, and Matthias Steffen. Building logical qubits in a superconducting quantum computing system. *npj Quantum Inf.*, 3(2):1–7, January 2017.

[20] John Clarke and Frank K. Wilhelm. Superconducting quantum bits. *Nature*, 453:1031–1042, June 2008.

[21] Rainer Blatt and David Wineland. Entangled states of trapped atomic ions. *Nature*, 453:1008–1015, June 2008.

[22] R. Hanson, L. P. Kouwenhoven, J. R. Petta, S. Tarucha, and L. M. K. Vandersypen. Spins in few-electron quantum dots. *Rev. Mod. Phys.*, 79(4):1217–1265, October 2007.

[23] Jeremy L. O'Brien, Akira Furusawa, and Jelena Vučković. Photonic quantum technologies. *Nat. Photonics*, 3:687–695, December 2009.

[24] Morten Kjaergaard, Mollie E Schwartz, Jochen Braumüller, Philip Krantz, Joel I-J Wang, Simon Gustavsson, and William D Oliver. Superconducting qubits: Current state of play. *Annual Review of Condensed Matter Physics*, 11:369–395, 2020.

[25] Jens Koch, M Yu Terri, Jay Gambetta, Andrew A Houck, DI Schuster, J Majer, Alexandre Blais, Michel H Devoret, Steven M Girvin, and Robert J Schoelkopf. Charge-insensitive qubit design derived from the cooper pair box. *Physical Review A*, 76(4):042319, 2007.

[26] M. D. Hutchings, J. B. Hertzberg, Y. Liu, N. T. Bronn, G. A. Keefe, Markus Brink, Jerry M. Chow, and B. L. T. Plourde. Tunable Superconducting Qubits with Flux-Independent Coherence. *Phys. Rev. Appl.*, 8(4):044003, October 2017.

[27] Vladimir E Manucharyan, Jens Koch, Leonid I Glazman, and Michel H Devoret. Fluxonium: Single cooper-pair circuit free of charge offsets. *Science*, 326(5949):113–116, 2009.

[28] Long B. Nguyen, Yen-Hsiang Lin, Aaron Somoroff, Raymond Mencia, Nicholas Grabon, and Vladimir E. Manucharyan. High-Coherence Fluxonium Qubit. *Phys. Rev. X*, 9(4):041041, November 2019.

[29] Irfan Siddiqi. Engineering high-coherence superconducting qubits. *Nat. Rev. Mater.*, 6:875–891, October 2021.

[30] Nathalie P. de Leon, Kohei M. Itoh, Dohun Kim, Karan K. Mehta, Tracy E. Northup, Hanhee Paik, B. S. Palmer, N. Samarth, Sorawis Sangtawesin, and D. W. Steuerman. Materials challenges and opportunities for quantum computing hardware. *Science*, 372(6539):eabb2823, April 2021.

[31] Michael A. Nielsen and Isaac L. Chuang. *Quantum Computation and Quantum Information: 10th Anniversary Edition*. Cambridge University Press, Cambridge, England, UK, January 2011.

[32] Austin G Fowler, Matteo Mariantoni, John M Martinis, and Andrew N Cleland. Surface codes: Towards practical large-scale quantum computation. *Physical Review A*, 86(3):032324, 2012.

[33] Steven M Girvin. Introduction to quantum error correction and fault tolerance. *arXiv preprint arXiv:2111.08894*, 2021.

[34] Rajeev Acharya, Igor Aleiner, Richard Allen, Trond I Andersen, Markus Ansmann, Frank Arute, Kunal Arya, Abraham Asfaw, Juan Atalaya, Ryan Babbush, et al. Suppressing quantum errors by scaling a surface code logical qubit. *arXiv preprint arXiv:2207.06431*, 2022.

[35] Nissim Ofek, Andrei Petrenko, Reinier Heeres, Philip Reinhold, Zaki Leghtas, Brian Vlastakis, Yehan Liu, Luigi Frunzio, S. M. Girvin, L. Jiang, Mazyar Mirrahimi, M. H. Devoret, and R. J. Schoelkopf. Extending the lifetime of a quantum bit with error correction in superconducting circuits. *Nature*, 536:441–445, August 2016.

[36] R. Barends, J. Kelly, A. Megrant, A. Veitia, D. Sank, E. Jeffrey, T. C. White, J. Mutus, A. G. Fowler, B. Campbell, Y. Chen, Z. Chen, B. Chiaro, A. Dunsworth, C. Neill, P. O'Malley, P. Roushan, A. Vainsencher, J. Wenner, A. N. Korotkov, A. N. Cleland, and John M. Martinis. Superconducting quantum circuits at the surface code threshold for fault tolerance. *Nature*, 508:500–503, April 2014.

[37] Matthew T Bell, Joshua Paramanandam, Lev B Ioffe, and Michael E Gershenson. Protected josephson rhombus chains. *Physical Review Letters*, 112(16):167001, 2014.

[38] W. C. Smith, A. Kou, X. Xiao, U. Vool, and M. H. Devoret. Superconducting circuit protected by two-Cooper-pair tunneling. *npj Quantum Inf.*, 6(8):1–9, January 2020.

[39] Konstantin Kalashnikov, Wen Ting Hsieh, Wenyuan Zhang, Wen-Sen Lu, Plamen Kamenov, Agustin Di Paolo, Alexandre Blais, Michael E Gershenson, and Matthew Bell. Bifluxon: Fluxon-parity-protected superconducting qubit. *PRX Quantum*, 1(1):010307, 2020.

[40] András Gyenis, Pranav S Mundada, Agustin Di Paolo, Thomas M Hazard, Xinyuan You, David I Schuster, Jens Koch, Alexandre Blais, and Andrew A Houck. Experimental realization of a protected superconducting circuit derived from the 0–π qubit. *PRX Quantum*, 2(1):010339, 2021.

[41] W. C. Smith, M. Villiers, A. Marquet, J. Palomo, M. R. Delbecq, T. Kontos, P. Campagne-Ibarcq, B. Douçot, and Z. Leghtas. Magnifying Quantum Phase Fluctuations with Cooper-Pair Pairing. *Phys. Rev. X*, 12(2):021002, April 2022.

[42] P. Krantz, M. Kjaergaard, F. Yan, T. P. Orlando, S. Gustavsson, and W. D. Oliver. A quantum engineer's guide to superconducting qubits. *Appl. Phys. Rev.*, 6(2):021318, June 2019.

[43] Grégoire Ithier. *Manipulation, readout and analysis of the decoherence ofa superconducting quantum bit.* PhD thesis, Université Pierre et Marie Curie - Paris VI, Paris, France, December 2005.

[44] Alexandre Blais, Arne L. Grimsmo, S. M. Girvin, and Andreas Wallraff. Circuit quantum electrodynamics. *Rev. Mod. Phys.*, 93(2):025005, May 2021.

[45] Michael Tinkham. *Introduction to Superconductivity: Second Edition (Dover Books on Physics).* Dover Publications, Mineola, NY, USA, June 2004.

[46] John M Martinis and Kevin Osborne. Superconducting qubits and the physics of josephson junctions. *arXiv preprint cond-mat/0402415*, 2004.

[47] Vinay Ambegaokar and Alexis Baratoff. Tunneling Between Superconductors. *Phys. Rev. Lett.*, 10(11):486–489, June 1963.

[48] Eric J. Zhang, Srikanth Srinivasan, Neereja Sundaresan, Daniela F. Bogorin, Yves Martin, Jared B. Hertzberg, John Timmerwilke, Emily J. Pritchett, Jeng-Bang Yau, Cindy Wang, William Landers, Eric P. Lewandowski, Adinath Narasgond, Sami Rosenblatt, George A. Keefe, Isaac Lauer, Mary Beth Rothwell, Douglas T. McClure, Oliver E. Dial, Jason S. Orcutt, Markus Brink, and Jerry M. Chow. High-performance superconducting quantum processors via laser annealing of transmon qubits. *Sci. Adv.*, 8(19):eabi6690, May 2022.

[49] András Gyenis, Agustin Di Paolo, Jens Koch, Alexandre Blais, Andrew A Houck, and David I Schuster. Moving beyond the transmon: Noise-protected superconducting quantum circuits. *PRX Quantum*, 2(3):030101, 2021.

[50] Alexei Kitaev. Protected qubit based on a superconducting current mirror. *arXiv preprint cond-mat/0609441*, 2006.

[51] John M. Martinis, K. B. Cooper, R. McDermott, Matthias Steffen, Markus Ansmann, K. D. Osborn, K. Cicak, Seongshik Oh, D. P. Pappas, R. W. Simmonds, and Clare C. Yu. Decoherence in Josephson Qubits from Dielectric Loss. *Phys. Rev. Lett.*, 95(21):210503, November 2005.

[52] David M. Pozar. *Microwave Engineering*. Wiley, Hoboken, NJ, USA, November 2011.

[53] C. Wang, C. Axline, Y. Y. Gao, T. Brecht, Y. Chu, L. Frunzio, M. H. Devoret, and R. J. Schoelkopf. Surface participation and dielectric loss in superconducting qubits. *Appl. Phys. Lett.*, 107(16):162601, October 2015.

[54] C. D. Wilen, S. Abdullah, N. A. Kurinsky, C. Stanford, L. Cardani, G. D'Imperio, C. Tomei, L. Faoro, L. B. Ioffe, C. H. Liu, A. Opremcak, B. G. Christensen, J. L. DuBois, and R. McDermott. Correlated charge noise and relaxation errors in superconducting qubits. *Nature*, 594:369–373, June 2021.

[55] Y. Nakamura, Yu. A. Pashkin, T. Yamamoto, and J. S. Tsai. Charge Echo in a Cooper-Pair Box. *Phys. Rev. Lett.*, 88(4):047901, January 2002.

[56] Y. Nakamura, Yu. A. Pashkin, and J. S. Tsai. Coherent control of macroscopic quantum states in a single-Cooper-pair box. *Nature*, 398:786–788, April 1999.

[57] BG Christensen, CD Wilen, A Opremcak, J Nelson, F Schlenker, CH Zimonick, L Faoro, LB Ioffe, YJ Rosen, JL DuBois, et al. Anomalous charge noise in superconducting qubits. *Physical Review B*, 100(14):140503, 2019.

[58] Frederick C. Wellstood, Cristian Urbina, and John Clarke. Low-frequency noise in dc superconducting quantum interference devices below 1 K. *Appl. Phys. Lett.*, 50(12):772–774, March 1987.

[59] Robert McDermott. Materials Origins of Decoherence in Superconducting Qubits. *IEEE Trans. Appl. Supercond.*, 19(1):2–13, January 2009.

[60] S. M. Anton, J. S. Birenbaum, S. R. O'Kelley, V. Bolkhovsky, D. A. Braje, G. Fitch, M. Neeley, G. C. Hilton, H.-M. Cho, K. D. Irwin, F. C. Wellstood, W. D. Oliver, A. Shnirman, and John Clarke. Magnetic Flux Noise in dc SQUIDs: Temperature and Geometry Dependence. *Phys. Rev. Lett.*, 110(14):147002, April 2013.

[61] P. Kumar, S. Sendelbach, M. A. Beck, J. W. Freeland, Zhe Wang, Hui Wang, Clare C. Yu, R. Q. Wu, D. P. Pappas, and R. McDermott. Origin and Reduction of $1/f$ Magnetic Flux Noise in Superconducting Devices. *Phys. Rev. Appl.*, 6(4):041001, October 2016.

[62] S. E. de Graaf, A. A. Adamyan, T. Lindström, D. Erts, S. E. Kubatkin, A. Ya. Tzalenchuk, and A. V. Danilov. Direct Identification of Dilute Surface Spins on Al_2O_3: Origin of Flux Noise in Quantum Circuits. *Phys. Rev. Lett.*, 118(5):057703, January 2017.

[63] John M Martinis, M Ansmann, and J Aumentado. Energy decay in superconducting josephson-junction qubits from nonequilibrium quasiparticle excitations. *Physical review letters*, 103(9):097002, 2009.

[64] Matt McEwen, Lara Faoro, Kunal Arya, Andrew Dunsworth, Trent Huang, Seon Kim, Brian Burkett, Austin Fowler, Frank Arute, Joseph C. Bardin, Andreas Bengtsson, Alexander Bilmes, Bob B. Buckley, Nicholas Bushnell, Zijun

Chen, Roberto Collins, Sean Demura, Alan R. Derk, Catherine Erickson, Marissa Giustina, Sean D. Harrington, Sabrina Hong, Evan Jeffrey, Julian Kelly, Paul V. Klimov, Fedor Kostritsa, Pavel Laptev, Aditya Locharla, Xiao Mi, Kevin C. Miao, Shirin Montazeri, Josh Mutus, Ofer Naaman, Matthew Neeley, Charles Neill, Alex Opremcak, Chris Quintana, Nicholas Redd, Pedram Roushan, Daniel Sank, Kevin J. Satzinger, Vladimir Shvarts, Theodore White, Z. Jamie Yao, Ping Yeh, Juhwan Yoo, Yu Chen, Vadim Smelyanskiy, John M. Martinis, Hartmut Neven, Anthony Megrant, Lev Ioffe, and Rami Barends. Resolving catastrophic error bursts from cosmic rays in large arrays of superconducting qubits. *Nat. Phys.*, 18:107–111, January 2022.

[65] V Iaia, J Ku, A Ballard, CP Larson, E Yelton, CH Liu, S Patel, R McDermott, and BLT Plourde. Phonon downconversion to suppress correlated errors in superconducting qubits. *arXiv preprint arXiv:2203.06586*, 2022.

[66] John M Martinis. Saving superconducting quantum processors from decay and correlated errors generated by gamma and cosmic rays. *npj Quantum Information*, 7(1):1–9, 2021.

[67] M. Houzet, K. Serniak, G. Catelani, M. H. Devoret, and L. I. Glazman. Photon-Assisted Charge-Parity Jumps in a Superconducting Qubit. *Phys. Rev. Lett.*, 123(10):107704, September 2019.

[68] O Rafferty, S Patel, CH Liu, S Abdullah, CD Wilen, DC Harrison, and R McDermott. Spurious antenna modes of the transmon qubit. *arXiv preprint arXiv:2103.06803*, 2021.

[69] Chuan-Hong Liu, David C Harrison, Shravan Patel, Christopher D Wilen, Owen Rafferty, Abigail Shearrow, Andrew Ballard, Vito Iaia, Jaseung Ku, Britton LT Plourde, et al. Quasiparticle poisoning of superconducting qubits from resonant absorption of pair-breaking photons. *arXiv preprint arXiv:2203.06577*, 2022.

[70] D. I. Schuster, A. Wallraff, A. Blais, L. Frunzio, R.-S. Huang, J. Majer, S. M. Girvin, and R. J. Schoelkopf. ac Stark Shift and Dephasing of a Superconducting Qubit Strongly Coupled to a Cavity Field. *Phys. Rev. Lett.*, 94(12):123602, March 2005.

[71] Fei Yan, Simon Gustavsson, Archana Kamal, Jeffrey Birenbaum, Adam P. Sears, David Hover, Ted J. Gudmundsen, Danna Rosenberg, Gabriel Samach, S. Weber, Jonilyn L. Yoder, Terry P. Orlando, John Clarke, Andrew J. Kerman, and William D. Oliver. The flux qubit revisited to enhance coherence and reproducibility. *Nat. Commun.*, 7(12964):1–9, November 2016.

[72] A. P. Sears, A. Petrenko, G. Catelani, L. Sun, Hanhee Paik, G. Kirchmair, L. Frunzio, L. I. Glazman, S. M. Girvin, and R. J. Schoelkopf. Photon shot noise dephasing in the strong-dispersive limit of circuit QED. *Phys. Rev. B*, 86(18):180504, November 2012.

[73] Valérie Lefevre-Seguin, Emmanuel Turlot, Cristian Urbina, Daniel Esteve, and Michel H Devoret. Thermal activation of a hysteretic dc superconducting quantum interference device from its different zero-voltage states. *Physical Review B*, 46(9):5507, 1992.

[74] JE Mooij, TP Orlando, L Levitov, Lin Tian, Caspar H Van der Wal, and Seth Lloyd. Josephson persistent-current qubit. *Science*, 285(5430):1036–1039, 1999.

[75] I. M. Pop, B. Douçot, L. Ioffe, I. Protopopov, F. Lecocq, I. Matei, O. Buisson, and W. Guichard. Experimental demonstration of Aharonov-Casher interference in a Josephson junction circuit. *Phys. Rev. B*, 85(9):094503, March 2012.

[76] M. T. Bell, W. Zhang, L. B. Ioffe, and M. E. Gershenson. Spectroscopic Evidence of the Aharonov-Casher Effect in a Cooper Pair Box. *Phys. Rev. Lett.*, 116(10):107002, March 2016.

[77] Andrey R Klots and Lev B Ioffe. Topology of quantum superconducting circuits. *In preparation.*

[78] Andrey R Klots. SuperQuantPackageV2, July 2022. [Online; accessed 6. Jul. 2022].

[79] John M Martinis. Saving superconducting quantum processors from decay and correlated errors generated by gamma and cosmic rays. *npj Quantum Information*, 7(1):1–9, 2021.

[80] Ulrich Eckern, Gerd Schön, and Vinay Ambegaokar. Quantum dynamics of a superconducting tunnel junction. *Physical Review B*, 30(11):6419, 1984.

[81] SUN Magnetics | Integrated Circuit Inductance Extraction | Stellenbosch, September 2022. [Online; accessed 15. Oct. 2022].

[82] Coenrad Johann Fourie and Kyle Jackman. Software Tools for Flux Trapping and Magnetic Field Analysis in Superconducting Circuits. *IEEE Trans. Appl. Supercond.*, 29(5):1–4, February 2019.

[83] Coenrad J. Fourie. Electronic Design Automation tools for superconducting circuits. *J. Phys. Conf. Ser.*, 1590(1):012040, July 2020.

[84] Antti P. Vepsäläinen, Amir H. Karamlou, John L. Orrell, Akshunna S. Dogra, Ben Loer, Francisca Vasconcelos, David K. Kim, Alexander J. Melville, Bethany M. Niedzielski, Jonilyn L. Yoder, Simon Gustavsson, Joseph A. Formaggio, Brent A. VanDevender, and William D. Oliver. Impact of ionizing radiation on superconducting qubit coherence. *Nature*, 584:551–556, August 2020.

[85] A. V. Shytov, D. A. Ivanov, and M. V. Feigel'man. Landau-Zener interferometry for qubits. *Eur. Phys. J. B*, 36(2):263–269, November 2003.

[86] Aaron D. O'Connell, M. Ansmann, R. C. Bialczak, M. Hofheinz, N. Katz, Erik Lucero, C. McKenney, M. Neeley, H. Wang, E. M. Weig, A. N. Cleland, and J. M. Martinis. Microwave dielectric loss at single photon energies and millikelvin temperatures. *Appl. Phys. Lett.*, 92(11):112903, March 2008.

[87] F. Levy-Bertrand, T. Klein, T. Grenet, O. Dupré, A. Benoît, A. Bideaud, O. Bourrion, M. Calvo, A. Catalano, A. Gomez, J. Goupy, L. Grünhaupt, U. v. Luepke, N. Maleeva, F. Valenti, I. M. Pop, and A. Monfardini. Electrodynamics of granular aluminum from superconductor to insulator: Observation of collective superconducting modes. *Phys. Rev. B*, 99(9):094506, March 2019.

[88] Andrey R. Klots and Lev B. Ioffe. Set of holonomic and protected gates on topological qubits for a realistic quantum computer. *Phys. Rev. B*, 104(14):144502, October 2021.

Yebin Liu

Email: ryan.lyeb@gmail.com | Place of Birth: China

EDUCATION

- **Syracuse University** Syracuse, NY
  Ph.D. expected 12/2022 08/2014 - present
- **China University of Mining and Technology (CUMT)** Xuzhou, China
  Bachelor of Science, Applied Physics 09/2010 - 07/2014

PUBLICATIONS

“Tunable superconducting qubits with flux-independent coherence” M.D. Hutchings, J.B. Hertzberg, Y. Liu, N.T. Bronn, G.A. Keefe, M. Brink, J.M. Chow, B.L.T. Plourde, Physical Review Applied 8, 044003 (2017).

"Implementing quantum stabilizers with superconducting hardware" K. Dodge*, Y. Liu*, et al., in preparation. * = equal author contributions.

INVITED PRESENTATIONS

- **Applied Superconductivity Conference** 11/2020
  Characterization of topologically protected charge-parity qubits
- **Cryogenic Engineering Conference and International Cryogenic Materials Conference** 07/2019
  Implementation of π-periodic Josephson elements for topologically protected charge-parity qubits

CONTRIBUTED CONFERENCE PRESENTATIONS

- **American Physical Society, March Meeting** 03/2022
  Charge-parity qubits based on concatenation of π-periodic Josephson elements: Part 1
- **American Physical Society, March Meeting** 03/2019
  Implementation of π-periodic Josephson elements for topologically protected charge-parity qubits
- **American Physical Society, March Meeting** 03/2018
  Exploration of alternate fabrication and processing techniques for superconducting qubit junctions

AWARDS

- **Third prize in Jiangsu Physics and Experimental Technique Innovation Competition**,
  Physical Society of Jiangsu Province, China 2013
- **First Prize Scholarship of CUMT,** CUMT 2012,2011